Faculty of Natural Science and Technology
Department of Physics

NTNU
Norwegian University of
Science and Technology

MASTER'S THESIS FOR

NORA KLEINKNECHT

Thesis started: 17. August 2009
Thesis submitted: 7. May 2010

DISCIPLINE: Physics

Title: *"Planetary Wave Oscillations Observed in Ozone from Troll Station Antartica"*

This work has been carried out at Department of Physics, under the supervision of Prof. Dr. Patrick J. Espy

---

Acknowledgments

Great thanks to my spervisor Prof. Patrick J. Espy who always had time to discuss my results, answer my questions and tell interesting and funny stories. I am also greatful for the help given by Ole Martin Christiensen to get a good start. My thanks also to Prof. Gerd Sonnemann from the Leizig Insitut of Atmospheric Physics in Kühlingsborn who provided me with the ozone data from the COMMA-IPA model. In addition I want to thank Snorre Hansen for answering all my administrative questions and Terje Røsten for solving all problems with the computer. I am thankful for all encouragement and support from my family and greatful for Kristian lightening my days.

Abstract

This thesis investigates the possibility of tracing planetary waves with ozone. The mixing ratio of ozone is sensitive to variations of its environment introduced by waves due to its short chemical lifetime. Ground-based millimetre-wave remote sensing of the 249.6 ozone line deep within the Antarctic vortex at Troll station (72°S, 2°E) have been used to retrieval vertical ozone mixing ratio profiles below 100 km by the use of the optimal estimation method. Calculations cover data from December 2008 until November 2009 with a spectra resolution of 1 hour and an altitude resolution of 8 km. Fluctuations of the ozone mixing ratio where separated from seasonal variations. Spectral analysis were done by Lomb-Scargle analysis and a Morlet wavelet transform for altitudes between 35 and 75 km. Wave activity consistent with models and other measurements of planetary waves was found. Periodic bands of 1.7-4, 4-8 and 8-16 days were extracted and could basically be related to the quasi two-day wave and the first three normal planetary modes. In addition consistence to wave activity extracted from meteor radar wind measurements at Senae could be shown.

Contents

Chapter 1

Introduction

Planetary waves are large-scale motions of the atmosphere. They have horizontal scales of thousands of kilometres and a vertical size of several kilometres. They are important for the understanding of many large-scale atmospheric phenomena. For example, planetary wave activity is assumed to be responsible for the early break down of the Antarctic vortex in 2002 that led to an unusually small "ozone hole" in the Antarctic spring that year [*Baldwin and et al.*, 2003]. Their interaction with the atmosphere and other wave activities is complex and not fully understood. A pure mathematical representation of planetary waves is useful to understand planetary wave characteristics but numerical calculations are needed to consider propagation in a real atmosphere. Measurements are important to test these models and characterize planetary wave activity and their impact on atmospheric dynamics.

Planetary wave activity has mainly been studied in upper mesospheric-lower thermosphere (MLT) and tropospheric-lower stratospheric (TLS) regions. Such measurements are done by radars and balloons, respectively. Observations in the region within the stratosphere and mesosphere are less common because the above mentioned methods can not observe this region. In addition other methods covering this altitude range, such as LIDAR or falling spheres, are unsuitable for measuring planetary waves or very expensive. LIDAR measurements require very clear skies and their operation at daytime is challiging, leading to sporadic data coverage in time. Furthermore, LIDARs measure density relative to a particular height, usally about 40 km, above which the signal is dominated by molecular Rayleigh scatter. This removes temparture and pressure variations due to planetary normal modes from the measurement. Falling spheres are balloons droped from a rockets. It is possible to monitor planetary waves with such measurements but to achive the necessary time resolution requirs a long compagn with many rockets, which becomes prohibitively expensive. In contrast ground based remote sensing of ozone operates automatically, offering the posibility of continuous monitoring of atmospheric conditions at upper stratospheric and mesospheric altitudes at a fixed horizontal location. This thesis seeks to extract planetary wave activity from the variations in the ozone mixing ratio above Troll station, Antarctica.

After going into the structure of the atmosphere and planetary wave theory, the chemistry and distribution of ozone is described and its ability to trace waves is discussed. Then the measurement principle and the design and foibles of the microwave radiometer at Troll are presented. Finally, the inverted profiles and the retrieval of planetary wave activity are considered and compared with the COMMA-IAP model and meteor wind measurements at Sanae, respectively.

Chapter 2

Theory

Nomencluture for all used variables can be found in Appendix A.

2.1 Atmosphere

2.1.1 Atmospheric structure of the earth

The properties (temperature, moisture, cloudiness, chemical constituents and density) of the atmosphere change makedly with altitude. Conventionally the atmosphere is divided in vertical layers, according to the sign change of the temperature gradient with height. In the lowest layer, the troposphere, the temperature decreases with altitude because the effect of surface heating reduces. It is bounded by the tropopause at around 15 km and followed by the stratosphere, which is bounded by the stratopause at around 50 km. In the stratosphere the temperature rises with altitude due to absorption of solar ultra violet radiation by ozone (O_3), known as ozone heating. The temperature then drops again in the mesosphere, due to diminished ozone heating and increasing radiative cooling to space by Carbon dioxide (CO_2). These two layers together are also called the middle atmosphere. At around 85 km the mesopause separates the middle atmosphere from the upper atmosphere, where ionisation of molecules by energetic solar radiation produces a plasma of free electrons. The temperature in this region increases steadily with altitude due to molecular dissociation by very energetic solar radiation. [*Salby*, 1995]

2.1.2 Atmospheric composition of the earth

The atmosphere is a mixture of different gases. Table 2.1 shows typical values of air near the ground. In dry air the volume mixing ratio of the components is constant. [*Malberg*, 2007] In the lower and middle atmosphere the composition of air varies little because the major constituents O_2 (20%) and N_2 (80%) are not significantly involved in chemical reactions.

species	dry air [Vol%]	wet air [Vol%]
N_2	78.1	77.0
O_2	21.0	20.7
Ar	0.9	0.9
CO_2	0.04	0.03
Ne, He, Kr,H_2, O_3, SO_2	<0.01	<0.01
H2O	-	1.3

Table 2.1: Composition of the air near the ground. From *Malberg* [2007]

Due to this feature the atmosphere in these layers can be described as a homogenous and continuous fluid. In the upper atmosphere this assumption is not longer valid, because the mean molecular weight decreases with altitude due to diffusive separation between heavier and lighter compounds in addition with a decrease of the amount of O_2 and N_2 due to rapid photo dissociation. [*Brasseur and Solomon*, 2005]

2.1.3 Atmospheric dynamics

The atmosphere is driven by radiative, chemical and dynamical processes. In general the atmosphere can be compared to a heat engine; heated due to absorption of sunlight and cooled by long wavelength radiation. Latitudinal variations of solar radiation result in net heating in the tropics and net cooling at the poles, which leads to a net heat transport towards the poles [*Malberg*, 2007]. In other words the sun drives the atmosphere towards a radiative equilibrium resulting in a baroclinic state, and dynamics like thermal winds, created by this pressure differences, then drive the atmosphere back to the energetic lower barotopic state. This interaction of radiation and dynamics, plus the curvature and rotation of the earth and chemical processes, create a complex structure of the atmosphere and a wide range of wave phenomena, such as tides, gravity waves and planetary waves. The timescales of such periodic motion ranges from a few minutes to several month. Wave interactions drive the atmosphere far away from radiative equilibrium especially in polar regions. The dynamics of the atmosphere can generally be modelled by the laws of fluid mechanics.

2.2 Wave Theory

2.2.1 Basic equations

Focusing on the middle atmosphere the assumption of the atmosphere as a continuous, isotropic, classical, Newtonian fluid that is forced by gravity, friction and pressure gradients and the rotation of the earth is usually valid. Under this assumption Newton's second law leads to the Navier-Stokes equation (B.1), which can be rewritten in spherical coordinates (B.1.1) and linearized. Further simplification can be achieved by applying the shallow

water, the traditional approximation and the hydrostatic approximation leading to the horizontal momentum equations and the hydrostatic equation (B.2). A more detailed derivation can be found in appendix B.

The equations of motion plus the continuity equation and the first law of thermodynamics are known as the linearized primitive equations. They approximately describe large-scale motion in the stratospheric and mesospheric regions. As stated in *Forbes* [1995] the linearized primitive equations for small atmospheric perturbations in a motionless atmosphere can be written in terms of the northward, v, eastward, u, and vertical, w, velocities:

$$\frac{\partial u}{\partial t} - fv + \frac{1}{a \cdot cos\phi}\frac{\partial \Phi}{\partial \lambda} = 0, \tag{2.1}$$

$$\frac{\partial v}{\partial t} - fu + \frac{1}{a}\frac{\Phi}{\partial \phi} = 0, \tag{2.2}$$

$$\frac{\partial}{\partial t}\frac{\partial \Phi}{\partial z} + N^2 w = \frac{\kappa J}{H}, \tag{2.3}$$

$$\frac{1}{a \cdot cos\phi}\left[\frac{\partial u}{\partial \lambda} + \frac{\partial}{\partial \phi}(v \cdot cos\phi)\right] + \frac{1}{\rho_0}\frac{\partial}{\partial z}(\rho_0 w) = 0, \tag{2.4}$$

where

a = earth's radius
f = coriolis parameter
J = heating rate per unit mass
λ = longitude
ϕ = latitude

The geopotential Φ, the buoyancy frequency N, the scale height H and the basic density ρ_0 are also introduced. These quantities are, in turn, given as:

$$\Phi = -\int \frac{RT}{p} dp,$$

$$N = \sqrt{\frac{\kappa g}{H}},$$

$$H = \frac{RT_m}{g},$$

$$\rho_0 = \rho(z=0) exp\left(\frac{-z}{H}\right)$$

2.2.2 Linear Wave Theory

Following *Forbes* [1995], perturbations are assumed to consist of longitudinally propagating waves of zonal wave number k and frequency σ, and the vertical and latitudinal dependen-

cies are separated as follows,

$$\left\{\begin{array}{c} u \\ \\ v \\ \\ \Phi \\ \\ J \end{array}\right\} = \sum_n \left\{\begin{array}{c} \frac{\sigma}{4\Omega^2 a} U_n(\phi) G_n(z) \\ \\ \frac{-i\sigma}{4\Omega^2 a} V_n(\phi) G_n(z) \\ \\ \Theta_n(\phi) G_n(z) \\ \\ \Theta_n(\phi) J_n(z) \end{array}\right\} exp[i(k\lambda - \sigma t)]. \tag{2.5}$$

The velocity expansion functions U_n and V_n are derivations of the Θ_n and given in Appendix B.3. This separate solution exists where the functions Θ_n are a complete orthogonal set. They represent the horizontal structure of the wave. The separation condition (B.4) for z and ϕ leads to the vertical structure equation,

$$\frac{d^2 G_n'}{dx^2} + \alpha^2 \; G_n' = -\frac{\sqrt{\rho_0}}{i\sigma N} \frac{d}{dx}(\rho_0 \kappa J_n) = F(x), \tag{2.6}$$

by defining

$$\begin{aligned} x &= \frac{z}{H}, \\ \alpha^2 &= \frac{\kappa H}{h_n} - \frac{1}{4}, \\ G_n' &= G_n \frac{\sqrt{\rho}}{N}, \end{aligned}$$

and assuming a isothermal atmosphere (T=256K) for which $N^2 = \frac{\kappa g}{H(256K)} = \frac{\kappa g}{7{,}5km}$. The separation constant h_n is know as the equivalent depth. It connects the vertical structure equation and the Laplace's tidal equation (B.5). Laplace's tidal equation embodies the ϕ-dependent part of the solution and can be written as an eigenvalue problem, as follows:

$$f_{k,\nu}\left(\Theta_n^{k,\nu}\right) = \epsilon_n^{k,\nu} \Theta_n^{k,\nu}. \tag{2.7}$$

Here $\epsilon_n = \frac{(2\Omega a)^2}{g h_n}$ is the eigenvalue and $\nu = \frac{\sigma}{\Omega}$ the normalized frequency. Positive (negative) values of ν correspond to eastward (westward) propagation. The reciprocal of the normalized frequency is the dimensionless period $\tau = \frac{1}{|\nu|}$ of the wave in numerical units of one sidereal day ($\Omega = 7.29 \cdot 10^{-5} s^{-1}$).

For each set of k and ν there exist a set of eigenvalues ϵ_n and eigenfunctions Θ_n that satisfies the Laplace Tidal equation. Therefore each wave mode can be uniquely identified by the zonal wave number k, the meridional wave number n and the normalised wave frequency ν. It is common to refer to a particular mode as the (k, n) mode, and add information about the wave period. The eigenfunctions Θ_n, called Hough functions, represent the horizontal structure of the wave.

Two families of curves can be distinguished by plotting corresponding normal frequencies ν and eigenfunctions ϵ_n for a given zonal wave number k. Figure 2.1 shows such a plot

for zonal wave number k=1. One family (Class I), known as gravity waves, always has positive eigenvalue ϵ_n. This family is labeled with positive meridional wave numbers, n. The other family (Class II), known as planetary waves or Rossby waves, has positive eigenvalues for westward propagation and negative eigenvalues in all other cases and vanish for periods shorter that 12 hours ($|\nu|$=2.0). Class II modes are labeled with their negative meridional wave number, -n. The mode behaving like a planetary wave for large frequencies and like a gravity wave for small frequencies, here (1,-1), is known as a mixed gravity-planetary mode or Yanai wave.

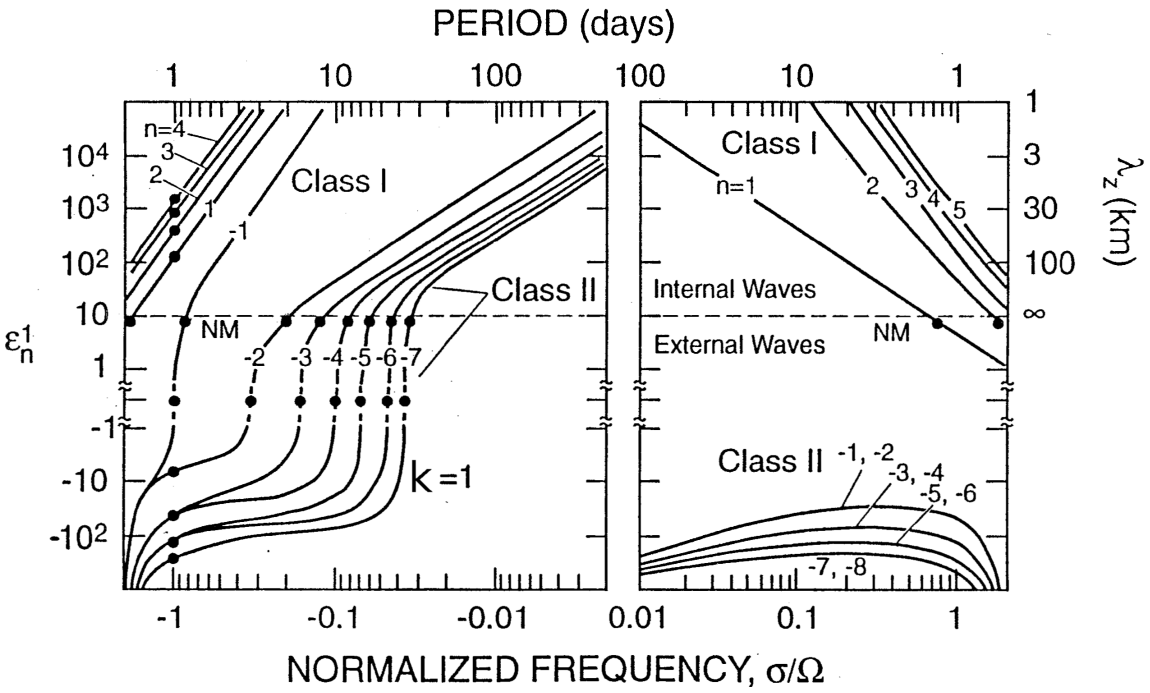

Figure 2.1: Eigenvalues ϵ_n^k of wave modes of zonal wave number k=1 vs. normalized frequency. Waves with positive (negative) frequency propagate eastward (westward). The horizontal dashed line indicates the transition from internal to external modes. The dots corresponding to "NM" refer to Normal modes ($\epsilon_n^1 \approx 8.4$; Class I = gravity waves; Class II = planetary waves. From *Forbes* [1995])

Free and forced solutions

- Forced solutions

  The two solutions to the vertical structure equation that exist for F(x)$\neq$ 0 are called

forced modes.

$$G_n \propto \exp(-|\alpha|x),$$

$$\alpha = \sqrt{\left(\frac{\kappa H g}{2\Omega a}\right)\epsilon_n - \frac{1}{4}}$$

is the solution for negative or small values of ϵ_n ($\alpha^2 < 0$). They are called trapped or evanescent and correspond to wave oscillations, which are confined to the region of their excitation.

The solution corresponding to sufficient large positive values of ϵ_n ($\alpha^2 > 0$) and a positive vertical group velocity at high altitudes, is

$$G_n \propto \exp(\pm i|\alpha|x),$$

$$\alpha = \sqrt{\left(\frac{\kappa H g}{2\Omega a}\right)\epsilon_n - \frac{1}{4}}$$

This solution refers to westward (+)/eastward (-) wave propagation away from the source. The assumption of positive vertical group velocity at high altitudes demands that at the energy flux is up going in this region. For forced modes the frequency is generally given by the forcing and therefore known. All modes corresponding to a particular forcing frequency can be found by drawing a vertical line at ν in Figure 2.1. The ϵ_n values defined by points of intersection correspond to the modes responding to the forcing frequency. In Figure 2.1 this is shown for the diurnal tide ($\nu = -1.0$). The responding modes are a mixture of trapped (α^2 ¡ 0) and propagating (α^2 ¿ 0) modes. Matching of the forcing with horizontal and vertical structures determines if the trapped or the propagating modes responce most.

- Free solutions

  Free or unforced modes are solutions to the vertical structure equation for zero total forcing (F(x)=0), meaning that they occurre due to random forcing such as unsteady basic flow over topographic and thermal contrast. A solution to the unforced vertical structure equation is

$$G_n \propto exp\left(\kappa - \frac{1}{2}x\right)$$

$$\text{with } h_n = \frac{H}{1-\kappa},$$

  This is the only non-trivial solution satisfying boundedness and zero vertical velocity at the ground. Unforced wave modes correspond to a resonant response of the atmosphere. The solution implies exponential increase of the horizontal velocity and other wave fields with altitude and energy decay away from the surface. For small

or negative values of ϵ_n there is no vertical flux of energy out of the atmosphere and no phase change with height.

The free modes are also known as the normal modes of the system. Their values of ϵ_n are defined by the solution of the vertical structure equation and therefore can this modes and their frequencies be found by drawing a horizontal line at the calculated value of ϵ_n in Figure 2.1. This is here done for $\epsilon_n = 8.4$ which corresponds to an isothermal atmosphere of T=256K. The points of intersection (labelled with NM) give the frequencies of the normal modes. Normal modes are resonant modes of the atmosphere.

Phase progression

The phase progression in height (x) and longitude (λ) for propagating modes has the form

$$k\lambda \pm \alpha x - \sigma t = \text{const.} \tag{2.8}$$

It describes a line of constant phase equals zero. For a fixed longitude (λ) this leads to downward phase progression as time increases, $x = -\frac{|\sigma|}{\alpha}t + \text{const.'}$, for both eastward ($-\alpha, \sigma > 0$) and westward ($+\alpha, \sigma < 0$) propagating waves. For a fixed time (t) the equation results in, $x = \pm\frac{k}{\alpha}\lambda + \text{const"}$, corresponding to westward (+)/eastward (-) phase tilt for westward/eastward propagating waves. The amplitude of propagating waves increases with altitude due to energy conversation and exponential decrease of air density.

Normal modes are resonant modes of an ideal (isothermal, uniform rotating) atmosphere, as mentioned above. They show therefore no downward phase progession and no amplitude change with height.

2.2.3 Planetary waves

Planetary waves are important for the understanding of many large-scale atmospheric phenomena like the early break down of the Antarctic vortex in 2002. The early break down let to a small "ozone hole" in the Antarctic spring [*Baldwin and et al.*, 2003]. Their horizontal scale is in the order of thousands of kilometres and their vertical size extends over several kilometres. As derived in Section 2.2.2 planetary waves are formed due to the combination of meridional temperature gradients and the rotation and curvature of the earth. They are forced by irregular thermal or mechanical forcing, or by stationary topographies such as large mountain areas. They can also be forced by stationary heat sources and land-ocean heating contrast, or by instabilities arising from gradients in the temperature and wind distribution. [*Todaro and et al.*, 2003]

For nomenclature introduced in Section 2.2.2 are Rossby modes symmetric around the equator if (n+k) is odd and antisymmetric if (n+k) is even. Figure 2.2 shows the eigenfunctions (Θ_n) for the (1,-2), (1,-3) and (1,-4) westward propagating free planetary mode. Their amplitudes are maximizing at middle to high latitudes. [*Forbes*, 1995]

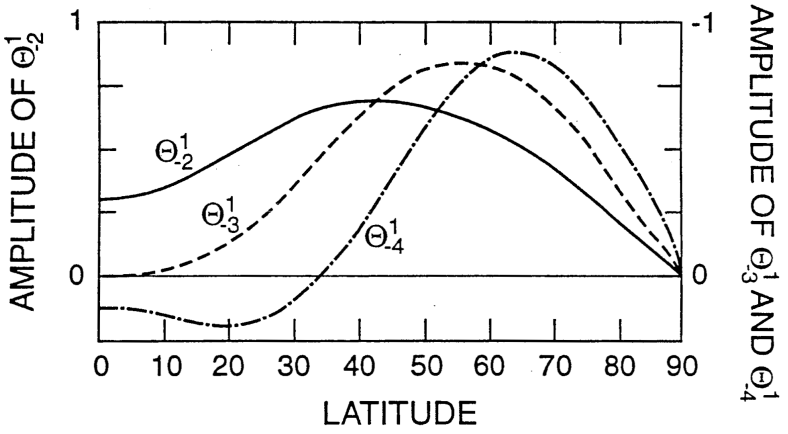

Figure 2.2: Hough modes corresponding to the first three free planetary modes of zonal wave number one. From *Forbes* [1995]

It is shown in *Volland* [1988] that for westward propagating planetary waves a solution for the eigenvalue can be found to be

$$\sqrt{\epsilon_n} = -\frac{2k}{(1-2(n+k))\nu} \tag{2.9}$$

$$\text{for periods } \tau >> \frac{-n-k(1-n-k)}{2k} \tag{2.10}$$

$$\text{with} - n > k \geq 0 \tag{2.11}$$

In the presence of wind the eigenfrequency or intrinsic frequency of the wave is Doppler shifted. Therefore the normalized frequency has to be replaced with the Doppler-shifted normalized frequency ν_D and the horizontal scale in Figure 2.1 has to be replaced by $\frac{\sigma_D}{\Omega}$.

For a mean zonal wind

$$U = B_1 \cdot a \cdot \Omega \cdot cos(\phi) \tag{2.12}$$

the Doppler-shifted frequency is

$$\nu_D = \nu - kB_1 \tag{2.13}$$

where B_1 is a constant wind amplitude.

The fact that for westward propagating ($\nu = -\frac{1}{\tau}$) planetary waves ϵ_n is positive results in

$$B_1 - \frac{\nu}{k} = U - c_p > 0. \tag{2.14}$$

The quantity c_p can be interpretet as the zonal phase velocity of the wave [*Forbes*, 1995] and is given by equation 2.14 to be:

$$c_p = -\frac{a\Omega cos(\Phi)}{k\tau} \tag{2.15}$$

Equation 2.14 stats that the propagation of planetary waves is only possible in westward flow (U<0) that is weaker then the zonal phase velocity, c_p.

If planetary waves enter an area where the wind is westward in respect to its zonal velocity (U< c_p), their intrinsic frequency and their group velocity will vanish, i.e. wave energy is absorbed. It does not matter if the background wind is eastward or westward. Important is just its direction with respect to the wave. The borders to such an area are called critical wind line or zero wind lines in the specific case of stationary planetary waves (c_p=0). [*Salby*, 1995]

Furthermore *Volland* [1988] has shown that too strong of an eastward wind (U_{cutoff}) stops the westward migrating planetary waves:

$$c_p < U < U_{cutoff} = \left[\frac{\kappa H g}{\Omega^2 a^2}\right]^{\frac{1}{4}} \cdot a \cdot \Omega \cdot \cos\phi + c_p \tag{2.16}$$

This statement is essentially the Charney-Drazin theorem, which predicts that stationary planetary waves (c_p=0) can only exist in eastward wind that is not to strong. The borders to regions with too strong of an eastward winds are called turning lines. Planetary waves encountering such a line are reflected [*Salby*, 1995].

As mentioned in, for example *Forbes* [1995]; *Salby* [1995], planetary waves are found to travel along wave-guides created by critical wind and turning lines. Planetary waves can be diffracted into a wave-guides realised between

- a region of westward and strong eastward wind
- strong eastward wind and the geometric pole
- two regions of strong eastward wind separated by less eastward wind

A wave-guide called equatorial wave-guide is created by summer westward winds and eastward jets of the winter hemisphere. Planetary waves travelling polewards while propagating vertically in this waveguide will be reflected equatorwards at the turning line of the eastward wind, and then absorbed when crossing the critical line of the westward winds. Planetary waves initially travelling upward and equatorward will encounter the critical line at even lower altitudes. Therefore vertical propagation of wave activity introduced into the equatorial wave guide has a limited altitude.

In winter solstice conditions, another wave-guide is formed by the eastward jets at mid-latitude, which weaken towards the poles. This wave-guide is called the polar cap wave-guide. Planetary wave activity reaching this wave-guide can propagate upwards with out being absorbed. Polwards travelling mid-latitude wave, whose vertical propagation is precluded above the stratopause due to strong eastward winds, can therefore penetrate into the mesosphere through the polar cap wave-guide. At mesospheric altitudes the eastward jets are weak enough that planetary waves are not longer reflected polewards. They can therefore travel equatorward into the equatorial and summer pole mesosphere.

The zonal phase velocity (Eq. 2.15) of a planetary wave is proportional to the reciprocal product of the zonal wave number and the period of the wave. Waves with small zonal velocities, according to amount, tolerate less strong westward but stronger eastward winds. Table 2.2 shows the nomenclatures of the more common planetary modes.

quasi period	**(s, n)**	**Additional Description**
2-day	(3,-3)	Mixed Planetary-Gravity; asymmetric
4-day	(2,-3)	Planetary; first symmetric
5-day	(1,-2)	Planetary; first symmetric
10-day	(1,-3)	Planetary; first asymmetric
16-day	(1,-4)	Planetary; second symmetric

Table 2.2: List of more common planetary waves. From *Forbes* [1995]

It is evident that the shorter period waves (2-5 day) resist stronger westward wind than longer waves. The wave period given in Table 2.2 refers to the actual atmospheric manifestation of a free planetary wave. To understand this one associates the atmosphere with an exterior observer like a geostationary satellite or a ground based measurement. This observer is not affected by wind and therefore observes the intrinsic frequency of the wave Doppler shifted by the wind through which the wave is moving. The observed period due to a mean zonal wind (Eq. 2.12) results in,

$$\tau = \frac{1}{\nu_D + kB_1}$$

and is shifted to longer frequencies for a mean eastward wind. For example, with an assumed background wind U($\Phi = 0$) of 10 m/s the intrinsic period of the (1,-4) planetary wave (12.5 days) for example would be observed at a period of 17.7 days. The observed period oscillates due to oscillations of the background wind. It is therefore common to refer to wave activity with a quasi period. The quasi period of 16-days for example refers to an observed 2-3 week oscillation.[*Forbes*, 1995]

Although the approach to planetary wave activity through normal modes is useful to identify ideal planetary wave characteristics, it is not always applicable to consideration of wave propagation in a realistic, i.e. non-uniform rotating and non-isothermal, atmosphere. Therefore numerical techniques are usually required. Figure 2.3 illustrates a modeled behaviour of planetary waves with zonal wave number equal to one due to typical solstice and equinox background winds. The extreme sensitivity of planetary wave response to background wind is evident. It is noted in *Murphy et al.* [2007] that the effect is strongest in the stratosphere and mesosphere and that the atmosphere does not alter the wave greatly below this region. In addition no true resonance exist in a non-isothermal atmosphere. Models show amplitude growth and phase tilt with height above 90km and non-zero vertical velocities when temperature varies with height. Models suggest moreover that phase tilt with height is not inconsistent with the concept of a free atmospheric mode and predict that an increase in wave periode goes along with increased amplitude reduction and phase tilt with height. [Forbes, 1995 and refernces within]

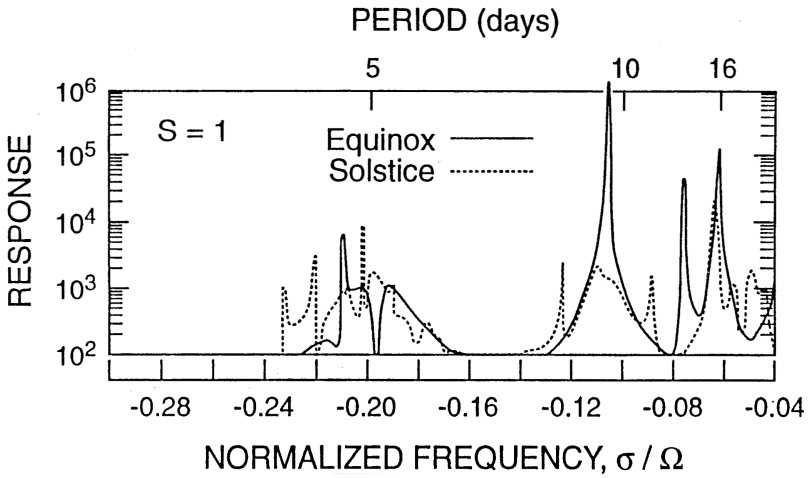

Figure 2.3: Simulated atmospheric response as a function of normalized frequency for k=1 westward propagating planetary waves, for typical solstice and equinox background wind conditions modelled by Murry L. Salby. From *Forbes* [1995]

2.3 Ozone

In this work ozone is used as a tracer for planetary waves. This section is mainly based on *Andrews* [2000] and *Brasseur and Solomon* [2005]. Due to dynamical and chemical processes, the distribution of ozone varies with time and location. Figure 2.4 maps variations of the total ozone value with latitude and season.

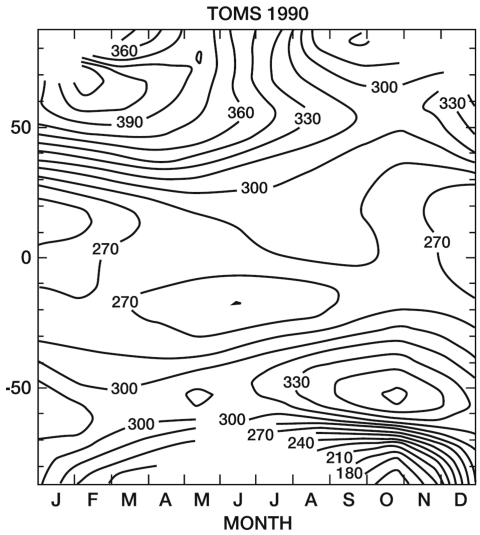

Figure 2.4: Variation of total ozone (DU) with latitude and season in the year 1990, as measured by the TOMS instrument. From *Brasseur and Solomon* [2005]

Strong seasonal variations occur north of 30° and in the Antarctic regions. The rapid decrease of ozone in the Antarctic springtime, known as the ozone hole, can be associated with polar stratospheric clouds during the cold wintertime [*Hamill and Toon*, 1991]. The highest concentration of ozone can be found in the extra tropical lower stratosphere, and ozone is most abundant at high latitudes during most seasons.

2.3.1 Ozone chemistry

The chemical reactions of ozone can be divided in oxygen-only processes, which were first described by Chapman in 1930, and catalytic processes. The k_i and j_i are the chemical rate coefficients and the photodissociation rates of the processes, respectivly.

Ozone-only processes

The only known mechanism that leads to production of ozone in the atmosphere is the fast termolecular reaction

$$\mathrm{O} + \mathrm{O_2} + M \xrightarrow{k_2} \mathrm{O_3} + M, \tag{2.17}$$

where M is an arbitrary air molecule.

The atomic oxygen that is required for this process is produced due to photo dissociation of molecular oxygen by ultraviolet radiation at a wavelengths less than 242.4 nm:

$$\mathrm{O_2} + \hbar\omega \xrightarrow{j_2} +\mathrm{O} + \mathrm{O} \tag{2.18}$$

Ozone destruction occurs through recombination, photo dissociation and catalytic processes:

- The recombination of ozone with atomic oxygen

  $$\mathrm{O} + \mathrm{O_3} \xrightarrow{k_3} 2\mathrm{O_2} \tag{2.19}$$

  is strongly temperature dependent.

- For the photolytic destruction of ozone

  $$\mathrm{O_3} + \hbar\omega \xrightarrow{j_3} \mathrm{O} + \mathrm{O_2}, \tag{2.20}$$

  a wavelength of less than 1140 nm is necessary.

Catalytic cycles

The most important catalysts (X) for the middle atmosphere are nitric oxide (NO), hydroxyl (OH) and chlorine (Cl). A typical catalytic cycle that leads to destruction of ozone and atomic oxygen, is shown in the following equations

$$\mathrm{X} + \mathrm{O}_3 \xrightarrow{k_4} \mathrm{XO} + \mathrm{O}_2, \tag{2.21}$$

$$\mathrm{XO} + \mathrm{O} \xrightarrow{k_5} X + \mathrm{O}_2, \tag{2.22}$$

The relevance of different catalytic cycles and poorly O_x-driven losses vary with altitude. Most important for the mesosphere is the hydroxyl catalytic cycle. In the upper stratosphere (around 45km) purely O_x driven losses become likewise important [*Brasseur and Solomon*, 2005].

Diurnal variation

At daytime the formation and destruction of ozone is in photochemical equilibrium. During the night the amount of ozone increases throughout the whole mesosphere as pictured in Figure 2.5.

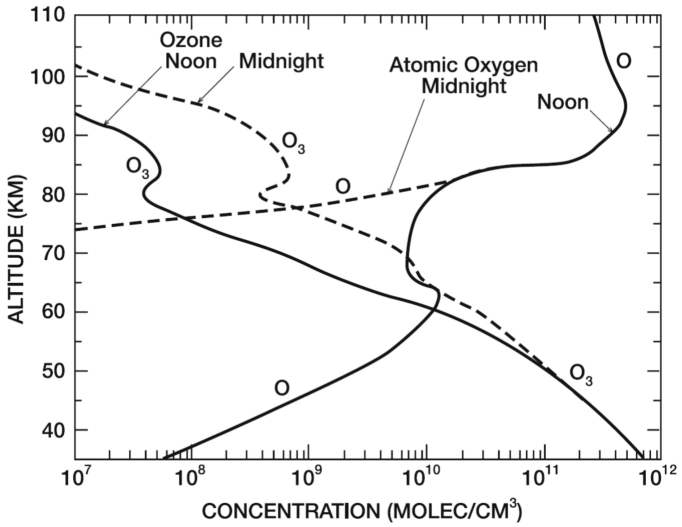

Figure 2.5: Calculated vertical distributions of ozone and atomic oxygen at noon and midnight. From *Brasseur and Solomon* [2005]

This results from the fact that photolytic destruction of ozone stops and the abundance of atomic oxygen is greater or equal to ozone. After sunrise ozone decreases again until

it reaches the photochemical equilibrium, resulting in strong diurnal variations. In the stratosphere the ozone density is high compared to atomic oxygen and the effect of solar radiation is less. Therefore smaller diurnal variations in the ozone concentration are expected.

2.3.2 Ozone distribution

Figure 2.6 shows a typical night ozone profile for June at $67,5°$S. The three maxima evident in the ozone mixing ration, at around 35, 72 and 95 km, are known as the first, the tertiary and the secondary maximum, respectively. The middle maximum is called teritary because it was discovered last.

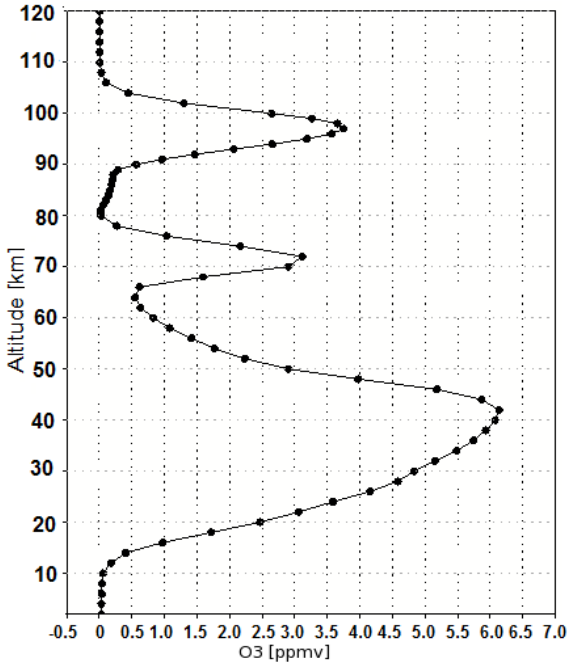

Figure 2.6: Typical ozone profile in Antarctic mid-winter (June, $67,5°$S) extracted from the COMMA-IAP model.

First maximum

As mentioned in Section 2.3.1 molecular and atomic oxygen are needed to form ozone (Eq.2.17). On the one hand, the amount of short wavelength radiation required to create atomic oxygen by depletion of molecular oxygen (Eq. 2.18) decreases downwards from the top of the atmosphere. On the other hand, the amount of O_2 decreases exponentially with altitude. By taking in addition the depletion processes of ozone due to solar radiation and

catalytic cycles into account, this leads to a maximum layer of ozone density around 20 km in the tropical region. Due to dynamics ozone is transported to the high-latitude lower stratosphere. The mixing ratio maximizes at higher altitudes ($\approx$ 35 km) because of the exponential decrease of air density. [*Andrews et al.*, 1994]

Secondary maximum

The secondary ozone maximum can be found in the upper mesosphere-lower thermosphere. The dissociation rate of molecular oxygen increases with height leading to a high concentration of atomic oxygen. In the region below 100 km atomic oxygen recombines to molecular oxygen or ozone, due to higher air density and the subsequent increasing efficiency of the three body reactions (Eq. 2.17 and O+O+M$\rightarrow$ O_2+M). This leads to a maximum in ozone mixingratio during the night at around 95 km. Nighttime values are greater then daytime values due to the absence of ozone depletion by solar radiation.

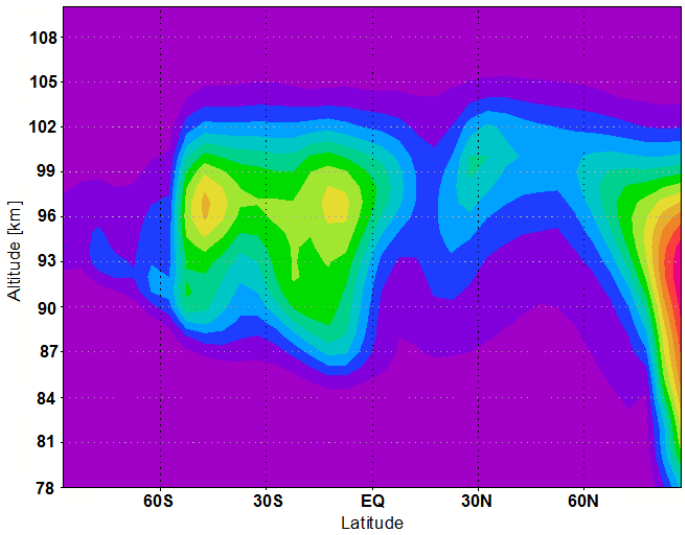

Figure 2.7: Latitudenal distributions of nighttime ozone mixing ratio at northern winter solictics between 78 and 110 km from the COMMA-IAP model.

Furthermore the secondary maximum reflects the dynamics of the vertical wind that transports oxygen. The vertical wind varies with latitude and time. At the polar regions the vertical wind is downwards in winter time and upwards in summer due to pol-pol circulation. Therefore the maximum of the second maximum is located at lower altitudes in winter polar regions as shown in Figure 2.7. [*Sonnemann et al.*, 2006]

Middle mesospheric maximum

At an altitude of around 66-76 km occurs a maximum called middle mesospheric maximum (MMM) or tertiary maximum of ozone at high latitudes just outside the polar night terminator. It is a nighttime phenomenon and extends into mid-latitudes with decreasing amplitude. The maximum goes along with a strong drop of mixing ratio above separating it from the second maximum [*Hartogh et al.*, 2004]. In contrast to normal conditions, where a concentration smaller then 1 ppmv would be expected, the maximum ozone mixing ratio reaches about 2-4 ppmv [*Sofieva and et al.*, 2009] at the MMM.

Figure 2.8 shows a latitude-seasonal section of nighttime ozone mixing ratio at an altitude of 72 km calculated by means of the COMMA-IAP model. The occurrence of the middle atmospheric maximum of ozone mixing ratio is clearly visible near the polar night terminator, varying in latitude with the position of the polar night terminator.

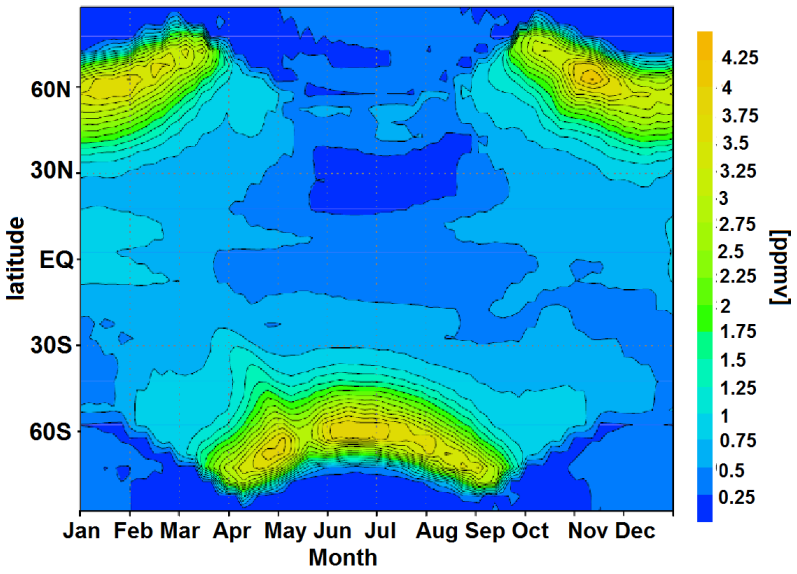

Figure 2.8: Latitude-seasonal section of nighttime ozone mixing ratio at an altitude of 72 km calculated by means of the COMMA-IAP model. From *Hartogh et al.* [2004]

As mentioned by Sonnemann et al. [2007 and references therein] the following effects related to a stongly incresed solar zenith angle lead to the occurence of the middle mesospheric maximum just outside the polar night terminator:

- an increasing solar zenith angle leading to stronger decline of the dissociation rate of water vapour then that of molecular oxygen

  The decline of the dissociation rate of water vapor reduces the production of hydrogen radicals from water vapor and results in less absoption of atomic oxygen by radiation

produced hydrogen radicals. This, and the less strong decline in the dissociation rate of molecular oxygen, leads to a greater amount of atomic oxygen present after sunset creating ozone. [*Marsh et al.*, 2001]

- very slow decrease of the ozone dissociation rate with increasing solar zenith angle and a non-zero ozone dissociation rate outside the polar night terminator

  All photolysis is stopped during polar night conditions, but outside the polar night terminator the depletion of ozone is non-zero due to a few hours of sunlight. This, and the very slow decrease of the ozone dissociation rate with the solar zenith angle, reduces the ozone concentratiois during daytime forming atomic oxygen. After sunrise the atmoic oxygen returns to ozone. [*Hartogh et al.*, 2004]

The early winter peak is modelled to be 2 km higher then the late winter peak and observations show strong variations in amplitude in order of weeks [*Sonnemann et al.*, 2007] and strong modulations due to planetary scale oscillations [*Sonnemann et al.*, 2006]. In *Sofieva and et al.* [2009] a decrease of the MMM due to energetic particles precipitation events such as solar proton events are mentioned and observed.

2.3.3 Ozone as a tracer

In contrast to the characteristic time scale of air motion ($\approx$ one day) the photochemical lifetime of ozone varies rapidly with altitude. In the lower stratosphere ozone is controlled by dynamical influences because it has a photochemical lifetime of weeks. At around 30 km the photochemical lifetime is in the order of 1 day, at the stratopause around 1 h, and it decrease to the order of minutes in the mesosphere [*Salby*, 1995]. Therefore upper stratospheric and mesospheric ozone is often considered to be a poor tracer of dynamics. Figure 2.9 presents the altitude dependence of chemical and dynamical lifetimes of the oxygen species.

It is true that upper stratospheric and mesospheric ozone do not trace global movements of a parcel of air well. Due to its short chemical lifetime a high mixing ratio of ozone produced locally (e.g. by a factory) will rapidly be equilibrated level to the photochemical equilibrium value of the surrounding air the parcel is travelling though. However, ozone can be used to trace a wave. To understand this one considers a wave in time at a constant altitude and latitude in an isothermal atmosphere with temperature T. The wave can be described as parcels of air coming into a location (x) periodically from the area above and under the location. This description is equivalent to the conventional description of a wave as parcels moving up and down in the atmosphere. The parcel of air originally located at the location x is in equilibrium with the surrounding and has temperature T, ozone mixing ratio μ, pressure p and density ρ. The parcel of air rising up from a lower altitude ($p_1 = \rho_1 \cdot T > p$, $\mu_1(T)$) expance and cools adiabatically to a temperature $T_1 < T$ and expands. Due to the lower temperature and the short chemical lifetime, the ozone mixing ratio of the parcel changes immediately to a now steady state mixing ratio ($\mu_1(T_1) \neq \mu(T)$).

The mixing ratio and the temperature change again, when a parcel from altitudes above ($p_2 < p, \mu_2(T)$) sinks, compresses and heats up to a temperature ($T_2 > T$). Hence a wave leads to periodic variations in pressure and density as well as temperature and ozone mixing ratio.

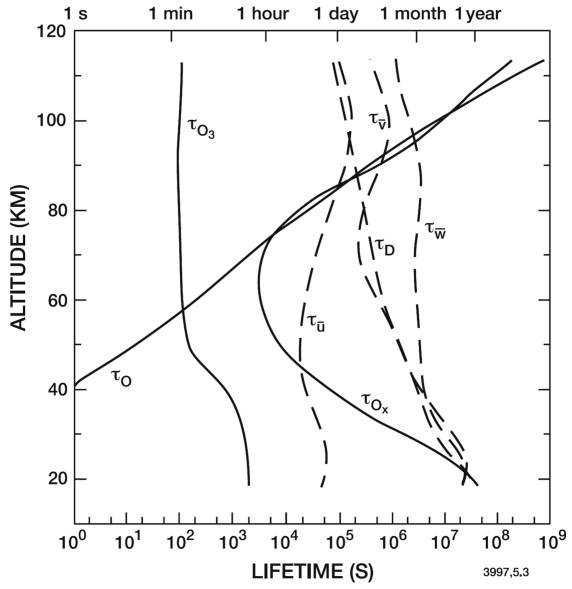

Figure 2.9: Daytime photochemical lifetimes of O_x, O_3, and O, and characteristic transport lifetimes for mid-latitude winter, from the model of Garcia and Solomon. τ_D represents the vertical diffusive lifetime (mean vertical mixing), assuming a vertical scale height of 5 km. $\tau_{\bar{u}}$, $\tau_{\bar{v}}$ and $\tau_{\bar{w}}$ represent the time constants for transports by the zonal, meridional, and vertical winds at middle latitudes, assuming characteristic scales of 1000, 1000, and 5 km, respectively. From *Brasseur and Solomon* [2005]

Temperature dependence of the ozone mixing ratio

At a first approximation the relation between temperature variations and variations of ozone mixing ratio can be modelled by considering just ozone-only processes. The equilibrium mixing ratio of ozone can than be calculated in steady state to be [*Andrews*, 2000]:

$$\mu = \frac{[\mathrm{O_3}]}{[\mathrm{M}]} = \frac{[\mathrm{O_2}]}{[\mathrm{M}]} \sqrt{\frac{k_2}{k_3} \cdot \frac{j_2}{j_3} \cdot [\mathrm{M}]}, \tag{2.23}$$

where $[O_2]$ and [M] are number density of molecular oxygen and air. The assumption of a steady state is valid if the period of the wave is much longer then the chemical lifetime of ozone. This is the fact for planetary waves. The k_i rate coefficients are given to be [*Sander*

and et al., 2006]:

$$k_2 = 6 \cdot 10^{-34} \cdot \left(\frac{T}{300}\right)^{-2.4},$$
$$k_3 = 8 \cdot 10^{-12} \cdot \exp\left(\frac{-2060}{T}\right).$$

The photodissociation rate coefficients j_i are chosen at one fixed altitude. In addition, they will to first approximation, have a similar temperature and solar dependence so that their ratio is relatively constant. Similary the night-time staedy state chemical rate coefficients have a strong temperature dependence. We use this primitive model only used as an indecation of the wave induced variations one might observe in the ozone mixing ratio. For a wave, the percentage variation in temperature was assumed equal to the percentage density fluctuation, but 180° out of phase [*Vincent*, 1984]. The number density of molecular oxygen was assumed to be 20% of the air density. The calculated variations of the ozone mixing ratio for a variation in temperature are pictured in Figure 2.10 for an altitude of 45km and 70km, respectively. The values used and calculations can be found in Appendix C.

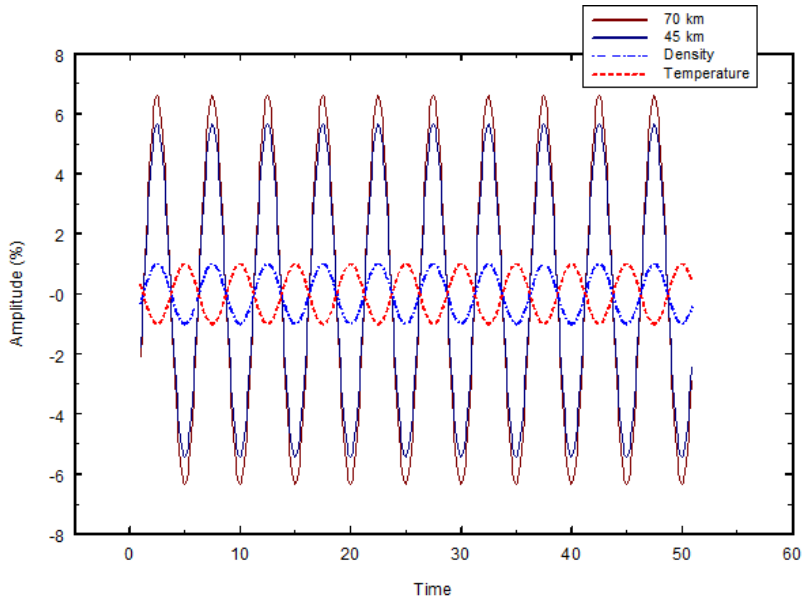

Figure 2.10: Modeled ozone mixing ratio variation at 45 and 70km due to a temperature variation of 1%.

This model indicates that the percentage of ozone mixing ratio variations is 6 times stronger than the temperature variance, anti-correlated and approximately constant with height. Ozone is therefore a good tracer for planetary wave motion in the upper stratosphere and mesosphere. However changes of the mean ozone concentration with altitude

and time has to be taken into account when construing the development of wave amplitudes. In addition, effects of hydrogen, nitrogen, and chlorine chemistry as well as time dependent influence of solar and cosmic radiation should be taken into account to improve the model.

2.4 Ground-based millimeter-wave remote sensing

As described in *Jarchow* [1998] ground-based millimetre-wave remote sensing is based on the fact that the rotational energy levels of molecules are quantized and each type of molecule therefore emits and absorbs characteristic wavelengths. Rotational states have low energy of excitation and can therefore be exited thermally due to collisions among the molecules. Exited molecules radiate the rotational energy away through spontaneous or induced emission. This radiation has a millimetre or submillimetre wavelength and can be seen as a complex line spectra at the ground by measuring the electromagnetic irradiance (I_σ). Gases with unique spectral lines can then be detected by their characteristic emission. Advantages of ground-based millimetre-wave remote sensing are that it is continuous, nearly weather independent and has a temporal resolution of a few minutes for some gases.

2.4.1 Measuring principle

As described for expamle in *Liou* [2002] is the line width of a spectral line broadened by pressure and Doppler broadening in addition to its natural line width. Doppler broadening describes the effect that due to thermal motion of the molecule, the emitted frequencies are shifted randomly around the monochromatic frequency of the spectral line. The Doppler line shape is given by the shape factor,

$$\mathrm{f}_D(\Sigma - \Sigma_0) = \frac{1}{\Delta\Sigma\sqrt{\pi}} \exp\left[-\left(\frac{\Sigma - \Sigma_0}{\Delta\Sigma}\right)^2\right], \tag{2.24}$$

with a half width at half maximum (HWHM) of

$$\Delta\Sigma_D \cdot \sqrt{ln(2)} = \frac{\Sigma_0}{c}\left(\frac{2k_BT}{m}\right)^{1/2} \cdot \sqrt{ln(2)}. \tag{2.25}$$

Σ_0 is the wave number of an ideal, monochromatic line, k_B is the Boltzmann constant and m the mass of the molecule. Pressure broadening or collision broadening takes into account that the lifetime of an energetic state is shortened due to collisions. The frequency of collisions increases with pressure (p) and temperature (T). The line shape factor of pressure broadening can be modelled with the Lorentz form,

$$\mathrm{f}_p(\Sigma - \Sigma_0) = \frac{1}{\pi}\frac{\Delta\Sigma_C}{(\Sigma - \Sigma_0)^2 + \Delta\Sigma_C^2}. \tag{2.26}$$

with a HWHM of

$$\Delta\Sigma_C = \Delta\Sigma_0 \cdot \frac{p}{p_0}\left(\frac{T_0}{T}\right)^{-\alpha}, \tag{2.27}$$

where $\Delta\Sigma_0$ is the half-width at standard pressure (p_0) and temperature (T_0). The index α depends on the type of molecule and ranges from $\frac{1}{2}$ to 1. For ozone α it is 0.76 [*Brasseur and Solomon*, 2005].

The Voigt form,

$$\mathrm{f}_v(\Sigma - \Sigma_0) = \int_{-\infty}^{\infty} \mathrm{f}_p(\Sigma' - \Sigma_0)\ \mathrm{f}_D(\Sigma' - \Sigma_0)\ d\Sigma' \tag{2.28}$$

models Doppler as well as pressure broadening. It is a mixture of the Lorentz and the Doppler line form and reduces to the Doppler and Lorentz shape for $\Delta\Sigma_D \to 0$and $\Delta\Sigma_C \to 0$, respectively. It is not possible to solve this function analytically but a very accurate approximate solution exists which can be solved numerically. (See [*Jarchow*, 1998]).

Figure 2.11 shows the development of the HWHM of Doppler and pressure broadening for ozone with altitude for a model atmosphere in June and November. It is evident that the altitude of the cross over changes with the season of the year and is located highest in summer.

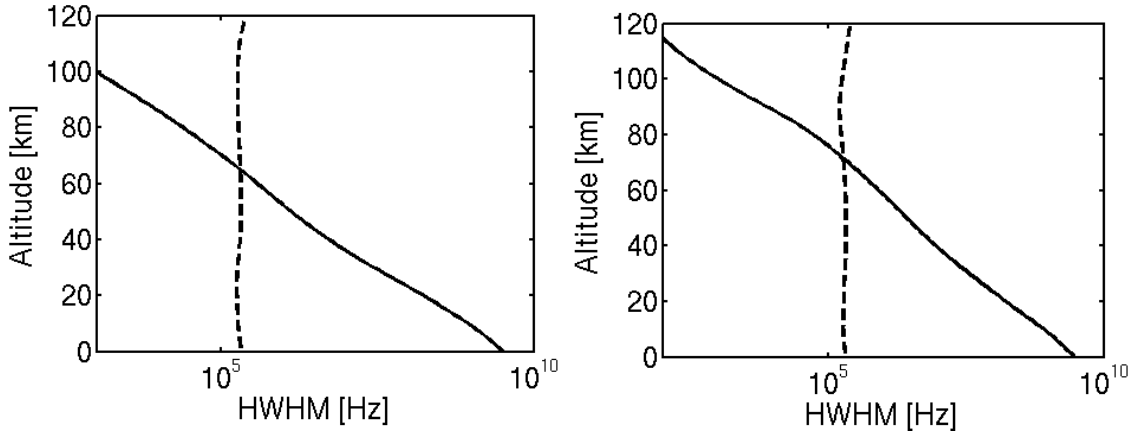

(a) (b)

Figure 2.11: Development of pressure (solid line) and Doppler (dashed line) broadening with altitude for ozone in a model atmosphere (see AppendixD) in (a) June and (b) November.

Due to pressure broadening each molecule emits a characteristic line shape depending on the height at which it is located. As long as pressure broadening is dominant, the form of a spectral line contains information about the distribution of the gas with height because the line width ($\Delta\Sigma_c$) is linear in pressure, and pressure decreases exponentially with altitude in the atmosphere. Figure 2.12 shows in which way the shape of a spectral line changes with altitude.

The spectrum measured at the earth surface is the sum of all the emitted spectra components. This means that each component represents an unique line shape, and that

its contribution to the sum is related to the quantity of molecules emitting this line shape. In other words by knowing the contribution of each component, the altitude profile of the gas is known. The contribution of each component is found by modelling the sum of all spectral line forms and optimizing their contribution so that the sum fits best with the measured spectra at the ground.

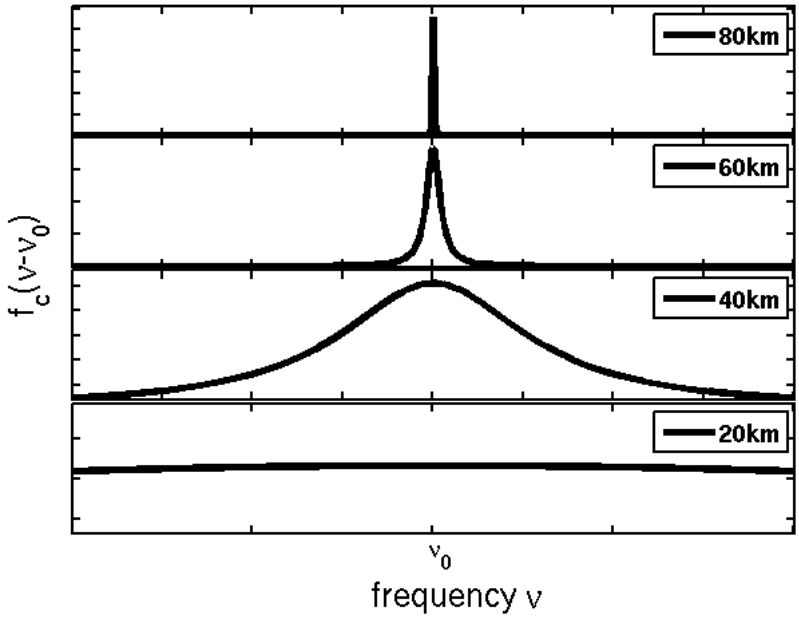

Figure 2.12: Line shape due to pressure broadening at different altitudes (20, 40, 60, 80km)

2.4.2 Calculation of the altitude profile

The correlation between the measured spectra and the corresponding altitude profile of the gas is described by the forward model. As described in *Jarchow* [1998] the model can be separated into a radiation transfer model and an instrument model. The radiation model describes the correlation between the mixing ratio profile and the corresponding spectra. It contains both quantum-mechanical processes of absorption and emission, and models radiation transfer through the atmosphere using the radiative transfer equation:

$$\frac{dI_\sigma}{dx} = j_\sigma - \mu_\sigma \cdot I_\sigma, \tag{2.29}$$

as a starting point. This equation describes quantitatively the fact that a specific irradiation (I_σ) of the frequency σ changes while passing through the atmosphere (space coordinate x) due to attenuation by absorption (μ_σ) and amplification by atmospheric emission (j_σ). The instrument model considers instrumental effects and describes the difference between the real and the measured spectra. Both models are described in *Jarchow* [1998] in great detail and will not be repeated here.

The forward model has to be inverted to calculate the altitude profile from the measurement data. Due measurement errors, the inversion of the instrumental model is not unique and it is not possible to find an exact solution. Therefore approximate solutions, which minimize the deviation between the measured and the calculated spectra, have to be found. The least square fit solution creates an excellent fit of the spectra, but can result in unphysical profiles. Therefore an a priori profile has to be used to control the fitting of the spectra by allowing only small differences between the solution (calculated profile) and the a priori. This method is called optimal estimation. The formal description is documented in *Jarchow* [1998] and *Rodgers* [1976]. For the inversion this method was used in an iteration loop, where the calculated profile of the first calculation was used as the a priori for the next one until the difference between the measured and the calculated spectra was minimized. This method creates unique and stabile solutions, i.e. altitude profiles.

To interpret the calculated profile it is important to know its height resolution. This information is provided by the averaging kernel matrix. The averaging kernel matrix characterizes how a change at a single height is interpreted by the fitting procedure as correlated changes at adjacent altitudes. That is, it shows the height responce or height resolution of the fitted profile at each altitude. Each i-th altitude response is represented by the i-th column of the matrix. In an ideal case the averaging kernel matrix would be an unit matrix, resulting in a profile with infinit height resolution. By plotting the averaging kernel matrix over altitude each curve of the averaging kernel matrix illustrates the response to the change at one specific height. An example of a typical averaging kernel matrix and how a changes of the measured profile are reflected in the solution can be seen in Figure 2.13.

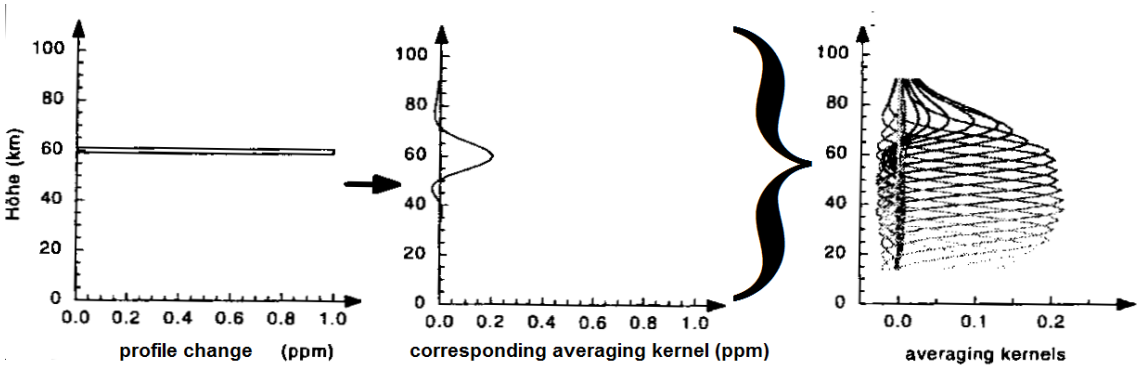

Figure 2.13: Profile change of 1 ppm at 60 km represented by a delta function (left), change in the solution, i.e. average kernel for 60 km (middle), average kernel matrix (right). From *Jarchow* [1998]

On the left a delta function represents a profile change of 1 ppm at 60 km and the corresponding averageing kernel (middle) expresses the change in the solution. The averaging

kernel matrix (right) is the collection of all averaging kernels. High sensitivity to changes in the true profile is represented by a thin curve with a high amplitude.

2.4.3 Limits

The averging kernel matrix is mostly effected by

- the radiometer formula
- Doppler broadening (high altitudes)
- baseline of the instrument (low altitudes)

The radiation formula describes the effect that the sensitivity changes with height due to the width of the sespectral line. At low altitudes the width of the emitted spectral line is very broad and therefore changes can be observed at all frequency channels. At higher altitudes the line shape is thin and changes can only be registered by frequency channels near the line center. This results in a linear sensitivity decrease with height.

Doppler broadening gets more and more dominatant with height and becomes the main contribution to the voigt shape at the height where Doppler and pressure broadening are equal. This results in higher noise sensitivity of the inversion because the correlation between line width and height is lost [*Hartogh and Jarchow*, 1994]. *Jarchow* [1998] states that a retrieval of the profile is possible up to 5 km above the altitude where Doppler and pressure broadening are equal. The effect of Doppler broadening and the radiometer formula are shown in Figure 2.14.

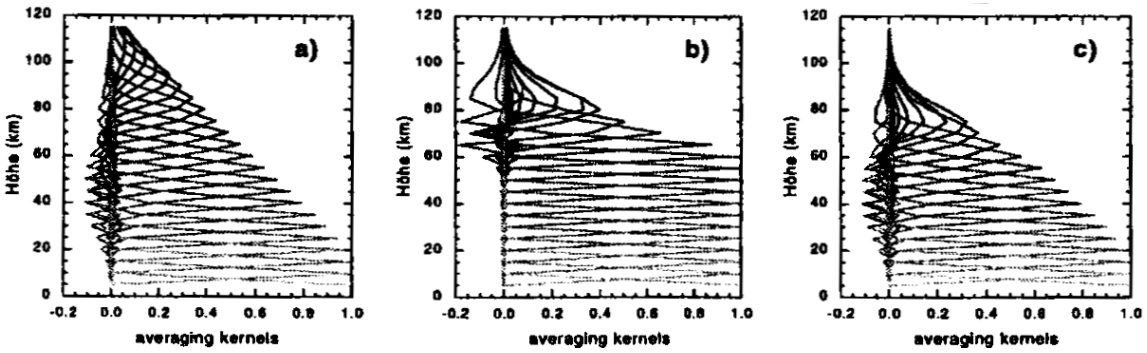

Figure 2.14: Impact of the a) radiometer formula, b) Doppler broadening and c) combination of radiometer formular and Doppler broadening on the Average Kernel matrix. From *Jarchow* [1998]

For low altitudes the sensitivity gets small due to the fact that the line shape becomes very broad so that it is not longer possible to distinguish between baseline and noise of the instrument and the spectral line. See Figure 4.8.

Chapter 3

Instrumentation

In this thesis ozone measurements from the Norwegian Polar Institute's (NPI) Troll research station at the Antarctic Plateau were used. The station is located inland at 72° south and 2° east and an altitude of 1275m. It lies deep within the polar vortex during Australian winter. For the measurements of the ozone spectra the millimetre wave spectrometer ARON (Antarctic Radiometer for Ozone and Nitric oxide) was used. The viewing angle of ARON is at an azimuth of 288° and an elevation of 30°, which corresponds to an atmospheric transmission of > 65 [*Espy et al.*, 2006].

3.1 Design

ARON observes nitric oxide (NO), ozone (O_3) and carbon monoxide (CO) by detecting both the 250.81 (NO), the 229.575, 249.96196 and 249.7886 (O_3) and the 230.538 (CO) GHz lines. The Design of ARON is described in *Espy et al.* [2006]. It consists of a radiometer front-end coupled to two Chirp Transformation Spectrometers (CTS); a narrow band (40.0 MHz) CTS with high-resolution ($\sim$ 10 kHz) and a wide band (220 MHz) CTS with moderate-resolution ($\sim$ 14.5 kHz). Figure 3.1 shows a schematic diagram of the radiometer. For calibration the incoming radiation is directed into a three-way chopper which selects the signal from a 60 K cold load, a 300 K warm load or the atmosphere. The warm and the cold loads calibrate the measured brightness temperature of the spectra, and the instrument obtains a calibrated sky spectrum every 17.5 s. They are detected anew for each measurement to compensate for shifts in the instrument. The incoming signal is polarised and one polarisation is directed into a Martin-Pupett Sideband filter with maximises transmission, with losses < 0.12 dB, at the 230 and 250 GHz signal bands and provides an image rejection > 21 dB with losses < 0.12 dB. The unwanted polarisation is directed into a 4K beam dump. A path modulator, a mirror mounted on a loudspeaker in order to make it vibrate, creates small but rapid changes in the optical path length of the system. It is installed after the Martin Pupett to minimise the baseline of the instrument by reducing standing waves.

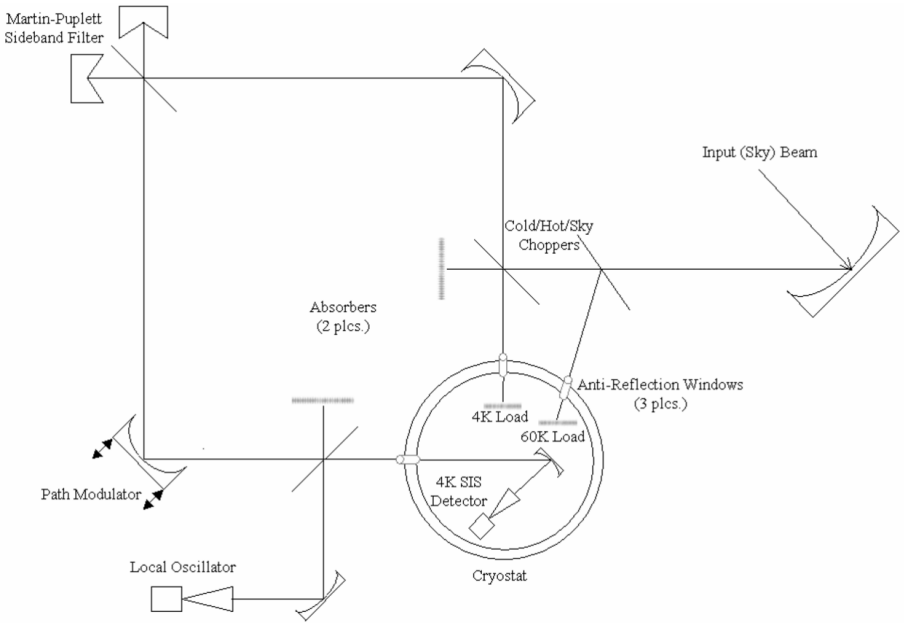

Figure 3.1: Schematic diagram of ARON showing the major system components of the radiometer. From *Espy et al.* [2006]

For frequencies above 10 GHz direct electrical signal processing is difficult, and for frequencies above 150 GHz no electronic amplifyers can be found. Therefore the signal has to be converted to a lower frequency to apply electronic spectrum analysis. The conversion to lower frequencies is done by mixing the original frequency (ω_{RF}) and a fixed frequency (ω_{LO}) of a local oscillator. The mixer produces a non-linear IV-charateristic, which can be expanded. The squared term of the expansion is most important. It is the squared sum of the original and the local oscillator signal ($A \sin \omega_{RF} + B \sin \omega_{LO}$). This term contains both

- a direct voltage component, $\frac{1}{2}(A^2 + B^2)$,
- the doubled RF- and LO-frequencies, $-\frac{1}{2}t \left[A^2 \cos(2\omega_{RF}) + B^2 \cos(2\omega_{LO})\right]$,
- sum and difference of these two frequencies, $AB \left[\cos(\omega_{RF} + \omega_{LO}) + \cos(\omega_{RF} - \omega_{LO})\right] t$.

The local oscillator frequency is set near to the frequency of the signal so that the difference of the two frequencies, known as the intermediate frequency (ωIF), is small enough to be amplified. The intermediate frequency is not unique because two frequencies originally at $\omega_{RF_1} = \omega_{LO} + \omega_{IF}$ (upper sideband) and $\omega_{RF_2} = \omega_{LO} - \omega_{IF}$ (lower sideband) are converted to the same intermediate frequency. See Figure 3.2(a).

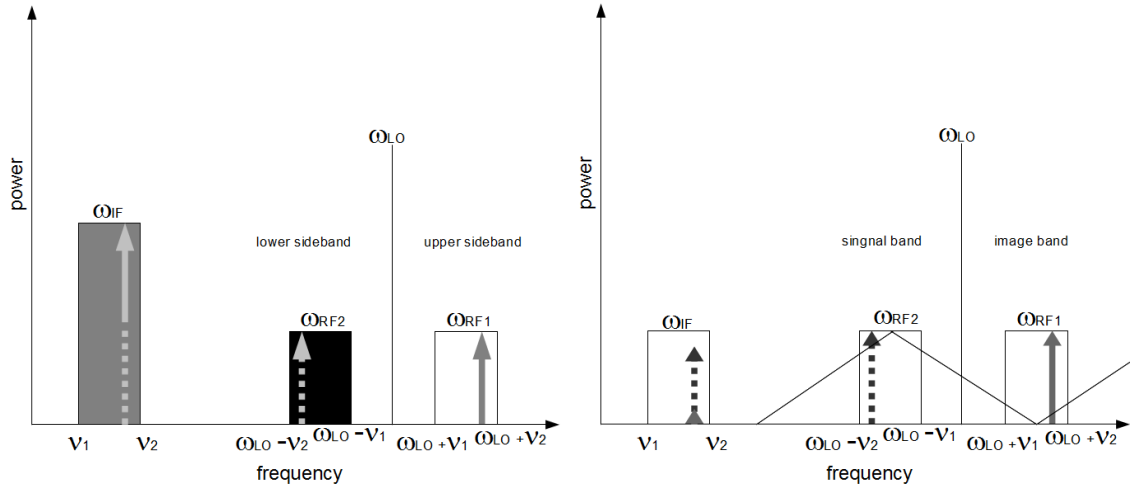

Figure 3.2: Frequency transformation: Both side bands are converted to the same intermediate frequency band (a) but one can be eliminated with the Martin-Pupett filter frequency $\omega_{MP} \propto cos^2$ (b)

In ARON the original signal is combined with one of two independent local oscillators at 255.25992 and 225.17784 GHz. This convertes the NO, CO and O_3 lines of interest from the lower/upper sideband to an intermediate frequency at approximately 5 GHz with a band width,$\nu_2 - \nu_1$ of $\sim$ 2GHz. The Martin-Pupett sideband filter attenuates the image band (unwanted sideband) while passing the signal band (wanted sideband) with a minimum of attenuation, as shown in Figure 3.2(b). This combined with the absence of bright emission lines in the image band eliminates unwanted spectral interference in the spectra of interested. The new signal is amplified around 5 GHz with a bandwidth of 2 GHz.

Afterwards the signal is split and relayed to the wide and the narrow band Chirp Transform Spectrometer (CTS). Inside the CTS the input signal is mixed with a chirp pulse that translates the frequency differences between the Fourier components of the input signal to time differences. The CTS technique, instrumentation and the formula has been described in *Hartogh and Jarchow* [1994] and will not be repeated here. In ARON the analog output of the CTS is digitized by four analog to digital converters (A/D) with a clock rate of around 69 μs, i.e. approximately 14.5 kHz resolution. ARON's wide band spectrometer measures the bright ozone lines at 249,79 and 249,96 GHz when the local oscillator is set to 255.3 GHz. When the local oscillator is manually switched to 225.2 GHz, the CO line at 230.54 GHz is observed by the wide band CTS. The observation schedule requires switching to the CO line between 11-13 GMT in winter and 12-14 GMT in summer.

3.2 Instrumental foibles

Instrumental errors such as incorrect temperature calibration, frequency calibration, A/D converter error and baseline were corrected by the previous master student Ole Martin Christensen and are described in his theses [*Christensen*, 2009]. It should be noticed that the frequency calibration leads to uneven channel spacing (17.6 kHz $< \Delta f <$ 38.7 kHz). This, and the fact that interaction between standing waves lead to a non-sinusoidal baseline results in the fact that a total number of 25 baseline periodicities had to be used to assure removal of the baseline. The use of a polynomial fitting of the baseline as an alternative should result in fewer free parameters while delivering a similar result.

3.2.1 False spectra

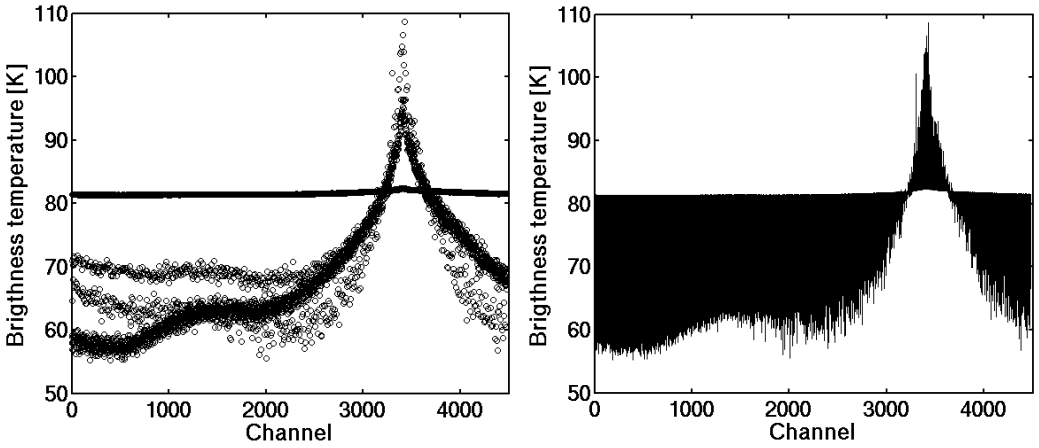

(a) (b)

Figure 3.3: False spectra (a) point plot, (b) line plot. Each A/D seems to produce its own.

ARON produces a wide range of false spectra including

- spectra standing upside down
- only random spikes
- just noise
- spectra where each A/D converter seems to produce its own spectrum

These false spectra have to be filtered out to assure a good signal to noise ratio in the average and assure a stable realistic ozone profile. Most of the time false spectra

occure only sparedicly. Therefore it is generally assured that hourly averages still supply a good signal to noise ratio because each average period still contains around 200 individual measurements. Figure 3.3 shows the false spectra where each A/D converter seems to produce its own spectra. Other examples of the false spectra mentioned above are presented in appendix E.1.

Chapter 4

Analysis

Measurement data from ARON were provided by the British Antarctic Survey [*BAS*]. The Atmospheric Radiative Transfer Simulator Arts 1.0.208 [*Buehler et al.*, 2005, 2007] was used to simulate the forward model. The inversion and sensor modelling were done with the add-on package Qpack [*Eriksson et al.*, 2005]. The necessary adjustments and corrections to run the inversion were done by Ole Martin Christensen and are described in his thesis [*Christensen*, 2009]. These parameters were used for the inversions done in this work, althrough it was nessary to extend the seasonal range of a priori profiles. Details of the a priori profiles used can be found in Appendix D.

4.1 Spectra

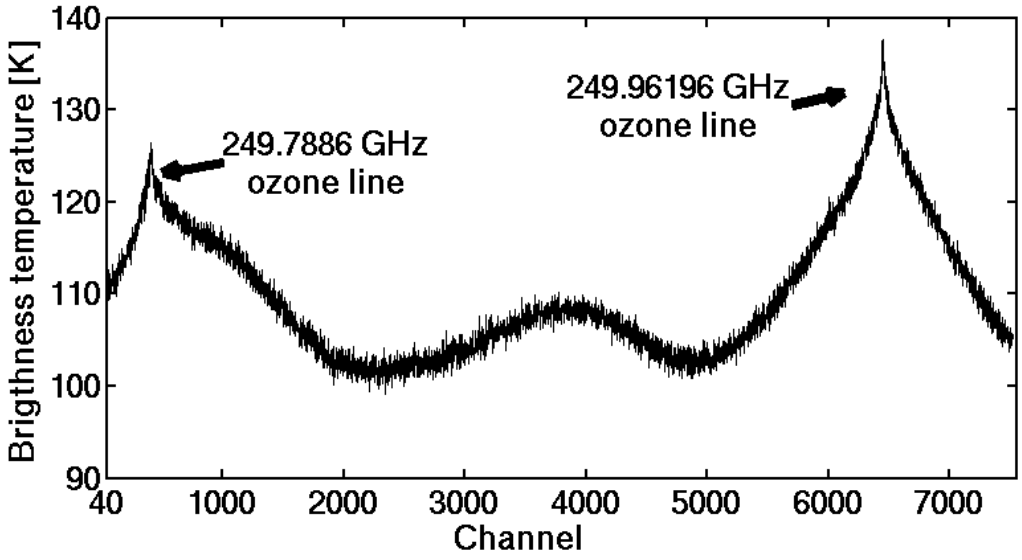

Figure 4.1: Ozone spectra of the broad band CTS of ARON, day 158 year 2009

A sample spectra measured by the broadband (220 MHz bandwidth, 14,5 kHz resolution) CTS of ARON around a frequency of 249.9 GHz is shown in Figure 4.1. The 249.7886 GHz and 249.96196 GHz ozone lines are evident. In the pictured spectrum the baseline is visible as a lower third peak between the two lines and as a "broadening" under the two peaks. In contrast to the first peak the whole peak shape of the second peak is covered by the measurement. Therefore the second peak (channel 3042 -7518) was used for the inversion. To reduce the noise level and insure stabile inversions the spectra were averaged over one hour. Figure 4.2 shows a measured spectrum, an averaged spectrum, the baseline corrected and the fitted average spectrum.

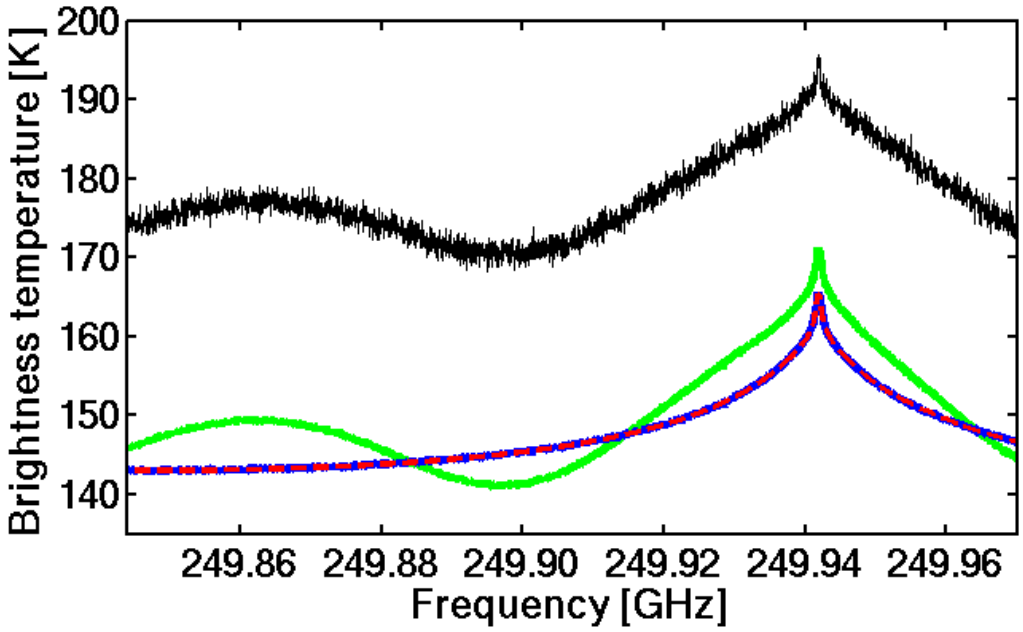

Figure 4.2: Sample of a measured (black), averaged (green), baseline corrected (blue) and fitted (red dashed) 249.9 GHz ozone peak; day 152, year 2009

4.1.1 Connection inverted profile and spectral peak

Typical profiles for June and December and the corresponding spectra are shown in Figure 4.3. The connection between line shape and profile is evident by comparing the profiles in Figure 4.3(a) with their corresponding peaks in Figure 4.3(c). The effect of pressure broadening, discussed in Section 2.4.2, is clearly evident in the spectra, as is the shape, narrow peak due to ozone at altitude above 65km, where the Doppler component begins to become appreciable. This narrow peakshape disappears during daytime due to photolytic ozone depletion. In summer the zenith angle of the sun becomes higher and the duration of a day longer. Ozone depletion can therefore take place at lower altitudes in summer than in winter, resulting in a broader peak during the summer days than found during the

winter days.

The spectra for June, presented in Figure 4.3(b) have a much higher brightness temperature offset than the one in December. This offset is assumed to be caused by tropospheric temperatures differing strongly from the a priori. Temperatures in the troposphere are strongly influenced by daily weather conditions such as clouds, rain or snow storms. The a priori profiles used are constant monthly values from 2001 and do not incorporate special weather conditions. During the retrieval this offset is therefore interpreted as a very flat peak that would correspond to tropospheric ozone. This leads to the unrealistic high ozone value below 10 km in the corresponding profiles for June, shown in Figure 4.3(c). However, as discussed in Section 2.4.3, there is little information in the spectra below 30km, and the profile below there is documented by the a priori.

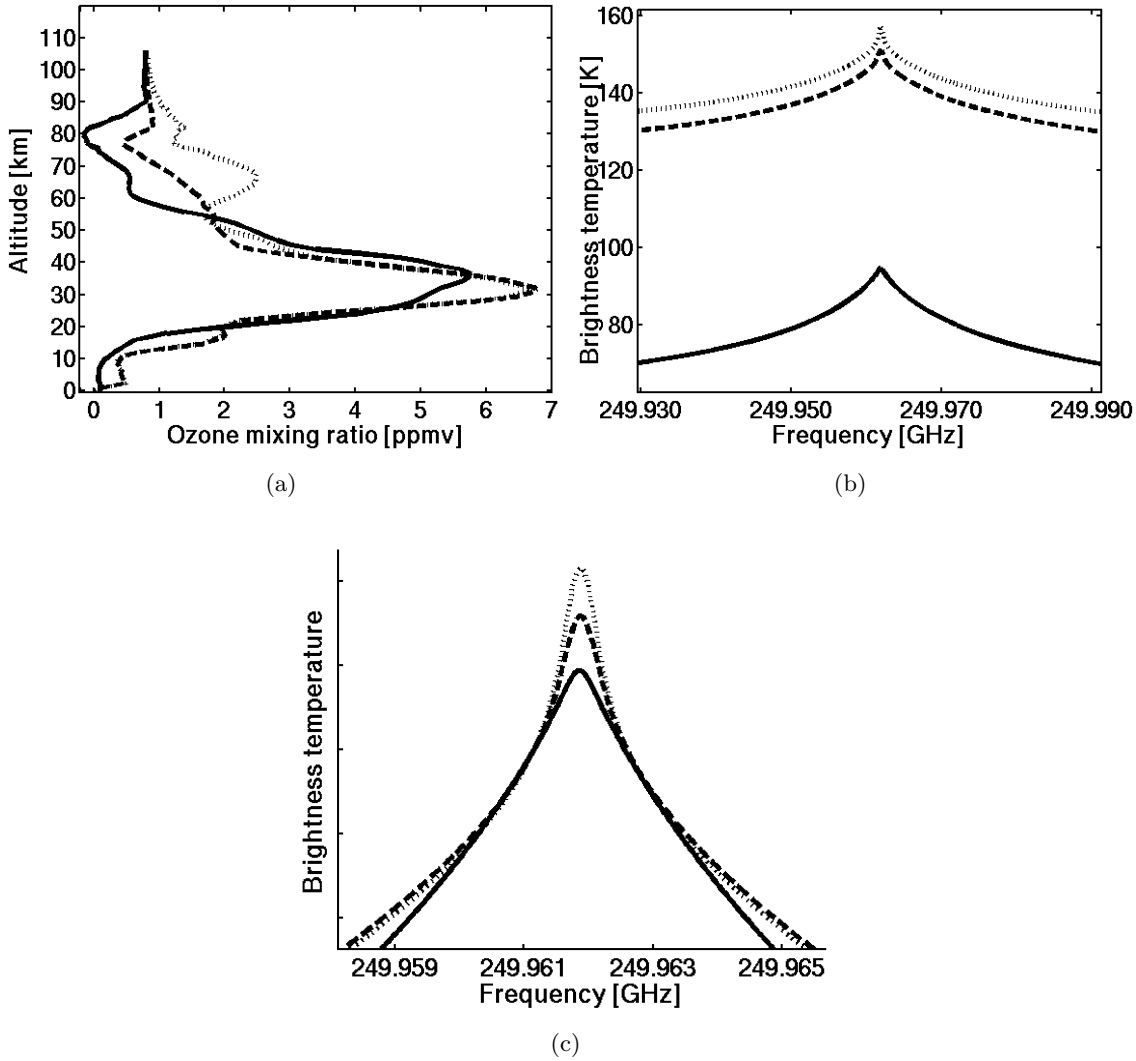

(a) (b)

(c)

Figure 4.3: Comparison of ozone (a) profiles and (b), (c) spectra for June day (dashed) and night (dotted) and December (solid)

4.1.2 Peak mismatch

In [*Christensen*, 2009] a peak mismatch between the baseline corrected and fitted spectra is mentioned. Figure 4.4 shows such a peak mismatch. Possible reasons for this include a wrong base line fit, error in frequency calibration, an error in the backend modelling and Doppler shift due to winds in the mesosphere.

Due to the geometry of ARON (azimuth = 288°) the Doppler effect caused by zonal winds can play a role. The top part of the peak corresponds to high altitude ozone because the peak is thinnest where Doppler broadening becomes dominant. Figure 2.11 shows the development of Doppler and pressure broadening for ozone. The cross over of the broadenings occures at approximatly 70 km. Therefore Doppler shift should be found due to winds above this altitude at nighttime in winter. The amplitude of zonal wind decreases from the mesosphere to the thermosphere and therefore mesospheric winds are assumed to dominate any peak shift. In summer and during the daytime in winter when the high altitude ozone is photo-dissociated, winds at slightly lower altitudes could cause a Doppler shift of the peak. Mesospheric and upper stratospheric winds as a function of season and time of day were used to interpret whether Doppler shift could be responsible for the peak shift.

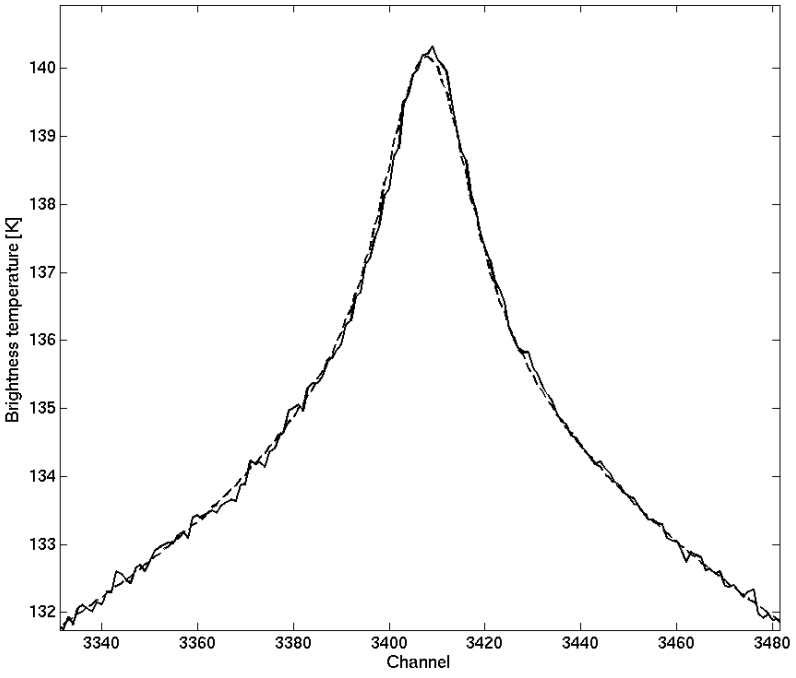

Figure 4.4: Peak mismatch of the measured (solid) and the fitted (dashed) spectrum

The maximum calculated Doppler shift during the year was found to be of the same magnitude as the resolution of ARON's broadband CTS using wind measurements at Rothera [*Hibbins et al.*, 2005]. The peak should be shifted to higher frequencies in winter due to mean eastward wind and the westward directed viewing direction of ARON. In summer a shift to lower frequencies due to a mean westward wind should be observed. The observed shift of the measured spectra, presented in Figure 4.5, shows the right tendency but the Doppler shift due to mean winds should be greatest June and not in March.

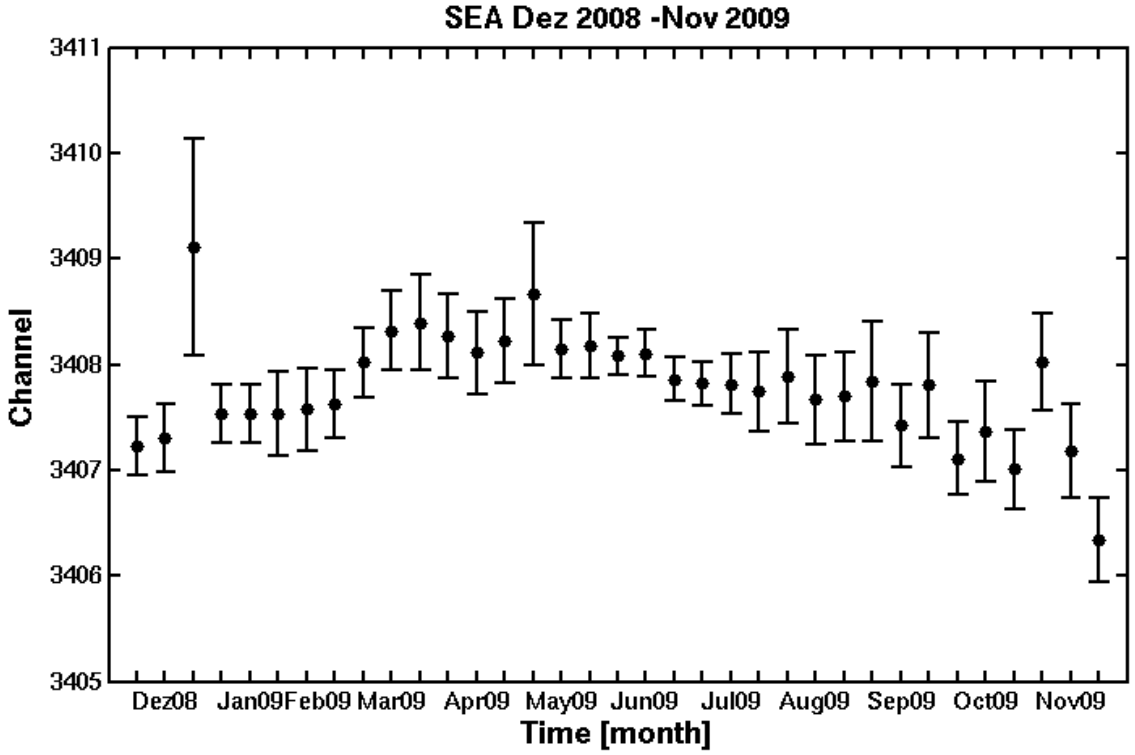

Figure 4.5: Shift of the peak center during the year, December 2008-November 2009

To assess if there are underlying diurnal or sub-diurnal variations such as a moving baseline, a Doppler shift due to tides, or altitude changes of the highest ozone value in the measurement, a Superposed Epoch Analysis (SEA) of the peak top was done for different months. Each SEA was done over a period of approximately 10 days and samples over one day with a resolution of 30 minutes. Figure 4.6 shows the SEA for June, September and December.

The mean of the SEA (solid line) is associated with the centre of the peak. In June (December) where it is nearly continously dark (light) no periodic variation could be observed. The variation in standard derivation in June is most likly due to missing data near noon because that is the time the local oscillator frequency was turned to CO observations. It might also be reactions to sunlight as discussed below. September, and all other months,

with appreciable day/night periods, show a slight shift of the mean to higher channels, i.e. higher frequencies, during daytime. It is improbable that such changes are produced by tides because tides at this latitude are observed to be symmetric around 15 o'clock and not noon. In addition the calculated shift produced by tides is smaller then the resolution of ARON and should if observable also be visible around solistics (June, December)

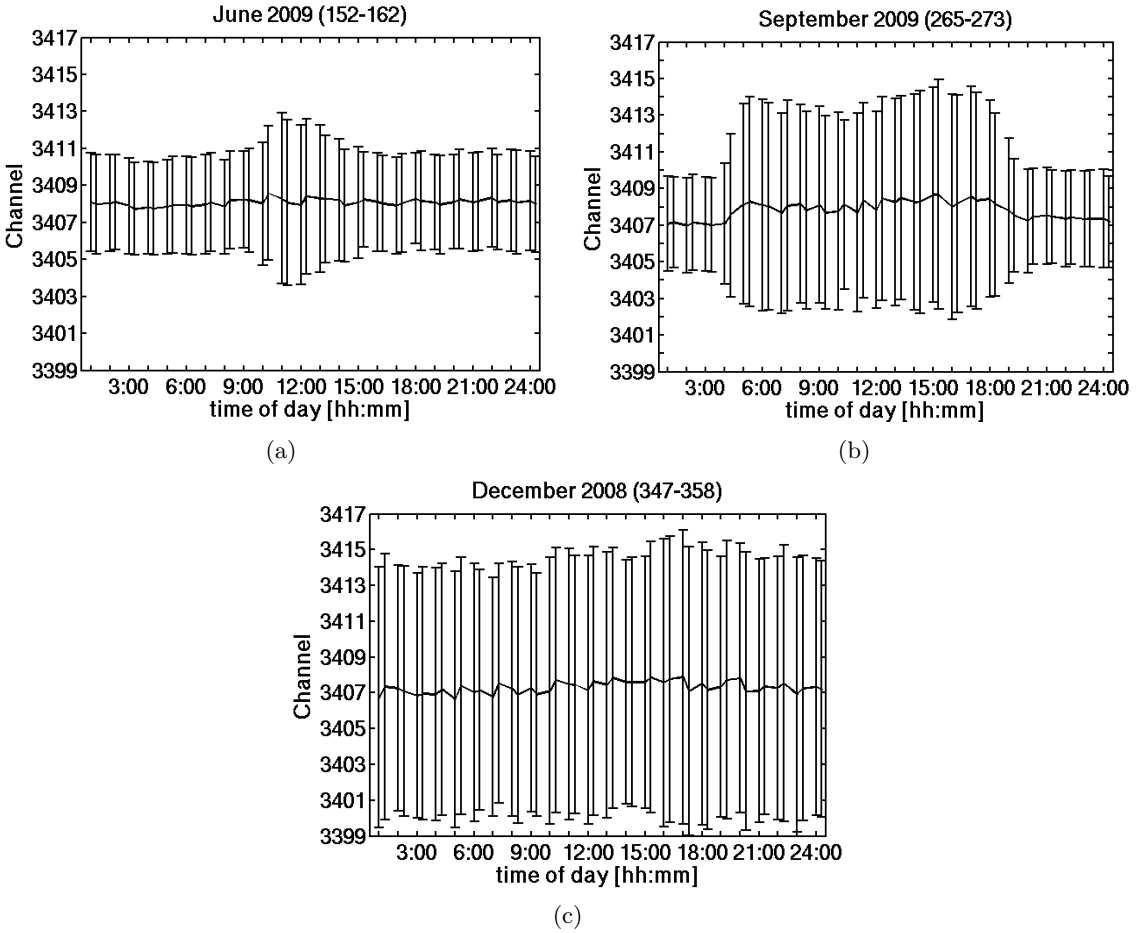

Figure 4.6: Superposed Epoch Analysis for (a) June (day 152-162), (b) September (day 265-273) and (c) December (day 347-358).

Furthermore there appears to be a very strong correlation between day/night conditons and both the peak shift and the magnitude of the standard deviation:

- standard diviation vs. night/day conditions

  The magnitude of the standard derivation is approximatly 5 channels during nighttime and approximatly 20 channels during daytime. This strong correlation between the standard deviation and day/night conditions suggests that the shape of the spec-

tral peak leads to the difference in standard deviation. During the day, when the high altitude ozone is depleted, the top part of the peak is flater then during the night. Therefore random shift of the highest peak value due to a low signal to noise ratio is possible over a wider frequency rangeduring daytime. This leads to stronger variation of the peak top value during the day and explaines the difference in standard deviation. However the shift of the line center, i.e. the mean, can not be shifted due to changes in the lineshape because the Doppler, Lorentz as well as the Voigt shape are all symmetric around the charateristic frequency.

- peak shift vs. night/day conditions

  Changes in Doppler shift due to different wind velocities at different altitudes could produce the shift of the peak top between night and day conditions. At nighttime mesospheric winds produce the Doppler shift. At daytime due to absence of mesospheric ozone means it would be the stratospheric winds that shift the peak. The calculated and the observed shift are in the same direction as winds become less eastward at higher altitudes. This should lead to a shift towards lower frequencies, i.e. channels, during night.

The shift of the peak position during the year and day/night shifts could be caused by Doppler effects but the magnitude of the effect is close to the resolution of ARON and the effects due to noise are much stronger. It is also possible that the shift is caused by the local environment of the instrument and have to be subject of future studies. For hourly averaged spectra the peak top varies about two channels around the mean over the period of one month. For the calculation of the profiles the ozone frequency was shifted to the average mean peak top frequency of the month in question. This has the same effect as shifting the frequency scale of the measured peak. There were also calculations done where the ozone frequency was shifted to the observed peak top value for each hourly averaged spectrum before the inversion, but the measurement response did not improve and the averaging kernel matrices looked alike. Therefore this error was assumed to be negligible. Furthermore is it possible that such a correction of the peak position could contaminate the position of the flanks of the peak. Due to the flat top shape of the peak the error due to a wrong peak top value should effect the inversion less then the error due to wrong positions of the steep flanks.

4.2 Measurement response

The measurement response (MR) shows at which altitudes the solution, i.e. altitude profile, represents the measurement and where only the a priori profile. That means it shows at which altitudes the a priori profil is changed to fit with the measurement. It can be interpreted in two ways:

- as the response at one altitude to constant change (1 ppm) at all altitudes
- as the sum over the responses at all altitudes to a change (1 ppm) at one altitude

Figure 4.7 shows the measurement response for ARON for a representative ozone measurement of the 249.9 GHz ozone line. Representative MR for all other months can be found in Appendix E.2.

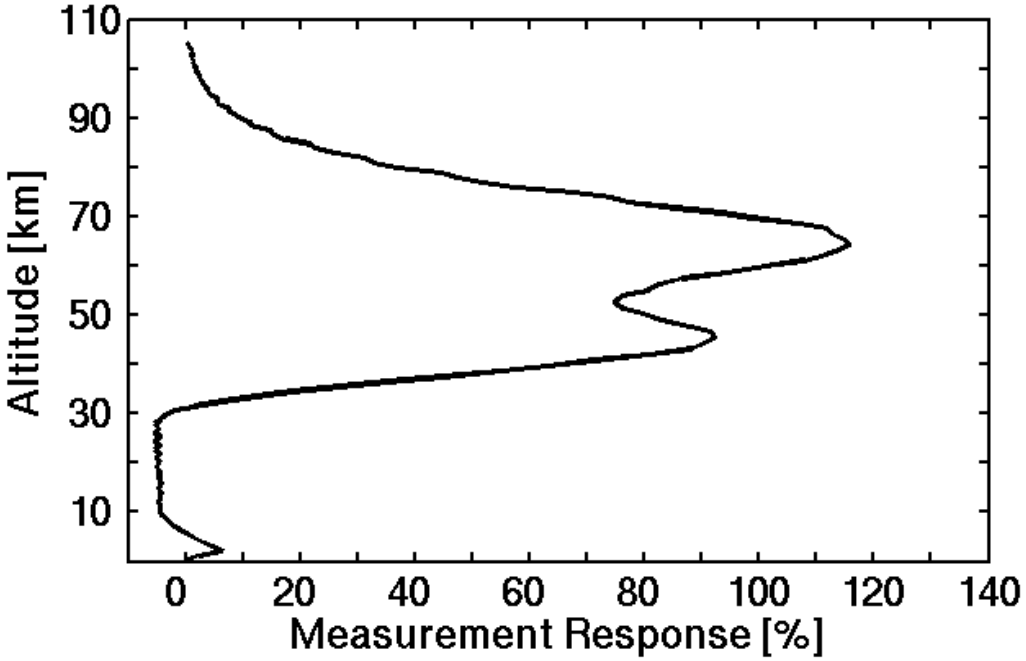

Figure 4.7: Sample measurement response of ARON, day 158 year 2009

Each inverted profile has a unique measurement response due to difference in signal to noise ratio, different a priori profiles and different model atmospheres, but there are strong similarities between them. In the height range between 35 and 75 km the response to the total change is more then 30%. That means that in this altitude range there is sufficient information in the spectrum so that the a priori profile will be adjusted. Information about how and where these changes in the real profile are observed in the inverted profile can be extracted from the average kernel matrix of the inversion (Section 2.4.2). Figure 4.8 presents the average kernel matrix for an inversion of the 249.96196 GHz ozone line measured by ARON in June. Typical averaging kernel matrices for all other months are given in Appendix E.3.

The linear sensitivity decrease due to the radiometer formula (Section 2.4.3) is clearly visible in the averaging kernel matrix above 40km. The rapid decrease of sensitivity below $\tilde{4}0$ km is due to the fact that the line shape becomes very broad due to pressure broadening. It is therefore no longer possible to distinguish between the spectral line and the

baseline/noise of the instrument. The spectral line at around 30 km looks very much like a sinosoidel baseline. The effect of Doppler broadening on the altitude resolution at around 70 km, which corresponds to the transition to Doppler broadening for ozone shown in Figure 2.11. The altitude, where the HWHMs of the Doppler and the pressure broadening cross, varies throughout the year due to changes in the pressure-height relation. In summer the same pressure level is located at higher altitudes than in winter. The cross-section is predicted at around 65 km in June and around 72 km in November and in between this range for all other month. The fraction of pressure to Doppler broadening is more then 25% at 75 km for all months. Therefore a sufficient altitude resolution should be found at this height during all seasons. The increasing effect of Doppler broadening might, however, lead to an anomalously strong response at altitudes around 70 km because changes in the real profile above 70 km create changes at 70 km in the calculated profile. This is observable in the averaging kernel matrix in Figure 4.8.

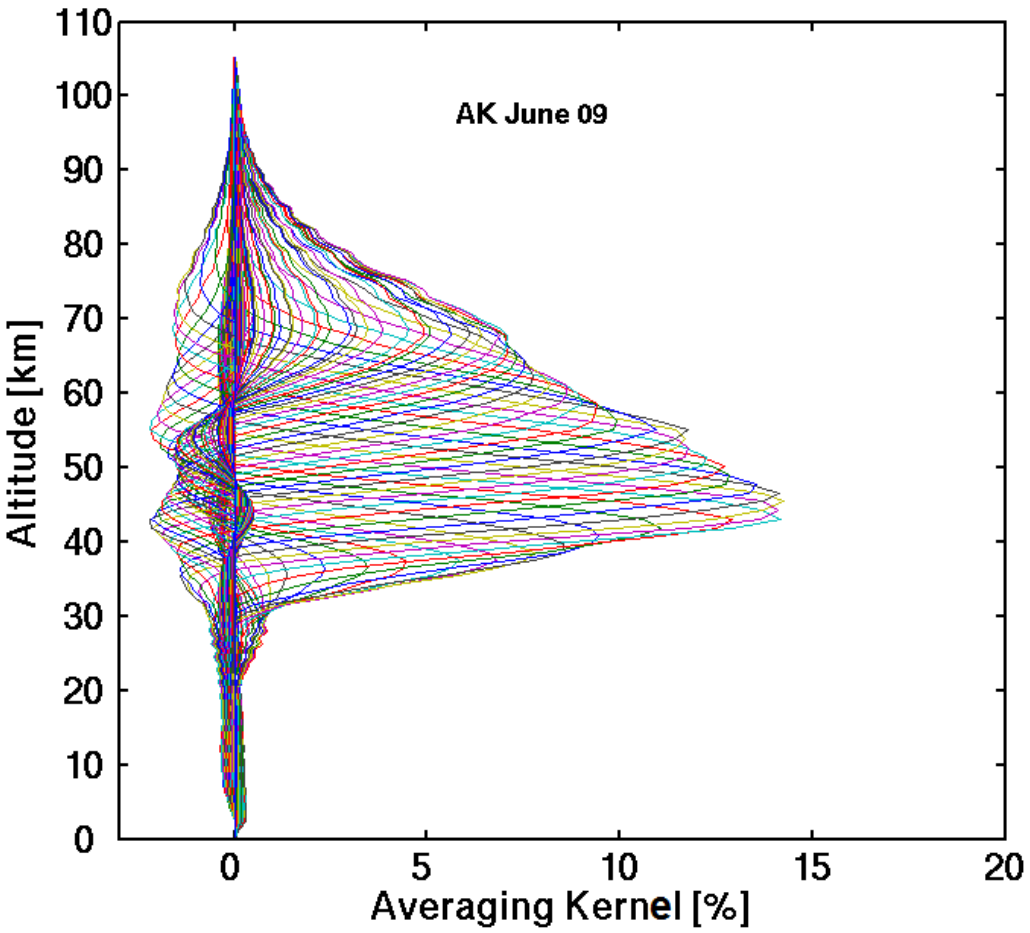

Figure 4.8: Averaging Kernel matrix of ARON for the 249.9 GHz ozone line, day 158 year 2009

The averaging kernel matrices of ARON show furthermore that features in the real profile will be distrubed, or smeared to adjacent altitudes in the calculated profile. The full width of half maximum of an averaging kernel is interpreted as the vertical resolution of its corresponding altitude. Figure 4.9 shows a typical vertical resolution of a profile calculated from ARON's broadband CTS ozone measurements. The vertical resolution is approximate 10 km in the stratosphere and reaches $\sim$ 17 km in mesospheric regions. The poorer altitude resolution at higher altitude could be improved by longer time averages of the spectra but this would lead to less temporal resolution. In addition, the transition of the lineshape to Doppler means that the spectrum does not carry as much altitude information, so it is unclear that significant improvements could be obtained.

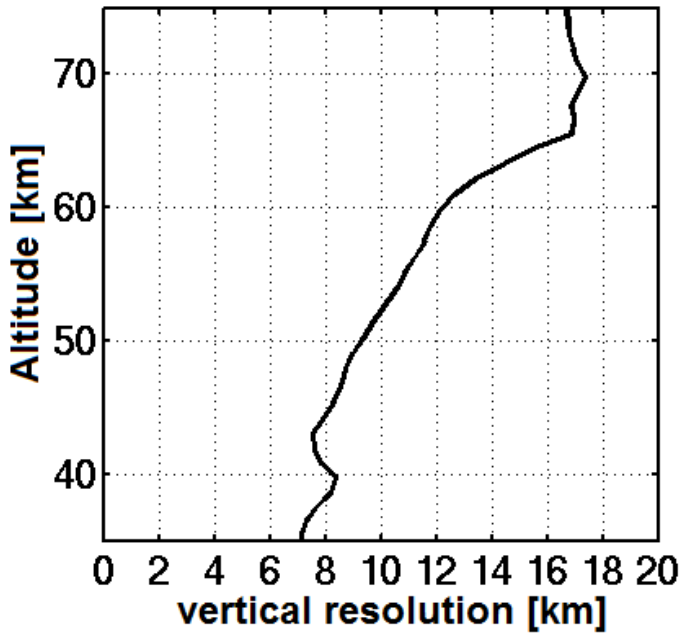

Figure 4.9: Vertical resolution of a sample inversion, June 2009

Measurement response and the averaging kernel matrix oscillated in the summer months for altitudes above ca. 70 km, as shown in Figure 4.10. This oscillation was interpreted as a feature created by a compination of incorrect a priori profiles and poor altitude information due to the increasing effect of Doppler broadening. The combination of these two leads to under- and overestimation of adjacent altitudes resulting in an oscillating measurement response. This oscillations are in the majority of cases small, and in addition the ozone concentration is nearly zero at these altitudes in summer so that it was in generel in the range of noise and could not be observed in the calculated profiles. In some cases the over and under estimation led to a sharp unphysical peak for a single height step. These profiles have been removed.

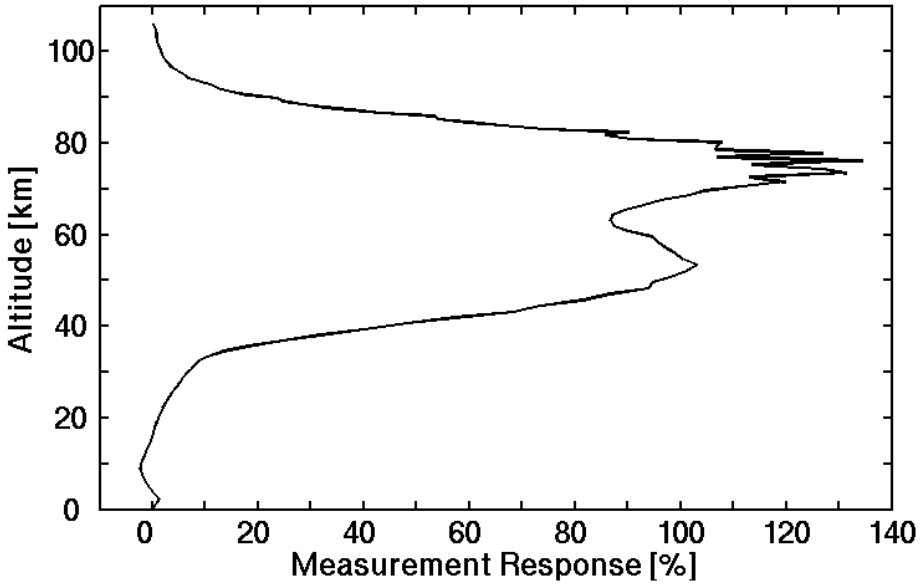

Figure 4.10: Measurement response for a inversion in Januar 2009, the responce is oscillation for heigh altitudes

In summary ARON is able to extract the real ozone profile in the altitude interval between 35 and 75 km with a vertical resolution of better than ¡17km

4.3 Data coverage

Ozone profiles have been calculated for the period of one year covering measurements from December 2008 until November 2009. However no spectra could be extracted from the 14.-18.Jan 2009 due to a poore signal to noise ratio in the measurements and in consequence of failure of the instrument no spectra were produced during two short periods in November and May (16. May 2009 2h -17. May 2009 13h and 24 Nov 2009 16h -25 Nov 2009 19h). In addition frequently absence of profiles due to the observation schedule occur approximately once a day during the lunch break at Troll station but the schedule is not always followed. The influence of such missing data sequences on spectral analysis will be discussed in Section 5.1.

4.4 Ozone profiles

The inversion of the profiles is based on a fixed pressure grid between 1 hPa and 0,01 Pa. The ozone profiles have afterwards be translated to an altitude grid (Figure D.2 in Appendix D) using a model atmosphere which leads to monthly changing offsets at the heigest altitudes. The used model atmosphere is given in montly means which leads to different offsets at the heigest altitudesto correct for seasonal changes for each month. The

pressure altitude correlation changes which gives an offset at the heighest altitudes. Figure 4.11 and 4.12 show the retrivaled profiles from December 2008 until November 2009 for all altitudes below 100 km as a contour and a 3D plot, respectivly. As mentioned before the area below 35 km is mostly a reflection of the a priori profiles used and monthly changes of the a priori are clearly visible in Figure 4.11.

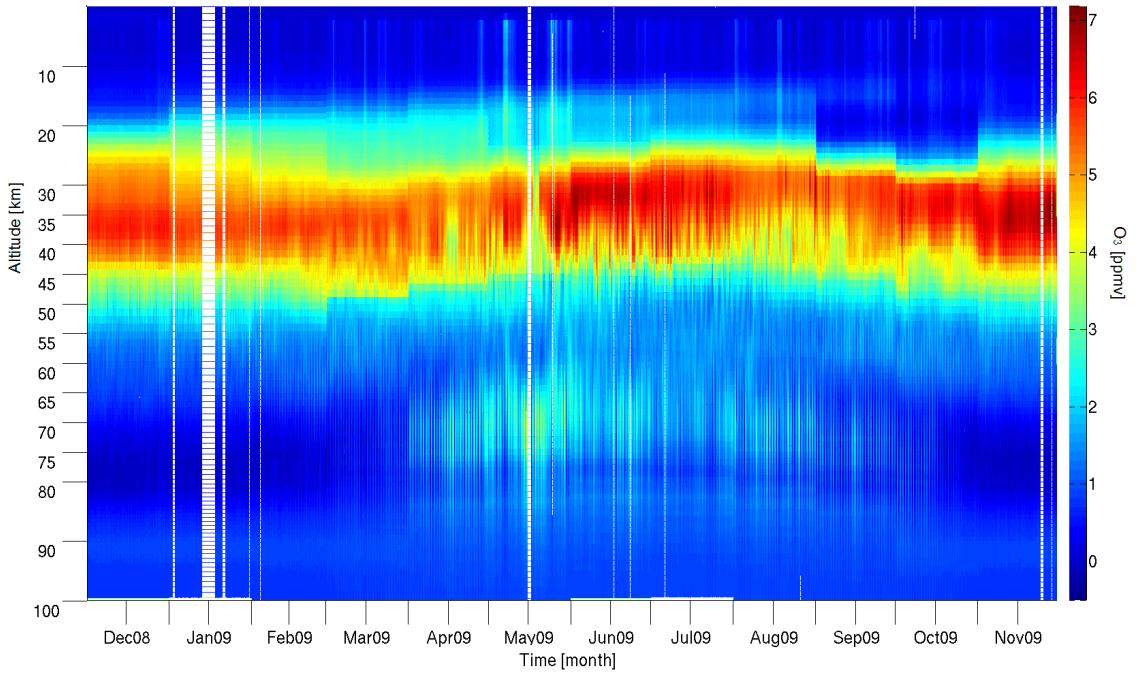

Figure 4.11: Inverted profiles below 100 km from December 2008 until November 2009

Above 75 km the inversion contains again mostly a priori information and all profiles are forced towards the a priori. It should be mentioned that the a priori profiles do not distinguish between day and night conditions and are just a summer/winter mean at altitudes above 45 km. Therefore, and because of the poor measurement response above 75 km, the development of the secondary maximum (Section 2.3.2) is not reflected by the inverted profiles. The first maximum (Section 2.3.2) is visible around 35 km. At its lower side the information is mostly provided by the a priori profile. The maximum magnitude varies between 5 and 7 ppmv throughout the year and has its highest values around June and November. Another maximum, which can be identified as the middle mesospheric maximum (Section 2.3.2), is clearly visible in the night profiles between April and September around 70 km. It maximizes in early (May) and late (August) winter, and the early winter maximum is greater the late winter one. Detailed exploration of the middle mesospheric maximum is beyond the scope of this thesis and will be subject of further work. The origin of the frequently observed high ozone values in the troposphere is assumed to be generated by incorrect tropospheric temperature profiles and is explained in Section 4.1.1.

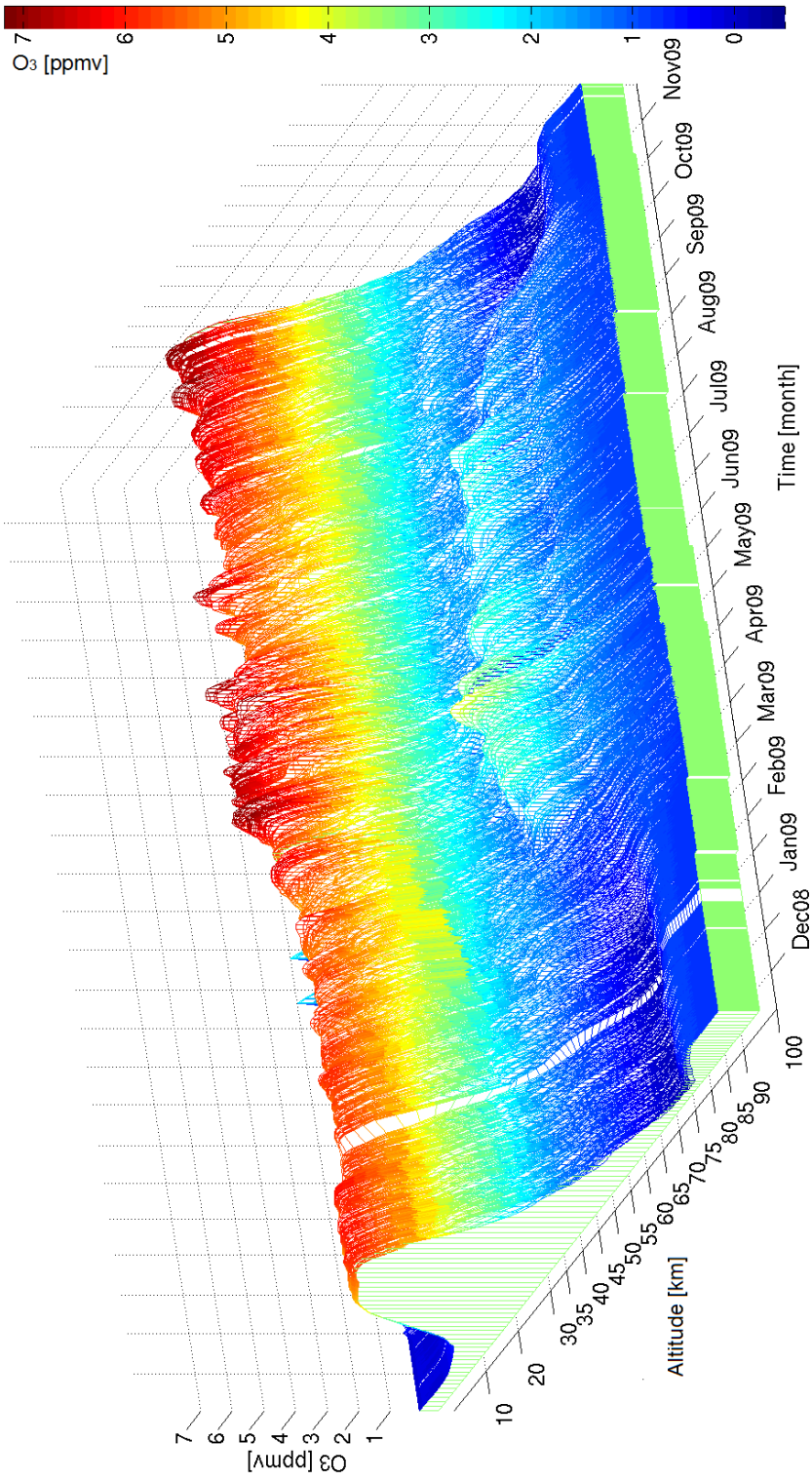

Figure 4.12: Inverted profiles below 100 km from December 2008 until November 2009

Temporal fluctuations of the ozone mixing ratio occur at altitudes of the first maximum and seem to strengthen during winter and spring. Similarly there is strong modulation of the middle mesospheric maximum at periods longer then one day, which might be caused by planetary waves. Spectral analysis has been done to extract wave periods present in the profiles as a function of altitude and season. These will be discusses in Section 5.1.

4.4.1 Comparison with COMMA-IAP

To ensure that the inverted profiles are reasonable compared to ozone distributions expected above Troll station, they have been compared with the COMMA-IAP model [*Sonnemann et al.*, 1998]. The model has been run for general solar minimum conditions and no attempt has been made to simulate the conditions present during the data period. Thus, these comparisons were used only as a guide to the reliability of the inverted profiles

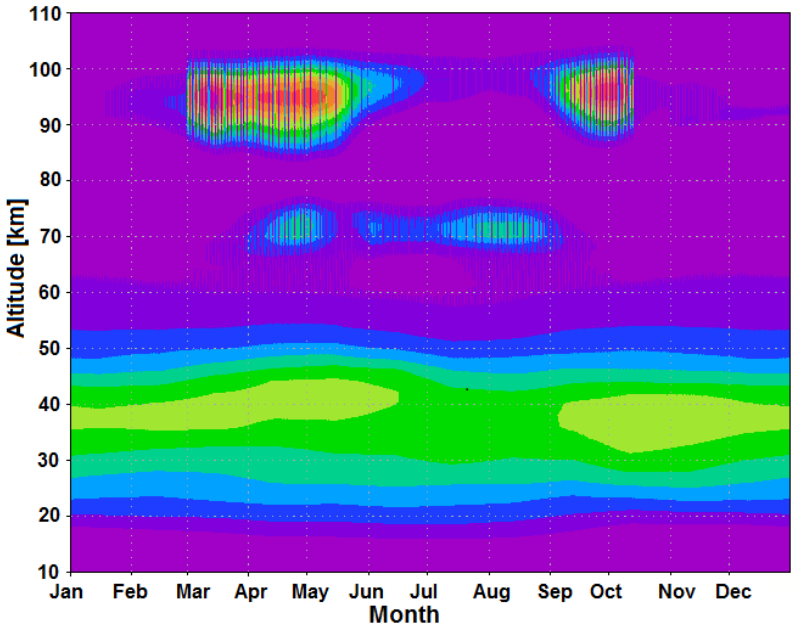

Figure 4.13: Ozone mixing ratio according to the COMMA-IAP model at 67.5°S, 10-110 km; ozone mixing ratios increas from 1 ppmv (violet) to 10 ppmv (red) with 0.5 ppmv scaling

The COMMA-IAP model is a three dimensional global model of dynamics and chemistry in the atmosphere (30-150km) combining a dynamic version of the Cologne model of the middle atmosphere (COMMA) and the Kühlungsborn three-dimensional photochemical model created by the Leibniz-Institut für Atmospherenphysik (IAP). The COMMA model covers dynamics from the boundary layer to the thermosphere (0-150km). The photochemical model covers advective and diffusive transport, chemical reactions and radiation

(ionization and photodissociation). The horizontal resolution is 5.625° in longitudinal and 5° in latitudinal direction. Figure 4.14 shows modelled ozone distributions for solar minimum conditions near Troll in the altitude range of 10-85 km. The ozone mixing ratio is presented in intervals of 0.5 ppmv and the altitude resolution is 1,1 km.

Similar seasonal variations in altitude of the first ozone maximum and a decrease around August are visible in both the inverted profiles and the model. In addition the occurrence of the middle atmospheric maximum and its maxima in early and late winter fit with the development of the inverted profiles. Furthermore the modelled magnitudes of the ozone mixing ratio are comparable with the magnitudes in the inverted profiles at all altitudes and seasons.

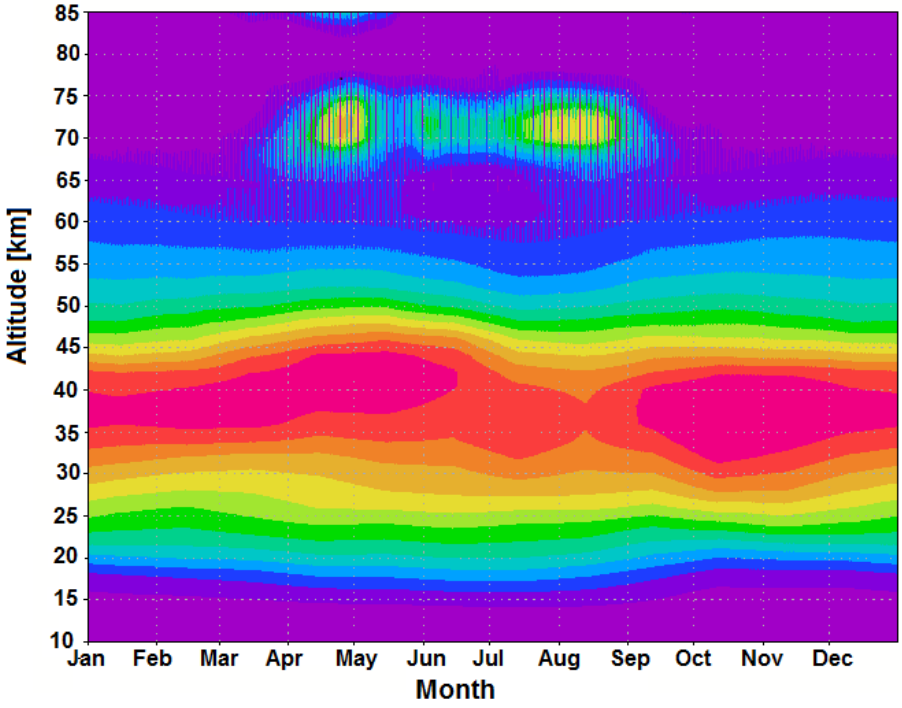

Figure 4.14: Ozone mixing ratio according to the COMMA-IAP model at 67.5°S, 10-85km; ozone mixing ratios increas from 0.5 ppmv (violet) to 6.5 ppmv (red) with 0.5 ppmv scaling

The model also shows the development of the secondary maximum during the year presented in Figure 4.13. However this can not be covered by the inverted spectra due to the insensitivity of the measurement at high altitudes discussed earlier.

As mentioned, the model was not run for spesific conditions during the data periode, and serves only as a guide. In the main the inverted profiles and the model provide similar results. For a more detailed compairison, the model must be run for the exact dynamic and solar conditions occuring the data period. However the consistency with the model

strengthens the reliability of the inverted profiles and justifies the effort to use them to trace planetary wave activities.

Chapter 5

Discussion

Although the ozone profiles in Section 4.1 are plotted for the altitude range below 85 km one has to keep in mind that only altitudes between 35 and 75 km can be used to trace wave activity. The rest of the profile is, as discussed in Section 4.2 contains mostly a priori controlled information, and changes in this regions are mainly created by noise.

5.1 Spectral analysis

For the retrieval of wave activitiy from the inverted ozone mixing ratio profiles, different spectral analysis were done.

5.1.1 Lomb-Scargel

The inverted profiles are averages over one hour but not totally evenly spaced in time. The observation schedule, which requires observation of CO with the broadband CTS for two hours each day, instrumental failure and defective measurements result in unevenly spaced spectra. Therefore the Fourier technique of Lomb-Scargle [*Press and Teukolsky*, 1988], which, in short, is a Fourier transformation for unevenly spaced data, is used for the spectral analysis of the data. The matlab implementation of this algorithm was taken from *Shoelson* [2003] and monthly sets of profiles were analyzed for each altitude step. Figures 5.1 shows the Lomb-Scargle for June and December.

Significant wave periods are found around 3 and 7 days in the upper stratosphere in winter. These periods fit with the expected periods of short period planetary waves. In addition the absence of wave periods in summer can be explained by interaction of planetary waves with local wind conditions. Therefore these periods were interpreted as an indicator for short period planetary waves.

Periods of more then 15 days are visible the whole year. Such periods are assumed to be caused by the limited size (30 days) of the dataset although their periods do fit with observed periods of planetary waves.

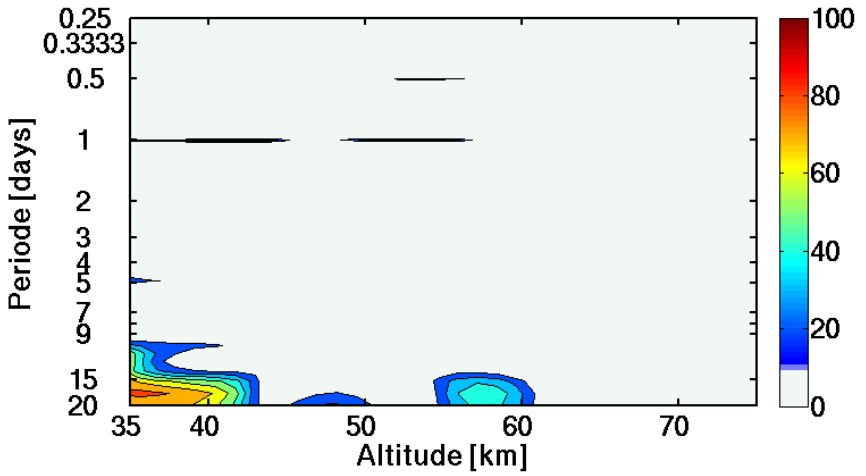

(a) December 2008

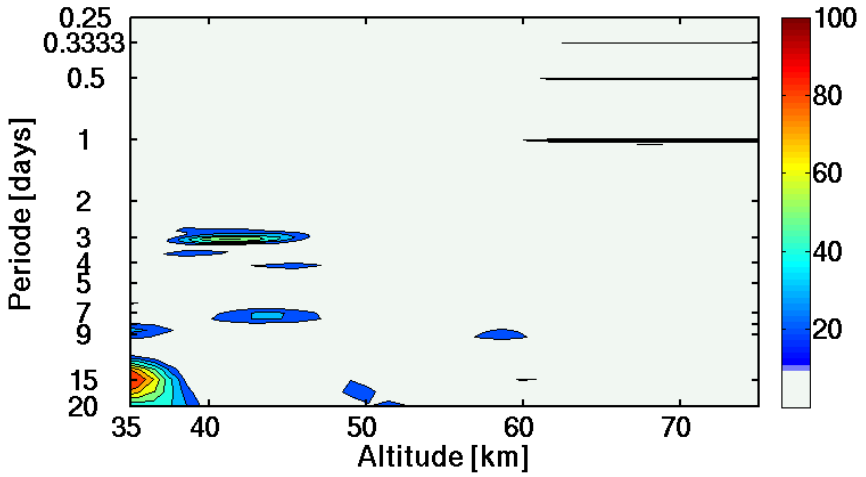

(b) June 2009

Figure 5.1: Lomb-Scargle of the inverted profiles for (a) December 2008 and (b) June 2009

Periods of 24h, 12h can be observed in the winter mesosphere and the summer stratosphere. They reflect the photolysis of ozone and/or diurnal (24h) and semi-diurnal (12h) tides. Solar tides in the atmosphere have a period of one day (diurnal) and higher harmonics and are created by the non-sinusoidal thermal heating of the diurnal variations of solar radiation. They arise in the troposphere and lower stratosphere and propagate vertically through the mesosphere up into the thermosphere and thus connect the different vertical layers of the atmosphere. In the troposphere they arise due to convection, condensation

and solar heating of water vapour. In the stratosphere solar heating of ozone is of capital importance [*IAP*, 2002/2003]. Tides are forced, not evanescent solutions to the vertical structure equation and propagate energy. Energy conservation and an exponential decrease of air density results in growth of wave amplitudes with altitude. The assumption of tides is strengthened by the occurrence of a ter-diurnal (8 h) period in winter that indicates an interaction between the diurnal and subdiurnal tide [*Younger et al.*, 2002].

The fact that no planetary wave activity is visible at higher altitudes does not mean that there is none. The absence might be caused by the decrease in the magnitude of the ozone mixing ratio. The easy model used in Section 2.3.3 to connect variations in temperature and ozone mixing ratio predicts a nearly constant percentage amplitude with altitude. This leads to stronger amplitudes where the magnitude of the mean ozone mixing ratio is highest. The amplitude of planetary wave activity assosiated with normal modes is assumend to stay realtivly constant below 90 km. This fact in addition to the growth of tidal-wave amplitudes and lower amounts of ozone mixing ratio with altitude results in insignificant amplitudes at higher altitude compared to lower altitudes. The fact that no, not even tidal, wave activity is visible in the summer mesosphere was related to the absence of ozone (the tracer) at these altitudes in summer.

There are some sporadic signs of wave periods around 7 days during some summer months. The Lomb-Scargle of January is presented as an example in Figure E.4. If they occur due to real wave activity or likely due to oversampling effects of the Lomb-Scargle is hard to tell. Furthermore the Lomb-Scargle algorithm gives only a stationary interpretation of the data. Though changes in wave activities during the year are evident by the comparison of different months, the Lomb-Scargle analysis does not tell if a wave changes amplitude, and therefore significance during a month. The Lomb-Scargle analysis was therefore only used as an indictor for planetary waves. However the results of the Lomb-Scargle analysis are a strong indicator that it is possible to observe wave activity in the Antarctica with ARON by analysing variations of the inverted ozone profiles.

5.1.2 Wavelet transform

To get more information about the dynamics of the observed planetary wave activity a Morlet wavelet transform [*Torrence and Compo*, 1998] was done for the whole dataset (December 2008- November 2009). Actually a wavelet transform requires evenly spaced data. However datagaps causedby the observation schedule are insignificant for the retrieval of planetary-wave activity because the periods of the waves are much longer than the variations in time spacing. In order to examine the fluctuations of the ozone mixing ratio from seasonal variations, monthly average profiles were subtracted from the data.

The wavelet transform is done for specific pressure levels because the inversion of the profiles is based on a constant pressure grid. The given altitudes are associated with a priori profile of February. Figure 5.2 show the ozone variation, the wavelet and the integrated variance for periods between 1.7-4-days, 4-8-days, 8-16-days and 25-50-days at 46km.

5.2 Planetary waves

The variations in the ozone mixing ratio are not constant in altitude or period throughout the season. This is clear from Figure 5.2(a). Fluctuations strengthen in wintertime, indicating stronger wave activity. This can also be observed from the wavelet.

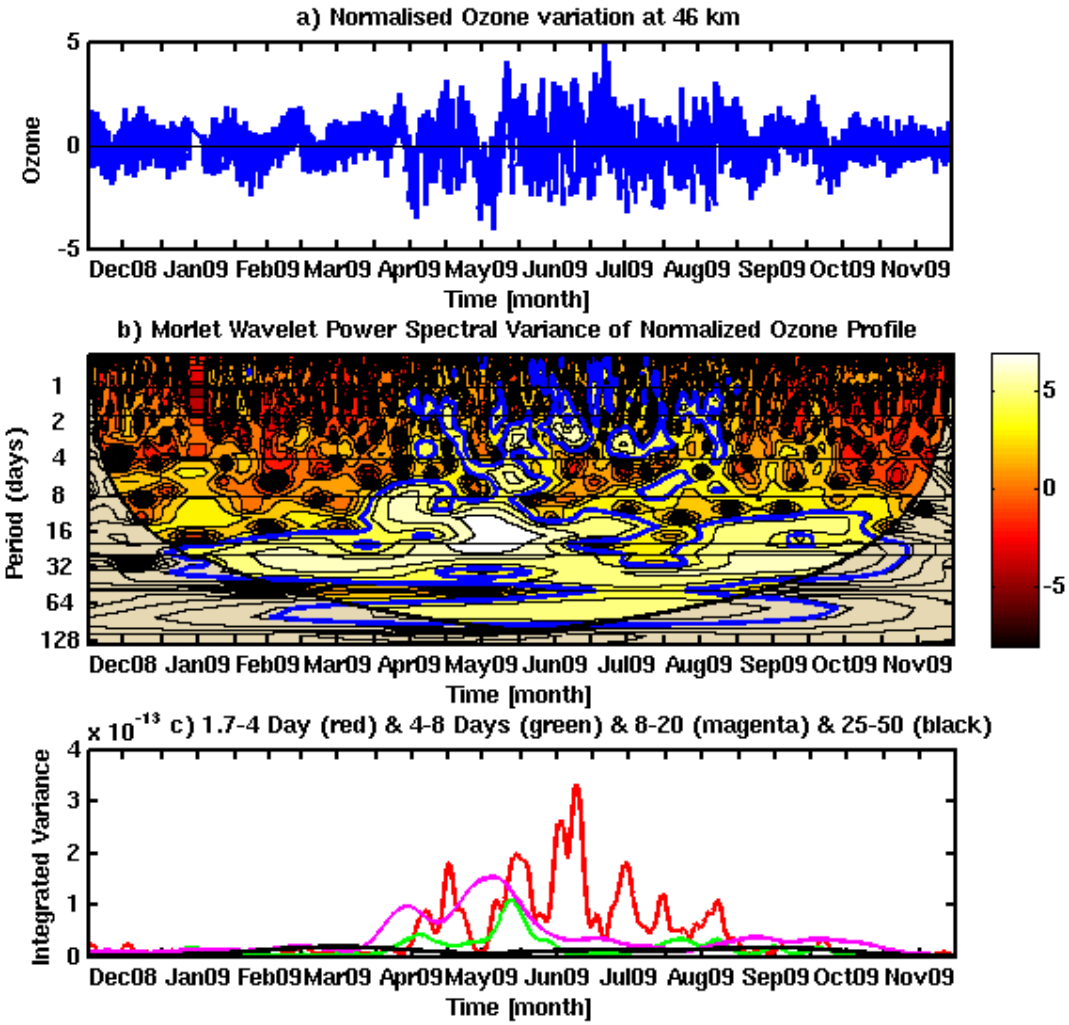

Figure 5.2: (a) Ozone variations at approximately 46 km over Troll from December 2008 until November 2009. (b) Morlet wavelet transform power spectrum from (a). The blue line renders areas of more then 95% significance. The areas below the cone-shaped solid line lines are subject to end effects. (c) The wavelet variance integrated over the 1.7-4-day (red), 4-8-day (green), 8-20 (magenta) and 25-50-day (black) periodic bands.

Short period waves are significant from April until September, middle period waves from end of March until end of October and long periodic waves are significant during the whole

period, except during the summer. The absence of planetary waves in summer can be observed from wavelet transforms at all reliable pressure levels (35-75km). This lack of wave activity in the summer upper stratospheric lower mesospheric region above Troll can be connected to the local wind motion.

Zonal wind measurements and calculations above Rothera [*Hibbins et al.*, 2005] station (67°S,68°W) are illustrated in Figure 5.3.

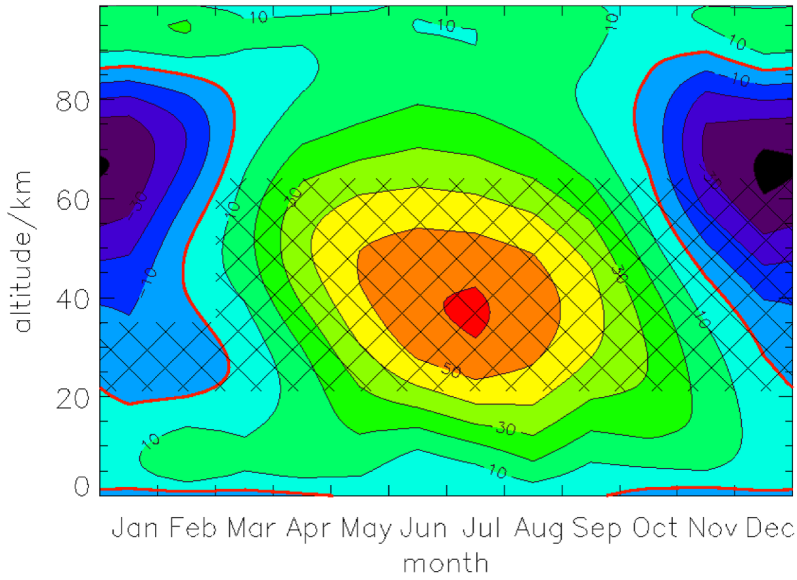

Figure 5.3: Mean zonal wind above Rothera from 0-100km. Generated from a 6th order polynomial fits to the monthly mean data and, within the hatched area, monthly mean HWM-93 model winds. The thick red line represents the 0 m/s contour, other contours are drawn at 10 m/s intervals (blue: westward). From *Hibbins et al.* [2005]

During summer (November - March) a mean westward wind absorbs planetary wave activity coming up from below (See Section 2.2.3).. By contrast, a mean eastward wind is predicted in winter. The eastward cut-off wind for the first normal modes (Table 2.2, Section 2.2.3) was calculated to be stronger than 100 m/s (Eq. 2.16). The maximum magnitude of the present eastward wind is much less and therefore not strong enough to reflect the waves. Therefore westward propagating planetary waves from sources in the troposphere are neither absorbed nor reflected. Hence they can propagate through the stratospheric and mesospheric region into the thermosphere. The observed modes should therefore also be observable in the upper mesospheric lower thermospheric (MLT) wave activity that also corresponds to sources in the lower atmosphere.

A component of the 1.7-4 period band is the quasi-two-day-wave (QTDW) which is associated with the asymmetric mixed planetary-gravity mode (3,-3). Its period remains in the range of 2.1-2.5 days. In addition, amplitudes of 3-day and 4-day oscillations with

zonal wave number one have been observed and it has been suggested that the waves are quasi-non-dispersive and circle the pole at a similar velocity. It is stated that this leads to strong temperature maxima that have been named warm pools [*Prata*, 1983]. They have been observed during the polar winter in the Southern Hemisphere with a period of 4 days. A variance with periods near two days is also documented. [*Prata*, 1983]

The strong amplitudes of the 1.7-4 day band from mid-April until September are assumed to be created by a trigger perturbation that transfers energy from the mean wind flow into the QTDW. Such a process requires regions of barotropic and baroclinic instabilities. These instabilities are respectively associated with strong horizontal and vertical shears in the zonal wind and related to the polar night jet [*Baumgaertner et al.*, 2008]. *Baumgaertner et al.* [2008] and references with in note that barotropic instabilities have the ability to create short-periodic waves and that a baroclinic atmosphere has the feasibility to develop instabilities and release potential energy. Figure 5.4, taken from *Baumgaertner et al.* [2008] illustrates the vertical average wind shear between 60° and 70°S and the horizontal average wind shear at 70° during 2005.

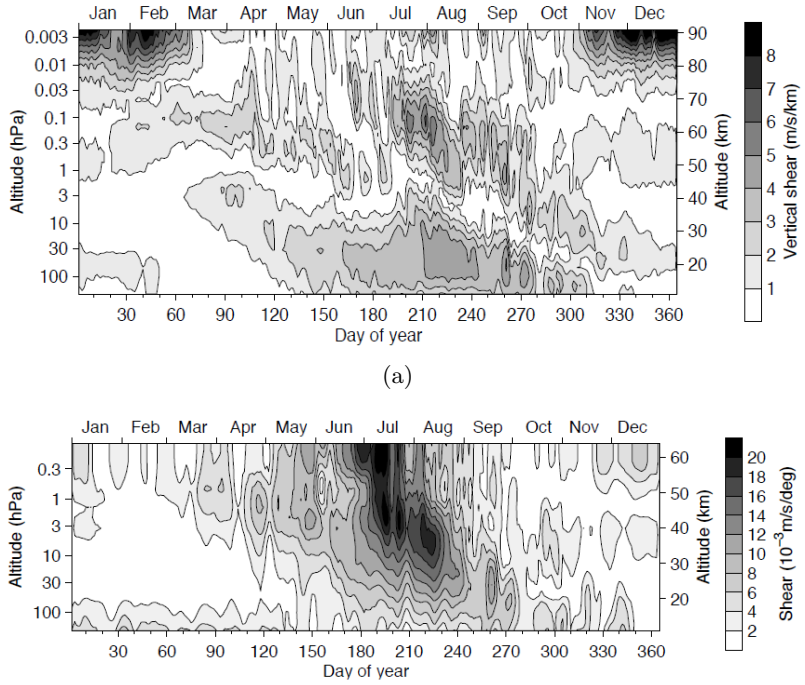

Figure 5.4: (a) Averaged vertical wind shear between 60° and 70° during 2005, derived from MLS temperature measurements. From *Baumgaertner et al.* [2008], (b) Averaged horizontal wind shear at 70° during 2005, derived from UKMO zonal wind data. From *Baumgaertner et al.* [2008]

The vertical wind shear is in good agreement with the mean zonal winds above Rothera presented earlier (Figure 5.3). The vertical shear minimizes around 40 km altitude where the mean zonal winds maximize. On the other hand the horizontal shear is biggest where the wind at each altitudes is strongest eastward. Examinations [*Baumgaertner et al.*, 2008] indicate that at 70°S the horizontal shear contributes more to wave activity than the vertical shear because it is larger at this latitude. The vertical, and even more the horizontal shear below the upper mesosphere is much larger in winter than in summer and maximises around solstices. This development is consistent with the increasing amplitude of the 1.7-4 day period band observed by ARON during wintertime. An increase in quasi two day wave activity due to instabilities is also expected in the upper summer mesosphere because of strong wind shear, evident in Figure 5.4(a). Such wave activity is, for example, documented in *Salby and Callaghan* [2001]. That this effect is not observed by ARON is most likely caused by low mesospheric ozone densities during the summer.

The amplitude of the integrated wave activity of the 1.7-4 day period band seems to oscillate strongly. To explor this oscillation a Lomb-Scargle analyse was performed on the integrated variance of this periodic band from March until October. The result is shown in Figure 5.5. It should be noted that the total collapse of the observed wave activity in the 1.7-4-day periodic band in the middle of May might be caused by an approximately 36 hour gap in the data coverage due to instrumental failure (Section 4.3).

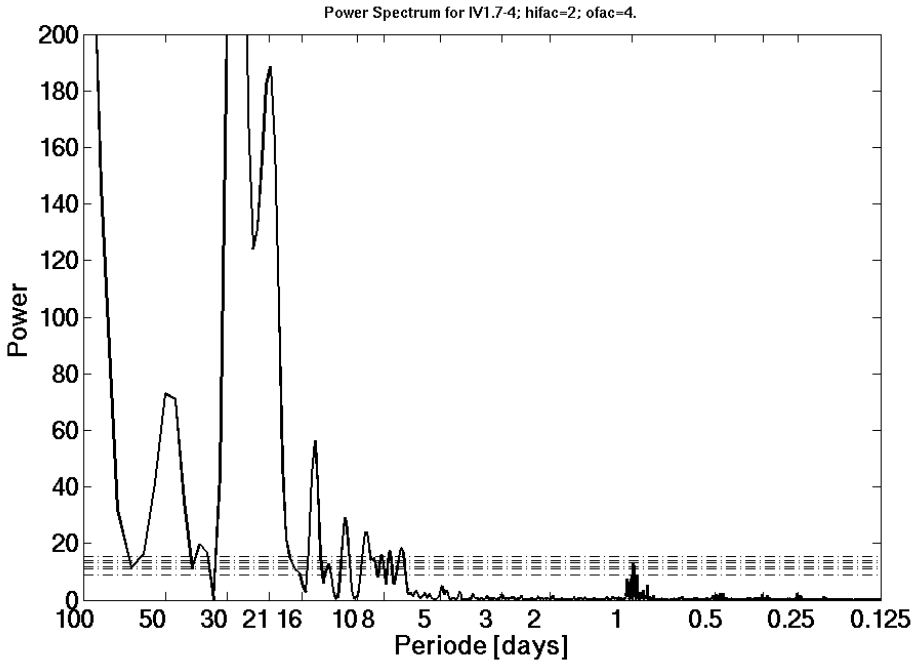

Figure 5.5: Power Spectrum from Lomb-Scargle of the 1.7-4-day periodic band from Figure 5.2 (c). The dashed lines represent the 0.5, 0.1, 0.05, 0.01, 0.005 and 0.001 probability amplitudes.

In addition to periods around 30 and 50 days, periods between 7 to 16, around 22 days and tidal periods are obvious. Periods above 100 days were assumed to be effects to the limited size ($\approx$ 200 days) of the analysed dataset. The 50-day period is presumed to be a subharmonic of the sinus like envelope of the analysed amplitudes.

The fact that diurnal and subdiurnal oscillations also appear in the Lomb-Scargle of the short planetary wave activity might indicate an interaction between tides and short planetary waves. In *Palo et al.* [2007] suggests that interaction between the diurnal tide and the westward propagating QTDW result in an eastward propagating two-day wave.

Interaction effects between short and longer planetary waves might cause the other identifiable periods. Shorter planetary waves see longer periodic planetary waves as a background wind slowly changing in time. The amplitude of westward propagating planetary wave is proportional to the background because its amplitude becomes higher for stronger headwinds. When the longer periodic waves maximises, the total background wind becomes less eastward and results in weaker short wave activity. It should be mentioned that the observed oscillation periods around 30 days might not be caused by interaction between planetary waves, but rather by the subtraction of monthly averages.

The (1,-3) 10-day and (1,-4) 16-day normal modes are covered by the 8-20 day periodic band. The model by *Salby* [1981] in a realistic atmosphere suggest periods of 8.3-10.6 days for the 10 day wave and a period range of 11.1-20.0 days for the 16 day wave. Extensive studies of the 16-day wave have been done using optical techniques and radar [*Luo et al.*, 2002] and two (or more) wave sources have been suggested [*Murphy et al.*, 2007]. As expected from theory, wave activity from the 8-20 day periodic band arises in the middle of March when the local zonal mean wind below 46 km become eastward in respect to the wave, and disappears in November when the local mean wind turns back into an westward direction. Wave amplitudes maximise around mid-April and mid-May, fall off and recover several times with much smaller amplitudes until mid-November. At higher altitudes the 8-20-day periodic band is only observable until September. This could be due to the fact that the mean zonal winds turn westward earlier in the year at higher altitudes (Figure 5.3). Althrough the absence of observed wave activity might be related to low ozone values. Another interessting feature of this band is that it shows a late winter (July-August) maximum at high (Figure 5.7) but not at low altitudes (Figure 5.2).

The observed wave activity of the 4-8 day periodic band maximizes in April and May shortly after the maxima of the 8-20 day periodic band, and also in August while the wave activity in the 8-20 day band has a minimum. This wave band contains the first symmetric normal mode (1,-2) solution denoted as the 5-day wave. Its period for a realistic atmosphere is modelled to be in the range of 4.4- 5.7 days [*Salby*, 1981]. Compared to the 10 and 16 day wave the latitudinal structure of the 5 day wave maximizes more equatorwards at middle latitude as illustrated in Figure 2.2. This might explain the weak wave activity of the 5-day wave in comparison to the 10 and 16-day waves.

The variation in wave activity in the 4-8-day and 8-20-day period band with respect to time is not explainable by the background winds. The decrease of wave activity of these periodic bands might be connected to the increasing amplitude of the QTDW. The QTDW wave extracts maybe not only energy from the mean flow, but also from the longer

period planetary waves. This would also explain the return of longer wave activity in September when fewer instabilities are reported and less wave activity of the 1.7-4 day band is observed. In addition a form of mode coupling seems to exist between the 5-day wave (4-8-day band) and the 10 and 16-day waves (8-20 day band). They are never observed to maximize at the same time, which may indicate some kind of exchange between them.

Longer period planetary waves covered by the 25-50-day band have been observed in the mesospheric and lower thermospheric regions by *Espy et al.* [2005] and *Luo et al.* [2001]. Such wave periods are also significant in the present observation. Excluding the border areas of the wavelet transform, the 25-50-day band is continously siginficant at upper stratospheric altitudes but at considerably smaller wave amplitudes. Towards higher altitudes such their amplitudes become more and more comparable to thoseof the other extracted periodic bands, maximizing in early winter simultaniously with the 8-20 day band. It is possible that such wave activity is a strong Doppler shifted version of the (1,-4) quasi-16-day mode which was assumed to be covered by the 8-20-day band. Such wave activity may not be able to exist at stratospheric heights due to the strong stratospheric eastward jets. It should be mentioned that the subtraction of a monthly mean done to extract wave fluctuations from seasonal variations might compromize the retrieval of wave periods longer then $\approx$ 30 days.

To assess if the observed wave activity of the different extracted bands propagates from below through the region of observation into the MLT, the integrated variance for the periodic 1.7-4, 4-8, and 8-20 day band is displayed for altitudes between 35 and 75 km in Figure 5.6 below, and Figures E.5, E.6 in Appendix E.4.2, respectively. Note the change in the scaling with altitude.

The amplitudes of the wave induced variations in the ozone mixing ratio are derived from the ozone anomaly (difference from monthly means). However, these amplitudes will be dependent upon the magnitude of the average ozone mixing ratio (Section 2.3.3). For example, the mesospheric ozone mixing ratio becomes zero in summer and therefore no wave information can be extracted from this area. In contrast night ozone mixing ratios during the occurence of the middle mesospheric maximum are large enough to observe wave activity. Seasonal variation of the upper stratospheric ozone mixing ratio are small and the observed seasonal change in wave activity is assumed to be real and only insignificant related to seasonal changes in ozone mixing ratio. Due to the mentioned dependence of the amplitudes upon the magnitude of the average ozone mixing ratio and smaller ozone mixing ratios at altitudes above the first maximum, the integrated variance is much smaller at higher altitudes. Therefore the scaling was ajusted to make wave activity visble at these altitudes.

It is obvious that wave activity of all considered periodic bands in question extends to higher altitudes and becomes observable around the middle atmospheric maximum. This strengthens the assumption that planetary wave activity created in (QTDW) and below the stratosphere and mesosphere mainly is caused by normal modes. For better identification of the observed modes, information about the wave number, phase and propagation direction

is needed. This can not be extracted from the present observation because horizontal properties can not be recovered from ARON measurements alone.

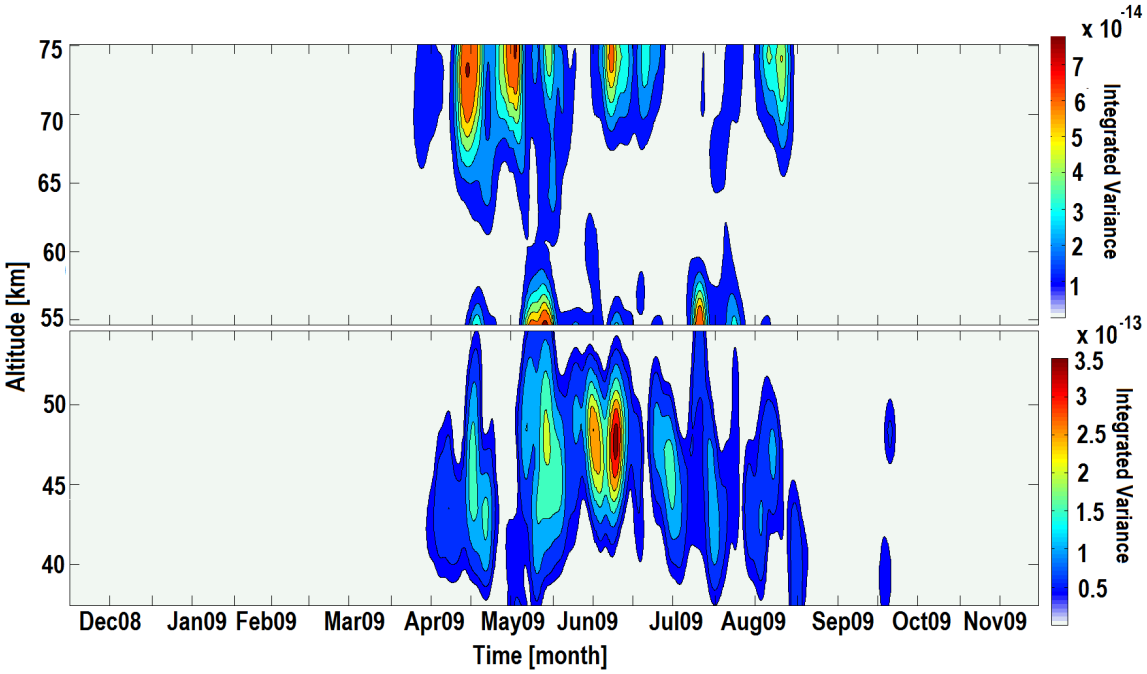

Figure 5.6: Integrated variance of the 1.7-4-day periodic band from the Morlet wavelet transform of ozone variation from December 2008 until November 2009 over altitude and time

5.3 Tides

In agreement with the Lomb-Scargle analysis of the profiles the wavelet transform shows significant periods of one day and less at higher altitudes during the occurrence of the middle atmospheric maximum. This is presented in Figure 5.7.

Periods of one day might just reflect the photolysis of ozone during daytime but they might also reflect tidal wave activity. A differentiation between diurnal and semi-diurnal tides is not possible due to the uneven spectral spacing of the analysed data. A possiblity to examine tides from the wavelet would be to extract time series of even spaced data or through extrapolartion of missing data. In addition, profiles could be studied for signs of downward phase progression in time. The retrieval of tidal motion is beyond the borders of this thesis. In [*Christensen*, 2009] ozone profiles were inverted from ARON's ozone measurements for some days in February and April 2008 and a vertical wavelength and downward phase progression compatable with a 12 h tides was observed.

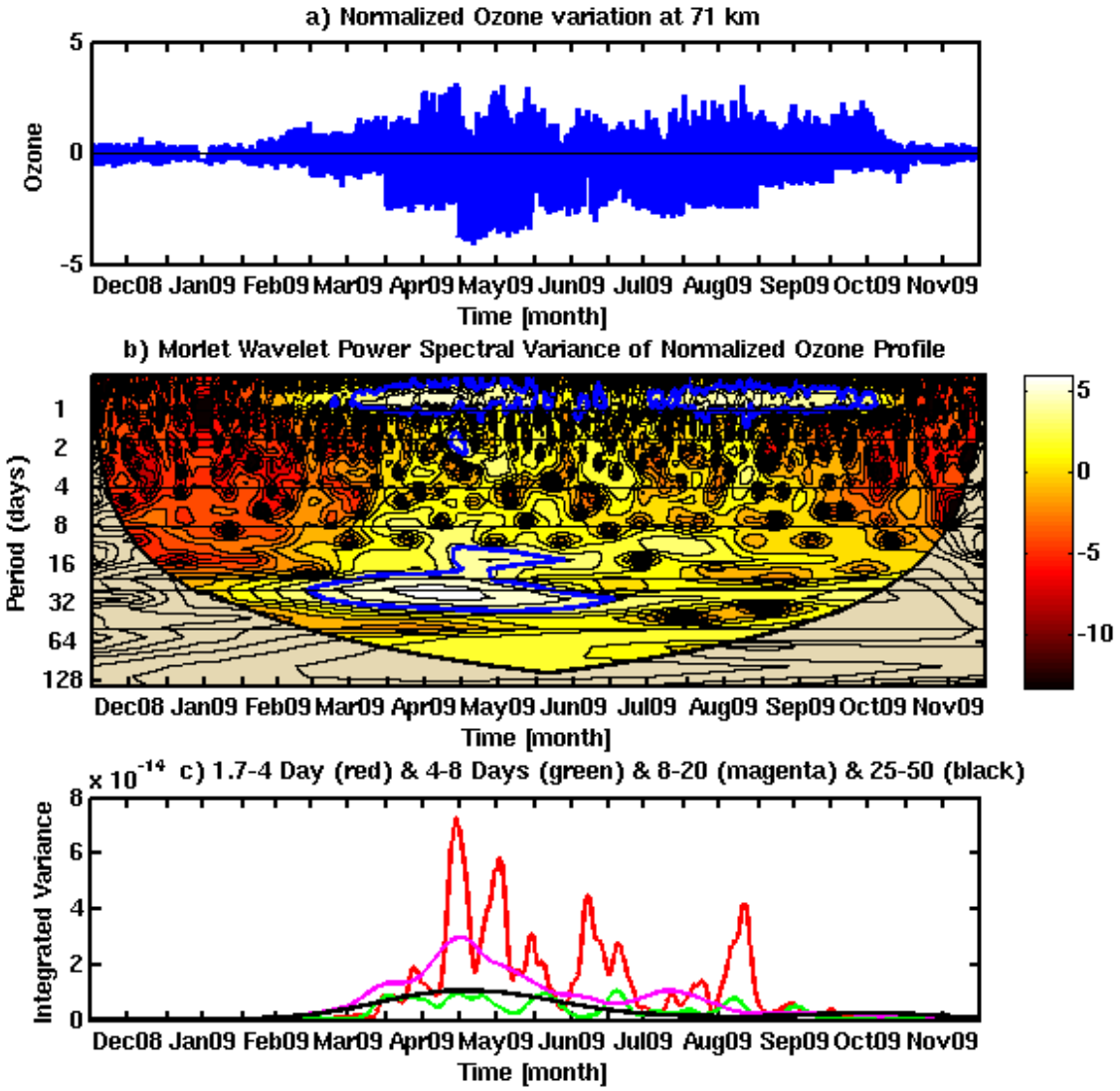

Figure 5.7: (a) Ozone variations at approximately 71 km over Troll from December 2008 until November 2009. (b) Morlet wavelet transform power spectrum from (a). The blue line renders areas of more then 95% significance. The areas below the cone-shaped solid line lines are subject to end effects. (c)The wavelet variance integrated over the 1.7-4-day (red), 4-8-day (green), 8-20 (magenta) and 25-50-day (black) periodic bands.

5.4 Comparison with Sanae wind measurements

In order to resolve the question if the observed planetary wave activities are characteristics of the real atmosphere, or whether it is an artifact of the inversion the results have been compared with wave activity calculated from meteor wind measurements at Sanea. A SuperDarn radar [*Greenwald and et al.*, 1995] is located at Sanae ($71°S, 2.5°W$). It measures wind velocities over the field of view of ARON by receiving echoes from meteor tails [*Hall et al.*, 1997]. These trails occur due to ionization as meteors ablate in the upper mesosphere and lower thermosphere. The evolution of these trails provides an estimation of the neutral wind at these altitudes. The radar has no altitude discrimination but the mean altitude has been estimated to ≈ 94 km with an altitude interval of 15 km. In addition, *Hibbins and Jarvis* [2008] shows that SuperDarn wind data at Hally correlate best with the height bin between 90 and 95 km of a near co-located imaging Doppler interferometer (IDI). The perpendicular winds are derived from difference in the radial velocity across the radar beams. The radar at Sanae covers a 45 km N-S range and averages over 200 km E-W. Its centroid is at $73.9°S, 3.4°W$ close to the viewing point of ARON.

To compare wave activity observed in winds at mesospheric- lower thermospheric (MLT) altitudes above Troll to wave activity observed in ozone mixing ratio variations in the upper stratosphere - mesospheric region, a Morlet wavelet transform of the meridional wind data from Sanae was done. As mentioned before variations in ozone mixing ratio were assumed to be related to temperature variations resulting from wave activity. Furthermore a good correlation between variations in mesospheric meridional wind velocity and temperature is documented in *Espy et al.* [2003]. This article states that such correlation is consistent with the idea of meridional wind modulations causing vertical flows that lead to adiabatic cooling or heating of the polar mesosphere. Therefore the meridional component was chosen for comparison. The radar at Sanae measures the wind above Troll but did not produce data for the year 2009. In addition are the wind measurements very noisy. Therefore daily means from of wind data in 2005 were created to enhence the signal to noise ratio. Figure 5.8 shows the wind variation, the Morlet wavelet and the integrated variance for periods between 1.7-4-days, 4-8-days, 8-16-days and 25-50-days of daily mean meridional wind velocities.

Given that the ozone and wind data are from different altitudes and years only a qualitative comparison can be done. Differences can arise due to interannual variability, interhemespheric wave propagation (Section 2.2.3) or changes in barotropic/baroclinic instabilities. Nevertheless, this qualitative comparison shows that the same ranges of oscillations can be observed in both the ozone and the wind wavelet. Very long periods near the cusp of the wavelet. Mid range periods maximising in winter and spring and short wave activity strengthening in winter. Concerning the short periods it should be noted that the

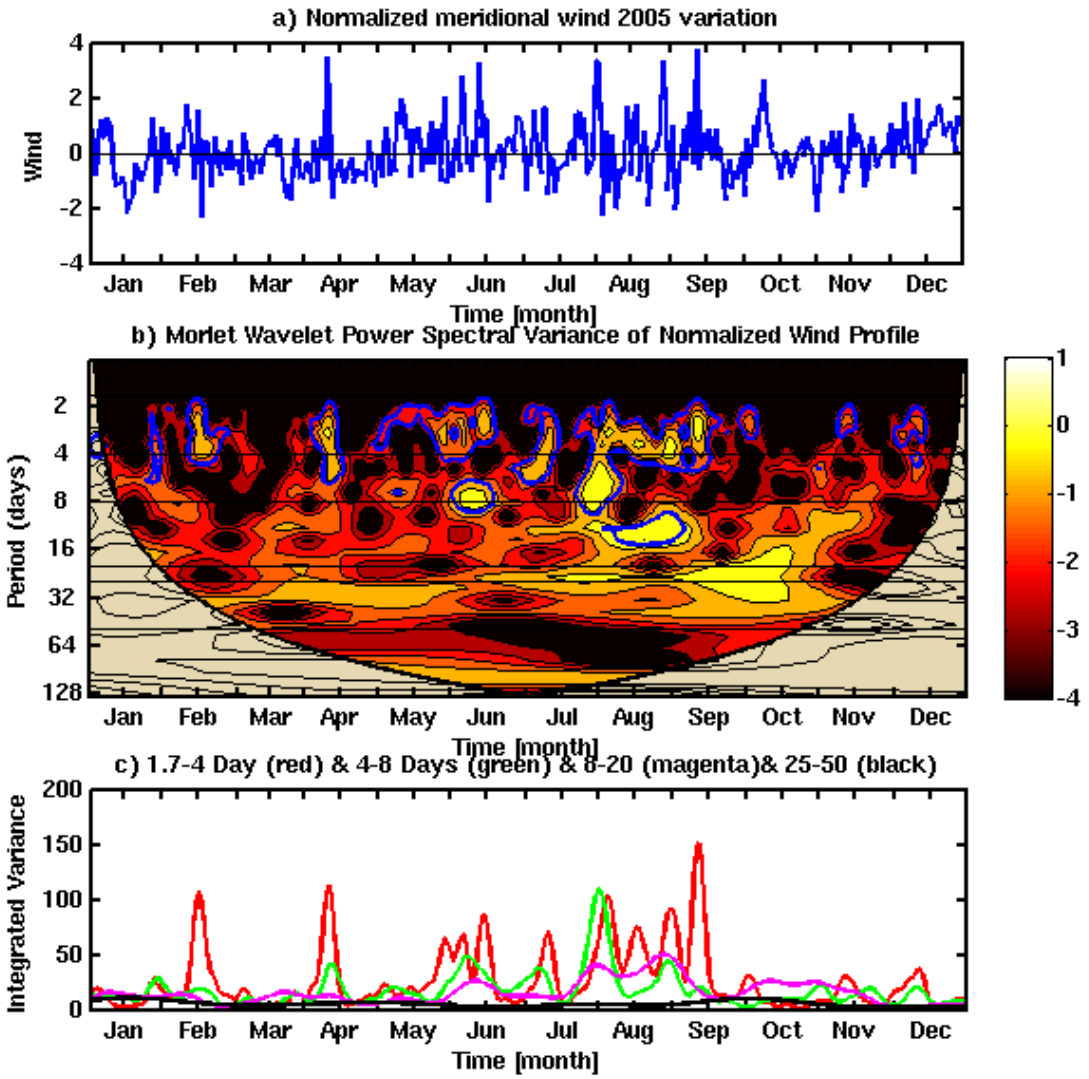

Figure 5.8: (a) Daily mean meridional wind averaged over 2005-2007. (b) Morlet wavelet transform power spectrum from (a). The blue line renders areas of more then 95% significance. The area below the cone-shape solid line is subject to end effects. (c) The wavelet variance integrated over the 1.7-4-day (red), 4-8-day (green), 8-20-day (magenta) and 25-50-day (black) periodic bands.

sample frequency of the wind data (1 day) is much less than the sample frequency of the ozone data ($\approx$ 1h) and that therefore short wave activity is near to the nyquist frequency of the wind wavelet.

The 4-8 day band observed from the Sanae winds ($\approx$ 95 km) is in contrast to the observed wave activities in ozone stronger then the 8-20 band during most of the time and occrues moreover also in summer. It is suggested that at MLT regions, other wave activity than only the normal-mode 5-day wave is present. On the one hand *Palo et al.* [1998] attributes an eastward propagating wave (August -September) with a period near 5-days to instabilities near the poles at 90 km. On the other hand a westward propagating 6.5-day wave [*Meyer and Forbes*, 1997] is predicted to be produced by strong vertical shears in the summer MLT. These additional waves are assumed to be the cause of the strong 4-8-day periodic band in the Sanae winds, referring to altitudes around 95km. The fact that the wind wavelet (year 2005) shows more late winter activity of the 8-20 day band than the ozone wavelet ($\sim$ year 2009) is most likely caused by interannual variabilities of the wind fields.

Summer wave activity and wave activity before equinox (August-Septmber) of the 8-20 day band in the mesosphere might be possible due to interhemispheric propagation. In the winter hemisphere wave activity can propagate vertical into the mesosphere and cross over to the summer hemisphere along wind lines as explained in Section 2.2.3. The existence of a duct between the hemispheres has been supported by modelling studies and modulation of this duct by the quasi-biannual oscillation has been mentioned [*Espy et al.*, 1997].The occurence of late winter wave activity of the 8-20-day band fit with ARON's observations at high altitudes.

The behaviour of the 1.7-4 day band fits with wave activity observed by ARON during April and September and wind shears in the winter stratosphere and mesosphere. In addition instablities in the summer MLT can create a QTDW as described above (Section 5.2) and are consistent with summer wave activity. However one has to be careful associating wave activity of this band in the Sanae data with the QTDW because the 1 day sampling puts them too near to the nyquist frequency of the transform.

In summary no inconsistency between the wave activity observed by ARON and the SuperDarn radar at Sanea can be found. Although the comparison can only be qualitaively due to the altitude and time difference of the two observations, both depict the same range of oscillations, and difference in the occurrence and strength of the considered periodic bands are explainable. This is a strong evidence that it is possible to trace planetary wave with ground based remote sensing of ozone at stratospheric and mesospheric altitudes.

Chapter 6

Conclusion and future work

Ozone mixing ratio profiles were calculated from ground based remote sensing measurements at Troll ($72°S, 2°E$) Antarctica using an optimal estimation method for a period of one year (December 2008 - November 2009). At altitudes between 35 km and 75 km the inverted profiles can be assumed to reflect the real profile present in the atmosphere. The profiles show a clear occurrence of the middle mesospheric maximum and are in good accordance with the COMMA-IAP model. Spectral analysis techniques as the Lomb-Scargle and the Morlet wavelet transform have been used to assess wave activity from these profiles. Here it was important to take seasonal and vertical variations of the ozone profile into account. Observation was possible in the upper stratosphere the whole year, and at middle mesospheric altitudes during the occurrence of the tertiary maximum of ozone mixing ratio. Observation in summer mesospheric regions was not possible due to absence of ozone. Wave activity for four periodic bands, namely a 1.7-4, a 4-8, an 8-20 and a 25-50 day band, could be extracted and was in good accordance with other observations and models. Wave activity was associated with the QTDW and the first three planetary normal modes known as the quasi 5-day, 10-day and 16-day wave, all with zonal wave number one.

The occurrence of the 1.7-4 day band, which was associated with the QTDW, shows good temporal agreement with documented vertical and horizontal sheers. This supports the theory that such wave activity is triggered by baroclinic and barotropic instabilities. The behaviour of the other two bands is consistent with vertical wave propagation of westward propagating planetary waves in winter due to a mean eastward wind and wave absorption in summer due to westward mean winds. Furthermore, a form of mode coupling seems to exist between the different wave modes.

Differences and similarities between wave activity in the MLT and the SLM region above Troll were obvious from a qualitative comparison with wave activity at ca. 95 km extracted from meteor wind measurements at Sanae. Differences were associated with instabilities in the MLT region creating additional waves in the 4-8-day periodic band and with interhemispheric propagation perhaps leading to wave activitiy of the 8-20 day band. Similarities have been attributed to vertical wave propagation from the SLM into the MLT region.

Together the results indicate that ozone from the upper stratosphere and mesosphere can be used to trace planetary waves, and that ground based remote sensing provide a possibility for continuous observation of wave motion with a good temporal resolution. However further testing of this method and moreover some improvements have to be done:

- even temporal spaced profiles

  Even temporal spacing would make the wavelet transform more accurate and might also afford the extraction of subdiurnal tide. This can be achieved by using the ozone measurements of the narrowband CTS to generate ozone profiles while the broadband CTS measures CO. In addtion, extrapolation over remaining missing profiles might be considered.

- improved model of amplification

  An improved modelling of the amplification of wave activity in ozone mixing ratio including effects of hydrogen, nitrogen, and chlorine chemistry as well as cosmic radiation and the change of solar radiation with height and time of day, should be calculated to be able to interpret observed wave amplitude variation with altitude.

- better a priori profiles

  By using models like the COMMA-IAP model, as a priori profiles for the invertions effects due to monthly a priori changes would eliminated. In addition support this models both the strong day-night changes in the contribution of the high altitude ozone and the accurence of the middle mesospheric maximum.

Furthermore investigations have to be done to determine the propagation direction, phase and wave number of the observed waves. Therefore observations at Troll should be connected to other simultaneous observations of stratospheric and mesospheric wave activities.

Finally the inverted ozone profiles can be used to study middle atmospheric ozone chemistry at Antarctica. Such as the occurrence and cause for the middle mesospheric maxima and influences of mesospheric ozone due to solar activity.

References

Andrews, D., *An Introduction to Atmospheric Physics*, Cambridge University Press, 2000.

Andrews, D., J. Holton, and C. Leovy, *Middle Atmosphere Dynamics*, Oxford University Press, 1994.

Baldwin, M., and et al., Major stratospheric warming in the southern hemisphere in 2002: Dynamical aspects of the ozone hole split, *SPARC Newsletter 20*, http://www.atmosp.physics.utoronto.ca/people/sparc/News20/index.html, 2003.

BAS, *Britisch Antarctic Survey*, http://www.antarctica.ac.uk.

Baumgaertner, A., A. McDonald, R. Hibbins, D. Fritts, D. Murphy, and R. Vincent, Short-period planetary waves in the antarctic middle atmosphere, *Journal of Atmospheric and Solar-Terrestrial Physics*, *70*(10), 1336 – 50, 2008.

Blank, C., T. Baurer, M. Bortner, and A. Feryok, *A Pocket Manual of the Physical and Chemical Characteristics of the Earth's Atmosphere.*, Defence Nuclear Agency Report number DNA3467H, 1974.

Brasseur, G., and S. Solomon, *Aeronomy of the Middle Atmosphere - Chemistry and Physics of the Stratosphere and Mesosphere*, Springer, 2005.

Buehler, S., P. Eriksson, T. Kuhn, A. von Engeln, and C. Verdes, Arts, the atmospheric radiative transfer simulator, *Journal of Quantitative Spectroscopy and Radiative Transfer*, *91*(1), 65–93, 2005.

Buehler, S., P. Eriksson, W. Haas, N. Koulev, T. Kuhn, and O. Lemke, *ARTS User Guide (v.1.0.208)*, 2007.

Christensen, O., Atmospheric dynamics over antarctica studied by the use of a microwave radiometer, Master's thesis, Norges Teknisk-Naturvitenskaplige Universitet (NTNU), 2009.

Eriksson, P., C. Jiménez, and S. Buehler, Qpack, a general tool for instrument simulation and retrieval work, *Journal of Quantitative Spectroscopy and Radiative Transfer*, *91*(1), 47–64, 2005.

Espy, P., J. Stegman, and G. Witt, Interannual variations of the quasi-16-day oscillation in the polar summer mesospheric temperature, *Journal of Geophysical Research*, *102*(D2), 1983 – 1990, 1997.

Espy, P., R. Hibbins, G. Jones, D. Riggin, and D. Fritts, Rapid, large-scale temperature changes in the polar mesosphere and their relationship to meridional flows, *Geophysical Research Letters*, *30*(5), 44 – 1 – 44–4, 2003.

Espy, P., R. Hibbins, D. Riggin, and D. Fritts, Mesospheric planetary waves over antarctica during 2002, *Geophysical Research Letters*, *32*(21), 4 pp. –, 2005.

Espy, P., P. Hartogh, and K. Holmen, A microwave radiometer for the remote sensing of nitric oxide and ozone in the middle atmosphere, *Proceedings of the SPIE - The International Society for Optical Engineering*, *6362*, 63,620 – 1, 2006.

Forbes, J., *Tidal and planetary waves, in The Upper Mesosphere and Lower Thermosphere: A Review of Experiment and Theory*, 67-87 pp., geophysical Monograph, 87, Eds. R.M. Johnson and T.L. Killeen, 1995.

Greenwald, R., and et al., Darn/superdarn. a global view of the dynamics of high-latitude convection, *Space Science Reviews*, *71*(1-4), 761 – 96, 1995.

Hall, G., J. MacDougall, D. Moorcroft, J.-P. St.-Maurice, A. Manson, and C. Meek, Super dual auroral radar network observations of meteor echoes, *Journal of Geophysical Research*, *102*(A7), 14,603 – 14, 1997.

Hamill, P., and O. B. Toon, Polar stratospheric clouds and the ozone hole, *Physics Today*, pp. 34–42, 1991.

Hartogh, P., and C. Jarchow, Millimeter wave detection of mesospheric ozone using a high resolution chirp transform spectrometer backend, *International Geoscience and remote sensing system symposium*, *1*, 3, 1994.

Hartogh, P., C. Jarchow, G. Sonnemann, and M. Grygalashvyly, On the spatiotemporal behavior of ozone within the upper mesosphere/mesopause region under nearly polar night conditions, *Journal of Geophysical Research*, *109*(D18), 17 pp. –, 2004.

Hibbins, R., and M. Jarvis, A long-term comparison of wind and tide measurements in the upper mesosphere recorded with an imaging doppler interferometer and superdarn radar at halley, antarctica, *Atmospheric Chemistry and Physics*, *8*(5), 1367 – 1376, 2008.

Hibbins, R., J. Shanklin, P. Espy, M. Jarvis, D. Riggin, D. Fritts, and F.-J. Lubken, Seasonal variations in the horizontal wind structure from 0-100 km above rothera station, antarctica (67°s,68°w), *Atmospheric Chemistry and Physics*, *5*(11), 2973 – 2980, 2005.

IAP, *Institutbericht*, chapter 38-39, Leibniz-Institut für Atmosphärenphysik, 2002/2003.

Jarchow, C., Bestimmung atmosphaericher wasserdampf- und ozonprofile mittels bodengebundener millimeterwellen-fernerkundung, Ph.D. thesis, Universität Bremen, 1998.

Liou, K., *An Introduction to Atmospheric Radiation*, Academic Press, 2002.

Luo, Y., A. Manson, C. Meek, K. Igarashi, and C. Jacobi, Extra long period (20-40 day) oscillations in the mesospheric and lower thermospheric winds: Observations in canada, europe and japan, and considerations of possible solar influences, *Journal of Atmospheric and Solar-Terrestrial Physics*, *63*(9), 835 – 852, 2001.

Luo, Y., et al., The 16-day planetary waves: Multi-mf radar observations from the arctic to equator and comparisons with the hrdi measurements and the gswm modelling results, *Annales Geophysicae*, *20*(5), 691 – 710, 2002.

Malberg, H., *Meteorologie und Klimatologie - Eine Einführung*, Springer, 2007.

Marsh, D., A. Smith, G. Brasseur, M. Kaufmann, and K. Grossmann, The existence of a tertiary ozone maximum in the high-latitude middle mesosphere, *Geophysical Research Letters*, *28*(24), 4531 – 4, 2001.

Meyer, C., and J. Forbes, A 6.5-day westward propagating planetary wave : origin and characteristics, *Journal of Geophysical research*, *102*(D22), 26,173–8, 1997.

Murphy, D., W. French, and R. Vincent, Long-period planetary waves in the mesosphere and lower thermosphere above davis, antarctica, *Journal of Atmospheric and Solar-Terrestrial Physics*, *69*(17-18), 2118 – 2138, 2007.

Palo, S., Y. Portnyagin, J. Forbes, N. Makarov, and E. Merzlyakov, Transient eastward-propagating long-period waves observed over the south pole, *Annales Geophysicae*, *16*(11), 1486 – 500, 1998.

Palo, S., J. Forbes, X. Zhang, I. Russell, J.M., and M. Mlynczak, An eastward propagating two-day wave: evidence for nonlinear planetary wave and tidal coupling in the mesosphere and lower thermosphere, *Geophysical Research Letters*, *34*(7), 273 – 6, 2007.

Picone, J., A. Hedin, D. Drob, and A. Aikin, Nrlmsise-00 empirical model of the atmosphere: Statistical comparisons and scientific issues, *Journal of Geophysysical Research*, *107*(A12), 1468, 2002.

Prata, A., The 4-day wave, *Journal of Atmospheric sciences*, *41*(1), 150 – 155, 1983.

Press, W., and S. Teukolsky, Search algorithm for weak periodic signals in unevenly spaced data, *Computers in Physics*, *2*(6), 77 – 80, 1988.

Ridgway, W., R. Moose, and A. Cogley, Atmospheric transmittance/radiance computer code fascod2, u.S. Air Force Geophysics Laboratory, 1982.

Rodgers, C., Retrieval of atmospheric temperature and composition from measurements of thermal radiation, *Reviews of Geophysics and Space Physics*, *14*(4), 609–624, 1976.

Rothman, L., et al., The hitran database: 1986 edition, *Applied Optics*, *26*(19), 4058 – 97, 1987.

Salby, M., Rossby normal modes in nonuniform background configurations. ii. equinox and solstice conditions, *Journal of the Atmospheric Sciences*, *38*(9), 1827 – 40, 1981.

Salby, M., *Fundamentals of Atmospheric Physics*, Academic Press, 1995.

Salby, M., and P. Callaghan, Seasonal amplification of the 2-day wave: relationship between normal mode and instability, *Journal of the Atmospheric Sciences*, *58*(14), 1858 – 69, 2001.

Sander, S. P., and et al., *Chemical Kinetics and Photochemical Data for Use in Atmospheric Studies*, evaluation Number 15. JPL Publ.06-2, 2006.

Shoelson, B., http://www.mathworks.com/matlabcentral/fileexchange/993-lombscargle-m, 2003.

Sofieva, V., and et al., Spatio-temporal observations of the tertiary ozone maximum, *Atmospheric Chemistry and Physics*, *9*(13), 2009.

Sonnemann, G., C. Kremp, A. Ebel, and U. Berger, A three-dimensional dynamic model of the minor constituents of the mesosphere, *Atmospheric Environment*, *32*(18), 3157 – 3172, 1998.

Sonnemann, G., M. Grygalashvyly, P. Hartogh, and C. Jarchow, Behavior of mesospheric ozone under nearly polar night conditions, *Advances in Space Research*, *38*(11), 2402 – 7, 2006.

Sonnemann, G., P. Hartogh, C. Jarchow, M. Grygalashvyly, and U. Berger, On the winter anomaly of the night-to-day ratio of ozone in the middle to upper mesosphere in middle to high latitudes, *Advances in Space Research*, *40*(6), 846 – 54, 2007.

Todaro, R. M., and et al., *Stratospheric Ozone - An Electronic Textbook*, http://www.ccpo.odu.edu/SEES/ozone/oz_class.htm, 2003.

Torrence, C., and G. Compo, *A Practical Guide to Wavelet Analysis*, http://paos.colorado.edu/research/wavelets/bams_79_01_0061.pdf, 1998.

Uppsala, and et al., The era-40 re-analysis, *Quarterly Journal of the royal meteorological society*, *131*, 2961–3012, 2005.

Vallis, G., *Atmospheric and Oceanic Fluid Dynamics - Fundamentals and Large-Scale Circulation*, Cambridge University Press, 2006.

Vincent, R., Gravity-wave motions in the mesosphere, *Journal of Atmospheric and Terrestrial Physics*, *46*(2), 119 – 28, 1984.

Volland, H., *Atmospheric Tidal and Planetary Waves*, Kluwer Academic Publishers, 1988.

Younger, P., D. Pancheva, H. Middleton, and N. Mitchell, The 8-hour tide in the arctic mesosphere and lower thermosphere, *Journal of Geophysical Research*, *107*(A12), 2 – 1, 2002.

Appendix A

Nomenclature

a	earth's radius
B_1	constant wind amplitude
c	speed of light
c_p	zonal phase velocity
C_p	specific heating rate per unit mass
f	coriolis parameter $= 2\Omega \sin \phi$
f	lineshape factor
$\mathbf{F}$	force
Δf	channel spacing
g	gravity acceleration
G_n	vertical structure
H	scale height $\equiv \frac{RT_m}{g}$
h_n	equivalent depth
$\hbar$	Planck constant
J	heating rate per unit mass
j_i	photodissociation rate coefficient
j_σ	stimulated emission
J_n	vertical profile of heating
k	zonal wave number
k_B	Boltzmann constant
k_i	chemical rate coefficent
m	mass
M	arbitrary air molecule
n	meridional wave number
N	buoyancy frequency $= \sqrt{\frac{\kappa g}{H}}$
$\mathbf{p}$	pressure

r	distance from the earth centre
R	gas constant for dry air
s	vertical wave number
t	time
T	temperature
T_m	constant mean temperature
U	zonal wind
$\mathbf{u}$	velocity $= \left\{ \begin{array}{c} u \\ v \\ w \end{array} \right\}$
u	eastward velocity
v	northward velocity
w	vertical velocity

$$\alpha = \sqrt{\frac{\kappa H}{h_n} - \frac{1}{4}}$$

ϵ_n	eigenvalue of the Laplace tidal equation $= \dfrac{(2\Omega a)^2}{g h_n}$
η	viscosity
Θ_n	Hough functions
κ	ratio of gas constant to specific heat at constant pressure $\equiv \dfrac{R}{C_p} \approx \dfrac{2}{7}$
λ	longitude
μ	mixing ratio
ν	normalised frequency $= \dfrac{\sigma}{\Omega}$
ρ	density
σ	frequency
Σ	wave number
Σ_0	wave number of an ideal, monochromatic line
$\Delta\Sigma$	half width of half maximum (HWHM)
τ	wave period
ϕ	latitude
Φ	geopotential $= -\int \dfrac{RT}{p} dp$
ω	photon frequency
Ω	angular velocity of the earth $= 7.29 \cdot 10^{-5} s^{-1}$

Appendix B

Basic equations

B.1 Navier-Stokes equation

The derivation of the Navier-Stokes equation described in this chapter follows *Andrews* [2000]. The atmosphere is considered to be a continuous, isotropic, classical and Newtonian fluid which is forced by gravity (F_g), friction (F_{vis}) and pressure gradients (F_p). This assumption is a good approximation for the middle and lower atmosphere. By applying Newton's second law to a small moving cubic parcel of air with Volume δV and mass $\rho \delta V$, the momentum equation, also known as Navier-Stokes-Equation,

$$\frac{D\mathbf{u}}{Dt} = \frac{F_p + F_g + F_{vis}}{m} = -\frac{1}{\rho}\nabla \mathbf{p} g \mathbf{e}_z + \frac{\nu}{\rho}\nabla^2 \mathbf{u}, \tag{B.1}$$

is obtained. $\frac{D\mathbf{u}}{Dt} = \frac{\partial}{\partial t} + (\mathbf{u} \cdot \nabla)\,\mathbf{u}$ is the material derivative and represents the rate of change with respect to time following the motion. The rotation of the earth has to be taken into account to understand atmospheric dynamics, resulting in Coriolis (F_c) and centripetal force. The centripetal force is much less in magnitude than the force of gravity and in opposite direction. Therefore the centripetal term is usually neglected and $\mathbf{g}$ denotes the acceleration due to gravity and centrifugal forces. This leads to the Navier-Stokes equation in a rotation frame,

$$\frac{D\mathbf{u}}{Dt} = \frac{F_p + F_c + F_g + F_{vis}}{m} = -\frac{1}{\rho}\nabla \mathbf{p} - 2\Omega \times \mathbf{u} - \mathbf{g} + \frac{\eta}{\rho}\left(\nabla^2 \mathbf{u} + \frac{1}{3}\nabla(\nabla \mathbf{u})\right), \tag{B.2}$$

where $\mathbf{u}$ now represents the velocity in the rotating frame. Furthermore, $\mathbf{g}$ is usually taken as a constant because the variation of $|\mathbf{g}|$ over the altitude range of the atmosphere is small. Using spherical coordinates (Section B.1.1), as the best choice to solve problems in the atmosphere of the earth Equation B.2 can be written in component and linearised

form as

$$\frac{Du}{Dt} - \left(2\Omega + \frac{u}{r\cos\phi}\right)(v\ \sin\phi - w\ \cos\phi) + \frac{1}{\rho}\frac{\partial p}{\partial x} = \mathbf{F}_{vis}\mathbf{i}, \tag{B.3}$$

$$\frac{Dv}{Dt} + \frac{wv}{r} + \left(2\Omega + \frac{u}{r\ \cos\phi}\right)u\ \sin\phi + \frac{1}{\rho}\frac{\partial p}{\partial y} = \mathbf{F}_{vis}\mathbf{j}, \tag{B.4}$$

$$\frac{Dw}{Dt} - \frac{u^2+v^2}{r} - 2\Omega\ \cos\phi + \frac{1}{\rho}\frac{\partial p}{\partial z} + g = \mathbf{F}_{vis}\mathbf{k}. \tag{B.5}$$

$$\tag{B.6}$$

The first to terms refer to horizontal and the last one to the vertical motion.

B.1.1 Spherical coordinates

Spherical coordinates (r,ϕ,λ) are defined as the distance from the earth centre (r), the latitude (ϕ) and the longitude (λ). A small incremental distance in eastward, northward and vertical direction can be written as [*Andrews*, 2000]:

$$dx = r\ \cos\phi\ d\lambda, \tag{B.7}$$

$$dy = r\ d\phi, \tag{B.8}$$

$$dz = d(r-a) = dr, \tag{B.9}$$

respectively, where z is the distance from the earth surface and a is the radius of the earth. Unit vectors at a point on earth are defined as **i**, **j**, and **k** pointing eastward, northward and upwards, respectively.

B.2 Approximations

To be able to understand and calculate different motions further approximations have to be made. The following approximations are for example described in *Vallis* [2006] and *Andrews* [2000].

- **shallow water approximation**
  The earth atmosphere is very shallow (thermosphere $\approx$ 100km) and therefore the distance from the earth centre can be approximated by the earth radius $a \approx 6400$ km. The distance from the earth center (r) can therefore be replaced by the radius of the earth (a), if it is not used as a differential argument, producing only a negligible error.
- **traditional approximation**
  Vertical winds are much smaller then horizontal winds and in addition the metric terms ($\frac{1}{r}$-terms) vanish if the scale of the problem is smaller then the radius of the earth.

- **hydrostatic approximation**
  Scale analysis show that for frictionless large-scale flow, the vertical momentum equation (B.5) reduces to the hydrostatic balance, because the remaining terms are gravity and pressure force.

Taking all three approximations together, neglecting friction and defining the Coriolis parameter $f = 2\Omega \sin\phi$, the spherical momentum equations in a rotational frame (Equation B.6) simplify to *Andrews* [2000],

$$\frac{Du}{Dt} - fv + \frac{1}{\rho}\frac{\partial \mathbf{p}}{\partial x} = 0, \tag{B.10}$$

$$\frac{Dv}{Dt} + fu + \frac{1}{\rho}\frac{\partial \mathbf{p}}{\partial y} = 0, \tag{B.11}$$

$$\frac{\partial \mathbf{p}}{\partial z} = -\mathbf{g}\rho. \tag{B.12}$$

$$\tag{B.13}$$

These are he horizontal momentum equations and the hydrostatic approximation, respectively.

B.3 U_n & V_n

U_n is the zonal, while V_n is the meridional wind [*Forbes*, 1995]:

$$U_n = \frac{1}{f^2 - \sin^2\phi}\left[\frac{k}{\cos\phi} + \frac{\sin\phi}{f}\frac{d}{d\phi}\right]\Theta_n$$

$$V_n = \frac{1}{f^2 - \sin^2\phi}\left[\frac{k\tan\phi}{f} + \frac{d}{d\phi}\right]\Theta_n$$

B.4 Separation condition

The condition of separation for z and ϕ of Equation 2.5 is [*Forbes*, 1995]:

$$i\sigma\left[\frac{1}{\rho_0}\frac{\partial}{\partial z}\left(\frac{\rho_0}{N^2}\right)\frac{\partial}{\partial z}G_n\right] + \frac{1}{\rho_0}\frac{\partial}{\partial z}\left(\frac{\rho_0 \kappa J_n}{HN^2}\right) = \frac{i\sigma}{gh_n}G_n$$

B.5 Laplace's tidal equation

The ϕ depending part of Equation 2.5 is covered by Laplace's tidal equation:

$$\frac{d}{d\sin\phi}\left[\frac{\left(1-\sin^2\phi\right)}{\left(f^2-\sin^2\phi\right)}\frac{d\Theta_n}{d\sin\phi}\right] - \frac{1}{f^2-\sin^2\phi}\left[-\frac{k}{f}\frac{\left(f^2+\sin^2\phi\right)}{\left(f^2-\sin^2\phi\right)} + \frac{k^2}{1-\sin^2\phi}\right]\Theta_n + \epsilon_n\Theta_n = 0$$

Appendix C

Ozone mixing ratio vs. temperature variations

t	=	time sequence
$ampl$	=	amplitude of temperature variations
$Densxx$	=	air density at xx km
$Tempxx$	=	temperature at xx km in K
$ampl$	=	0.01
$Dens45$	=	$4.15 \cdot 10^{22}$
$Temp45$	=	268
$Dens70$	=	$1.822 \cdot 10^{21}$
$Temp70$	=	216
T		temperature variation
M		density variation
O_2		molecular oxygen variation
O_3^{tot}		total Ozone mixingratio variation
O_3		percental ozone mixing ratio variation

$$
\begin{aligned}
T &= Tempxx \cdot \left[1 + ampl \cdot \cos\left(\frac{2\pi t}{5}\right)\right] \\
M &= Densxx \cdot \left[1 - ampl \cdot \cos\left(\frac{2\pi t}{5}\right)\right] \\
O_2 &= M \cdot 0.2 \\
O_3^{tot} &= \frac{O_2}{\sqrt{M}} \sqrt{\frac{6 \cdot 10^{-34} \left(\frac{T}{300}\right)^{-2.4}}{8 \cdot 10^{-12}\ e^{\left(\frac{-2060}{T}\right)}}} \frac{j_2}{j_3} \\
O_3 &= \frac{O_3^{tot} - \overline{O_3^{tot}}}{\overline{O_3^{tot}}} \cdot 100
\end{aligned}
$$

Used model values for temperature and density were taken from *Blank et al.* [1974]. The values for the photodissociation rates j_i are taken from *Andrews* [2000] and correspond to solar radiation at 25 km at noon. Due to the fact that they are temperature independent cancel their contribution for the percental ozone mixing ratio variation.

Appendix D

A priori

Figure D.1 shows the used a priori profiles for all months and Figure D.2 the altitude grid for all months. Table D.1 lists the used model atmospheres. Spectroscopic data are mostly taken from HITRAN [*Rothman et al.*, 1987; *Buehler et al.*, 2007]. Continums absorption is modeld for water vapor and molecular oxygen [*Christensen*, 2009].

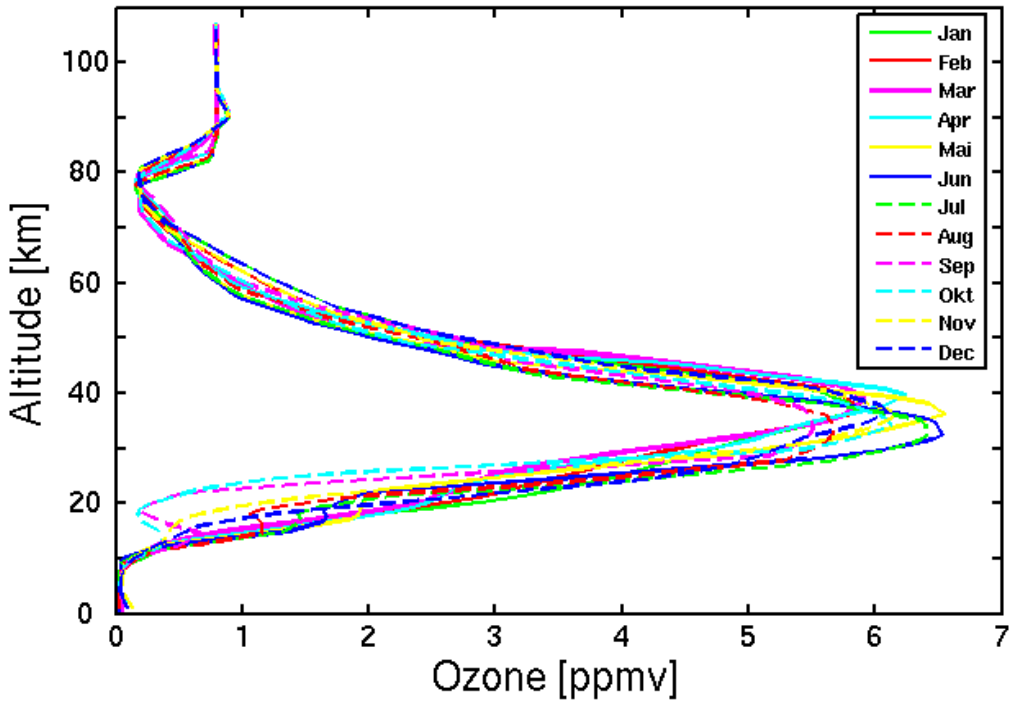

Figure D.1: Used a priori profiles

	Temperature and pressure	**O_3 and water vapor absorption**
< 45 km	ERA40 model [*Uppsala and et al.*, 2005]	monthly average of the ERA40 model (71 − 73° S and 1.5 − 3°E, year 2001)
>45 km	MSIS model [*Picone et al.*, 2002]	standard model data from FASCOD [*Ridgway et al.*, 1982] summer a priori: October- February winter a priori: Mars- September
	constant values above 85 km due to limited model	constant values above 85 km due to limited model

Table D.1: A priori profiles used for the inversion

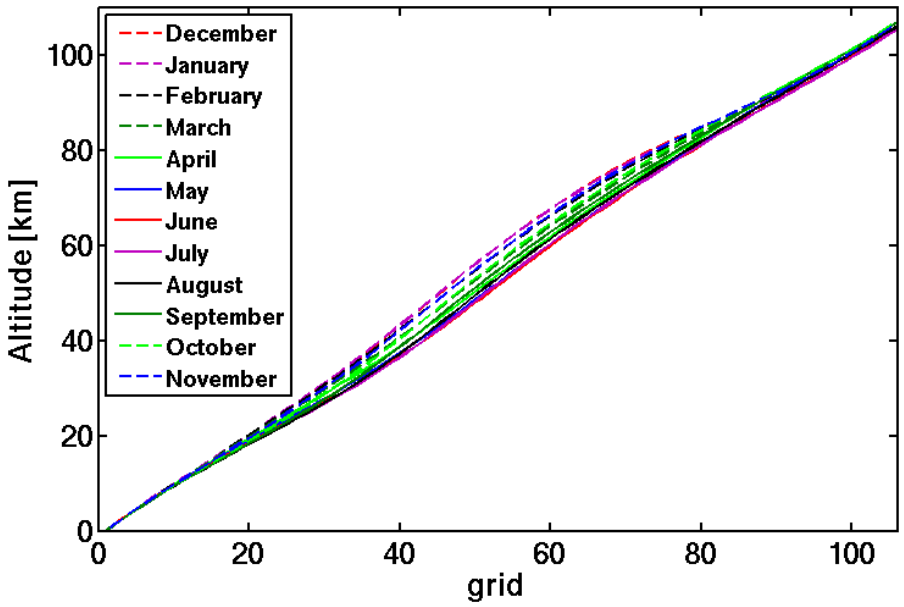

Figure D.2: Altitude grid for different month

Appendix E

Figures

E.1 Examples of false spectra

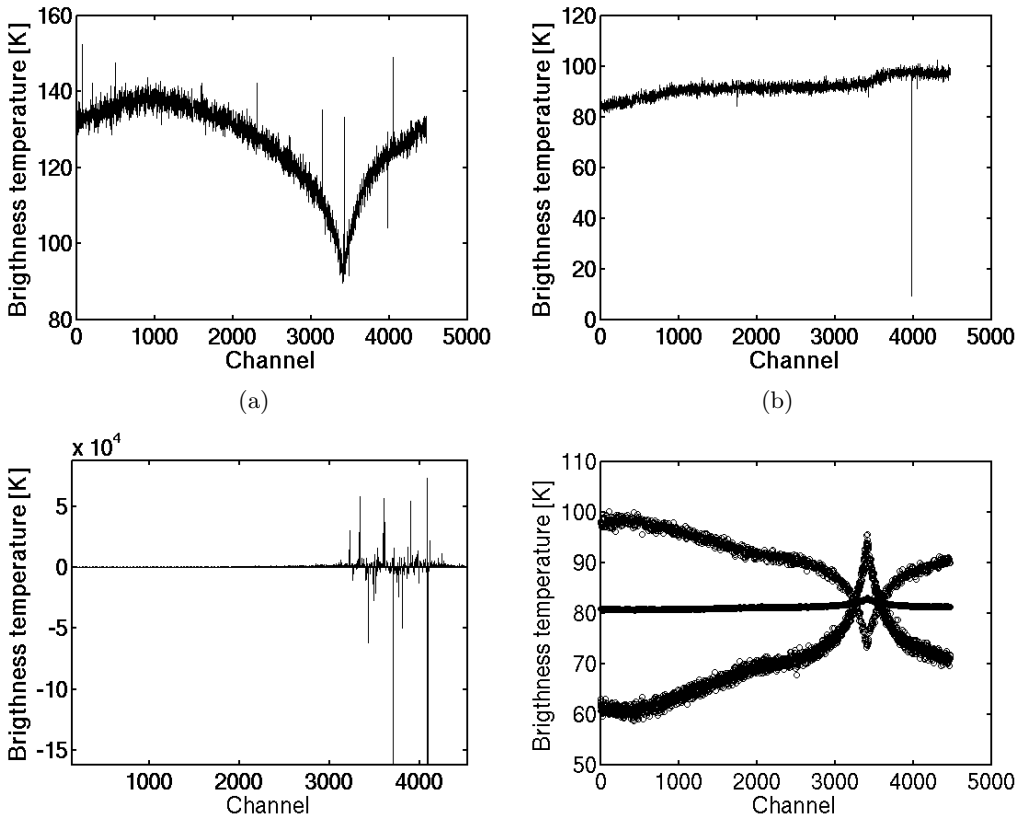

Figure E.1: Excamples of false spectra produced by ARON

E.2 Measurement response

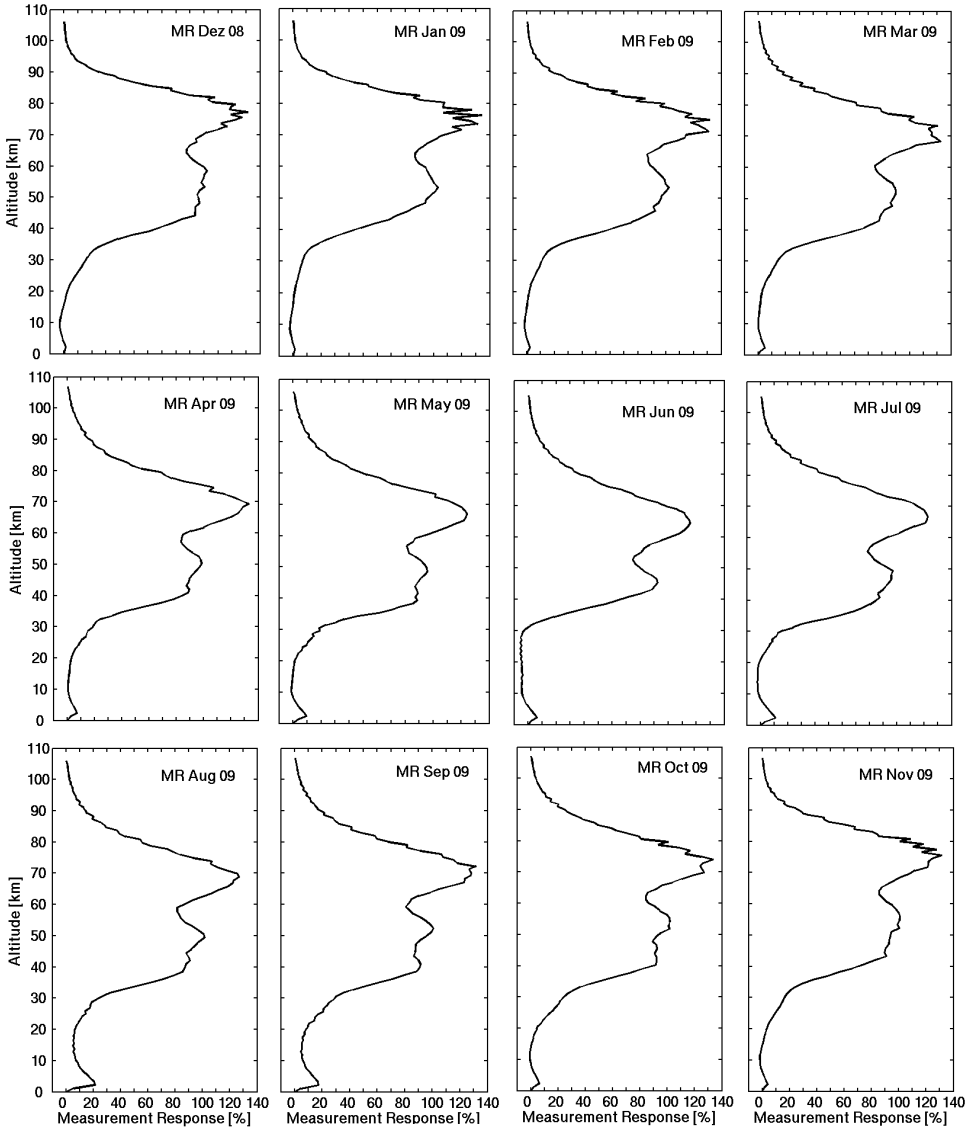

Figure E.2: Sample measurement response for inversions of the 249.96196 GHz Ozone line for different months.

E.3 Averaging kernel

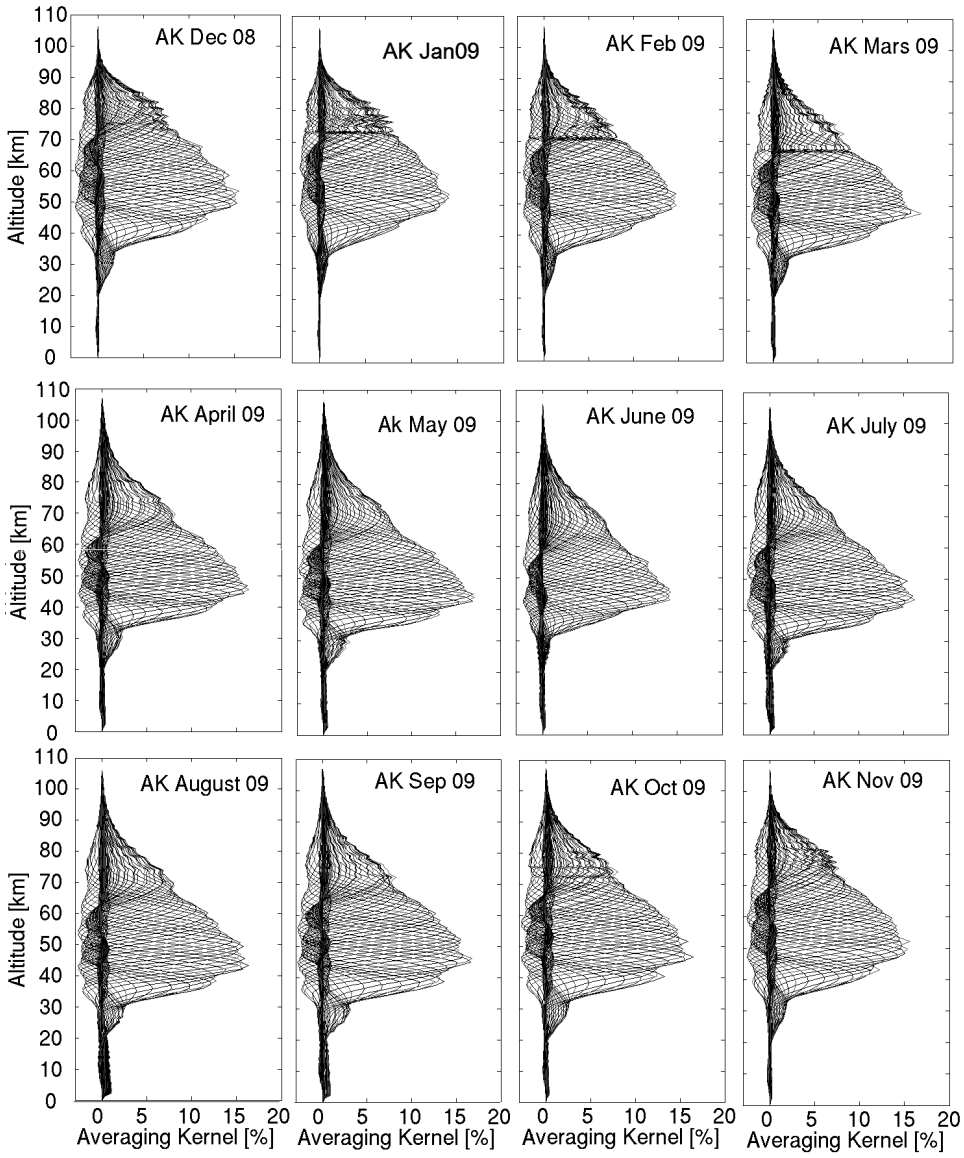

Figure E.3: Sample averaging kernels for inversions of the 249.96196 GHz ozone line for different months.

E.4 Spectral Analysis

E.4.1 Lomb-Scargle

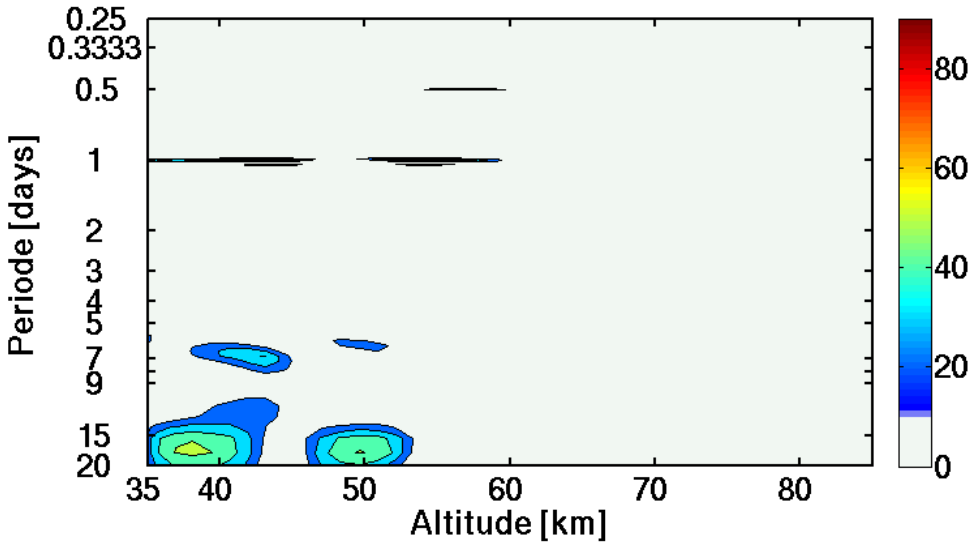

Figure E.4: Lomb-Scargle of the inverted profiles for Januar 2009

E.4.2 Wavelet

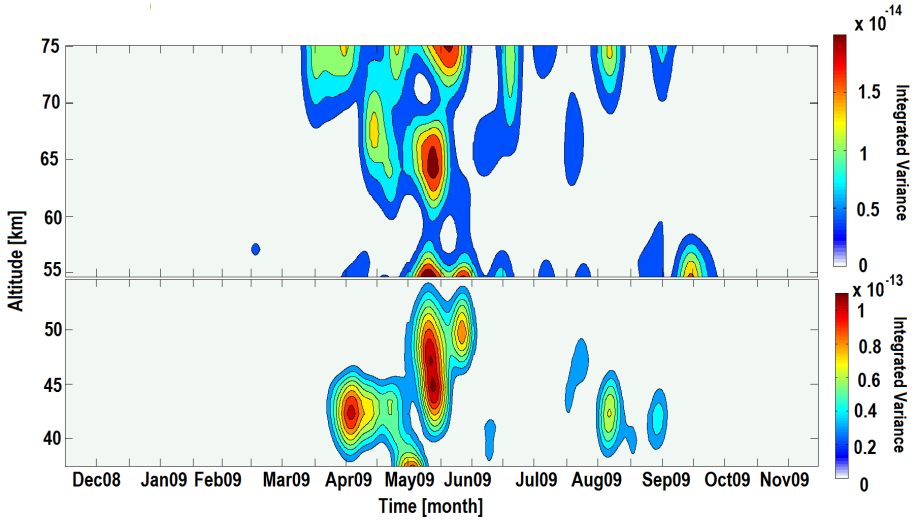

Figure E.5: Integrated variance of the 4-8 periodic band from Morlet wavelet transform of ozone variation from December 2008 until November 2009 over altitude and time

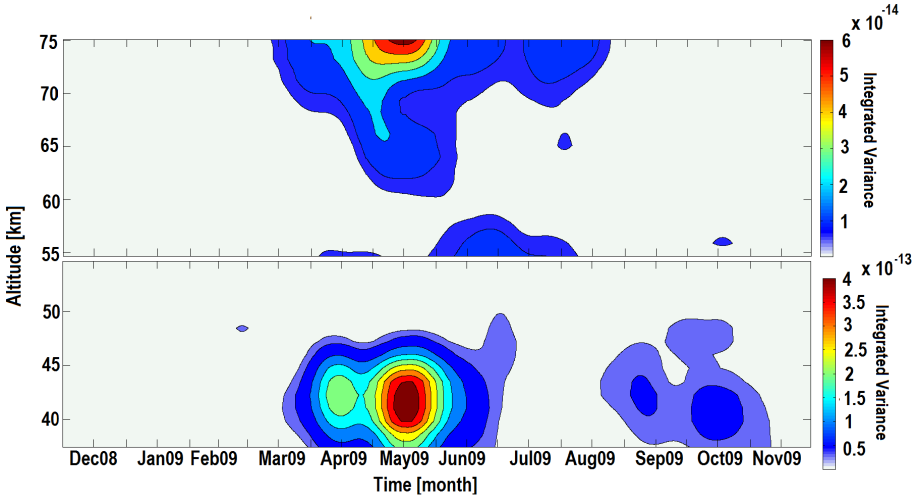

Figure E.6: As Figure E.5 for the 8-20 day periodic band.